Gold nano- and microparticles: synthesis, deposition and their assembly into 2D structures

Katarzyna Winkler

Supervisor: dr hab. Marcin Fiałkowski, prof. IPC PAS

The presented dissertation was prepared within
the International Ph.D. Studies
at the Institute of Physical Chemistry of the Polish Academy of Sciences,
Department of Soft Condensed Matter,
Kasprzaka 44/52, 01-224 Warsaw, Poland.

Warsaw, February 2017

Acknowledgements

Achievements presented in this dissertation would not have been possible to reach without the kind help of many knowledgeable people. I would especially like to thank:

Marcin Fiałkowski, my advisor, for his support and help, fascinating research challenges, pertinent advice, answers and questions.

Robert Hołyst, for the opportunity to study in the Department of Soft Condensed Matter, but also for his inspiring energy, ambition, and strength.

Agnieszka Kamińska and **Tomasz Wojciechowski**, for all the hours spent doing measurements essential for our scientific projects. Agnieszka Kamińska performed and analyzed the SERS spectra, Tomasz Wojciechowski (Institute of Physics PAS) took the majority of the SEM images and taught me how to take the remaining ones by myself. Tomasz Wojciechowski is also responsible for the EDX measurements and the FIB-milling process.

Volodymyr Sashuk, for collaboration and inspiring discussions, for support, patience, and faith.

Ewelina Kalwarczyk, **Jan Paczesny, Tomasz Szymborski, Katarzyna Wybrańska**, and **Andrzej Żywociński**, for being there to work, talk, and laugh together. Also, I would like to thank Ewelina for her contribution to the ionic-strength controlled method for deposition of nanoparticles, and Jan for cooperation on SERS platform preparation.

Malwina Liszewska, for her contribution to the research on the gold microflowers.

Ewa Górecka (Warsaw University), for the SAXS and XRD measurements.

Thanks to **all the co-authors** of my articles for their help and **all my colleagues** from the Institute of Physical Chemistry for creating a wonderful and inspiring scientific atmosphere.

Financial support

The work was supported by a project operated within the Foundation for Polish Science "Team" programme, co-financed by the EU European Regional Development Fund TEAM/2010-6/4.

INNOVATIVE ECONOMY
NATIONAL COHESION STRATEGY

FNP
Foundation for Polish Science

EUROPEAN UNION
EUROPEAN REGIONAL DEVELOPMENT FUND

The work was partially financed by the National Science Centre "Preludium 1" programme on the basis of the DEC-2011/01/N/ST5/02916 decision.

NATIONAL SCIENCE CENTRE
POLAND

Katarzyna Winkler is also a two-time scholar within the system project „Potencjał naukowy wsparciem dla gospodarki Mazowsza - stypendia dla doktorantów", co-financed by state budget and EU European Social Fund - Sub-measure 8.2.2 Human Capital Operational Programme 2007-2013.

KAPITAŁ LUDZKI
NARODOWA STRATEGIA SPÓJNOŚCI

Mazowsze.
serce Polski

UNIA EUROPEJSKA
EUROPEJSKI FUNDUSZ SPOŁECZNY

List of publications

Papers presented in the dissertation

1. **K. Winkler**, T. Wojciechowski, M. Liszewska, E. Górecka, M. Fiałkowski "Morphological changes of gold nanoparticles due to adsorption onto silicon substrate and oxygen plasma treatment ", *RSC Advances* [IF 3,84] **2014**, 4 (25), 12729-12736
2. J. Paczesny, A. Kamińska, W. Adamkiewicz, **K. Winkler**, K. Sozański, M. Wadowska, I. Dzięcielewski, R. Hołyst "Three steps of hierarchical self assembly toward a stable and efficient surface enhanced Raman spectroscopy platform", *Chemistry of Materials* [IF 8,354] **2012**, 24 (19), 3667-3673
3. **K. Winkler**, A. Kamińska, T. Wojciechowski, R. Hołyst, M. Fiałkowski „Gold Micro-Flowers: One-Step Fabrication of Efficient, Highly Reproducible Surface-Enhanced Raman Spectroscopy Platform", *Plasmonics* [IF 2.238] **2011**, 6 (4), 697–704
4. **K. Winkler**, M. Paszewski, T. Kalwarczyk, E. Kalwarczyk, T. Wojciechowski, E. Górecka, D. Pociecha, R. Hołyst, M. Fiałkowski „Ionic Strength-Controlled Deposition of Charged Nanoparticles on a Solid Substrate", *J. Phys. Chem. C* [IF 4.772] **2011**, 115 (39), 19096–19103

Other papers

5. A. Kamińska, E. Witkowska, **K. Winkler**, I. Dzięcielewski, J. L. Weyher, J. Waluk "Detection of Hepatitis B virus antigen from human blood: SERS immunoassay in a microfluidic system", *Biosensors and Bioelectronics* [IF 6,409] **2015**, 66, 461-467
6. V. Sashuk, **K. Winkler**, A. Żywociński, T. Wojciechowski, E. Górecka, M. Fiałkowski „Nanoparticles In a Capillary Trap: Dynamic Self-Assembly at Fluid Interfaces"; *ACS Nano* [IF 12,881] **2013**, 7 (10), 8833-8839
7. M. Mroczkiewicz, **K. Winkler**, D. Nowis, G. Placha, J. Gołąb, R. Ostaszewski „Studies of the Synthesis of All Stereoisomers of MG-132 Proteasome Inhibitors in the Tumor Targeting Approach", *Journal of Medicinal Chemistry* [IF 5.447] **2010**, 53 (4), 1509–1518

8. J. Łopacińska, M. Skolimowski, M. Dąbrowski, M. Jacewicz, M. Kuciński, **K. Stefanek**, Z. Brzózka „Miniaturowe układy typu Lab-on-a-chip w chemii, biologii i medycynie”; chapter of the book *Na pograniczu chemii i biologii* (ISBN: 978-83-232184-5-6), Wydawnictwo Naukowe UAM, Poznań, tom XIX; strony 71 - 80, **2007**.

Patent applications

1. V. Sashuk, **K. Winkler**, M. Fiałkowski, R. Hołyst „Sposób otrzymywania monowarstwy zbudowanej z gęsto upakowanej warstwy nanocząstek pokrytych ligandami hydrofilowymi i hydrofobowymi, monowarstwa i zastosowanie monowarstwy do pokrywania powierzchni”. Wynalazek zgłoszony do Urzędu Patentowego RP (P-404256) w dniu 10.06.2013.
2. J. Paczesny, K. Sozański, A. Żywociński, W. Adamkiewicz, I. Dzięcielewski, **K. Winkler**, A. Kamińska, R. Hołyst „Platforma do pomiarów SERS oraz sposób jej wykonania”. Wynalazek zgłoszony do Urzędu Patentowego RP (P-397249) w dniu 05.12.2011. Ochrona przyznana (PL 218683) w dniu 23.06.2014.
3. J. Paczesny, K. Sozański, A. Żywociński, W. Adamkiewicz, I. Dzięcielewski, **K. Winkler**, A. Kamińska, R. Hołyst „Sposób pokrywania powierzchni ciała stałego dwuwymiarową siecią nanocząstek i powierzchnia ciała stałego pokryta tym sposobem”. Wynalazek zgłoszony do Urzędu Patentowego RP (P-397169) w dniu 29.11.2011. Ochrona przyznana (PL 217032) w dniu 05.11.2013.
4. **K. Winkler**, M. Fiałkowski, A. Kamińska, R. Hołyst „Verfahren zur Beschichtung von hydrophilen Festkörpern mit einer Goldschicht mit ausgedehnter Oberfläche sowie ein mit einer Goldschicht mit ausgedehnter Oberfläche beschichteter hydrophiler Festkörper“. Wynalazek zgłoszony do Urzędu Patentowego Szwajcarii (CH 01389/11) w dniu 25.08.2011. Ochrona przyznana (CH 703612) w dniu 13.12.2013.
5. M. Paszewski, M. Fiałkowski, E. Kalwarczyk, T. Kalwarczyk, **K. Winkler**, R. Hołyst „Method of coating material surfaces with nanoparticles”. Wynalazek zgłoszony do Urzędu Patentowego Wielkiej Brytanii (GB 1102589.7) w dniu 15.02.2011.
6. **K. Winkler**, M. Fiałkowski, A. Kamińska, R. Hołyst „Sposób pokrywania hydrofilowych ciał stałych warstwą złota o rozbudowanej powierzchni oraz hydrofilowe ciało stałe pokryte warstwą złota o rozbudowanej powierzchni.” Wynalazek zgłoszony do

Urzędu Patentowego RP (P-392222) w dniu 25.08.2010. Ochrona przyznana (PL 219899) w dniu 21.11.2014.

7. M. Paszewski, M. Fiałkowski, E. Kalwarczyk, T. Kalwarczyk, **K. Winkler**, R. Hołyst „Metoda pokrywania powierzchni nanocząstkami”. Wynalazek zgłoszony do Urzędu Patentowego RP (P-391217) w dniu 14.04.2010. Ochrona przyznana (PL 217816) w dniu 27.01.2014.

Theses

- Addition of inorganic salt that screens the electrostatic repulsion between nanoparticles (NPs) makes it possible to arrange positively charged NPs into dense monolayers on a solid substrate.

- Deposition of gold nanoparticles (AuNPs) on solid substrates leads to deformation of the shape of the AuNPs. The extent of the distortions depends on the composition of the organic shell of the AuNPs.

- During the plasma treatment AuNPs exhibit a liquid-like behavior and coalesce into larger objects. This process follows the Smoluchowski Ripening mechanism.

- In the reaction of auric acid and hydroxylamine hydrochloride, gold microflowers (AuMFs) are formed. It is possible to immobilize them on a solid substrate and use them as an effective analytical platform for surface enhanced Raman spectroscopy.

- The morphology of the AuMFs can be controlled by the parameters of the reaction such as reaction time and molar ratio of the reagents, by the addition of inorganic salts, and selection of the solid substrate on which the AuMFs are deposited.

- The AuMFs are reactive gold forms, soluble in dilute inorganic acids. The presence of acids and a reducing agent in the post-reaction mixture leads to the smoothing of the sharp edges of the AuMFs through continuous oxidation of gold atoms by acid, reduction of gold ions by amine, and re-deposition of the resulting atoms on the AuMFs.

Table of contents

Major symbols

2θ – angle between the incident X-ray beam and the detector measuring the scattered intensity, used in SAXS

A – symbol indicating Au^{3+} ions

$[A]$ – concentration of Au^{3+} ions in the reaction solution

$[A]_0$ – initial concentration of Au^{3+} ions in the reaction solution

$[A]_1$ – concentration of the Au^{3+} ions at the beginning of the autocatalytic growth stage

B – symbol indicating metallic gold

$[B]_1$ – concentration of the surface atoms of the growing clusters at the beginning of the autocatalytic growth stage

$B(\theta)$ – blocking function (the fraction of the surface that is available for the oncoming nanoparticles)

c – concentration

C_{100} – water solution of gold nanoparticles in which the concentration of gold is 0.15 mg/mL; the subscript "100" denotes the highest concentration used ("100%") and concentrations C_{75}, C_{50} and C_{25} are respectively lower

$c50(3:8)$ – reaction mixture containing 3:8 $HAuCl_4$: $NH_2OH{\cdot}HCl$ molar ratio, made of one volume of 40 mM $NH_2OH{\cdot}HCl$ with 0.6 volume of 25 mM $HAuCl_4$; mixtures $c10$, $c1$ and $c0.1$ are diluted in respect to $c50$ five, fifty, and five hundred times, respectively; another ratio in the brackets denotes another $HAuCl_4$: $NH_2OH{\cdot}HCl$ molar ratio

C_{NP} – bulk concentration of nanoparticles

C_{salt} – concentration of inorganic salt in the solution

D – diffusion coefficient

e – elementary charge

E_0 – electric field deriving from an incident light

E_{out} – electric field radiated by the illuminated gold nanoparticle

I – intensity of transmitted light

I_0 – intensity of incident light

K – Debye screening length

$k(m, m')$ – rate constant of collisions between two droplets of masses m and m'

k_1 – effective rate of the reduction of Au^{3+} ions

k_2 – rate of the reduction of Au^{3+} ions on gold surfaces

k_a – adsorption rate constant

k_{ads} – adsorption coefficient

k_{agg} – effective aggregation constant

k_B – Boltzmann constant

k_{des} – desorption coefficient

l – length of absorption path

$\ln\mu$ – mean deviation of $\ln R_p$

$\ln\sigma$ – standard deviation of $\ln R_p$

M – molar concentration

m – mass

N – number of particles

n_m – surface density of the nanoparticles of mass m

n_{av}^0 – average droplet density before the plasma treatment

p – polydispersity

Q_{eff} – effective charge

R – radius of the sphere containing spherical cap V_{cap}

R_0 – average radius of the nanoparticles in the solution

R_a – average projected (apparent) radius of the adsorbed nanoparticles

R_p – average radius of the adsorbed nanoparticles after plasma treatment

$<R_{pt}>$ – average radius of the gold droplet during the plasma treatment

r – aspect ratio

S – vacant site on the surface

SNP – nanoparticle bound to the surface site

t – time

T – temperature

t_n – duration of the nucleation stage

V_{av} – average volume of the AuNPs in the bulk solution

V_{cap} – average volume of the AuNPs adsorbed on the substrate

δ – distance from the surface

ε – dielectric constant of the solvent

ε_{abs} – molar absorption coefficient

ε_0 – permittivity of a vacuum

ε_{diel} – permittivity of air

ε_m – permittivity of metal

ζ – Zeta potential

θ – percentage or fractional coverage of the substrate

λ – wavelength

τ – rescaled time, $\tau = t \times k_{ads}$

φ – absorbance

φ_a – average contact angle after adsorption

φ_p – average contact angle after plasma treatment

χ^2 – Statistic of the Chi-square goodness-of-fit test

Major abbreviations

1D, 2D, 3D – one-dimensional, two-dimensional, three-dimensional

AA – ascorbic acid

AgNPs – silver nanoparticles

AFM – atomic force microscpopy

Au@MUA NPs – gold nanoparticles covered with an organic layer of MUA

Au@TMA NPs – gold nanoparticles covered with an organic layer of TMA

AuMFs – gold microflowers

AuNPs – gold nanoparticles

CTAB – cetyltrimethylammonium bromide

CVD – chemical vapor deposition

DDA – dodecylamine

DDT – dodecanethiol

EDS – electron diffraction studies

EF – enhancement factor

FE-SEM – field emission scanning electron microscopy

FIB – focused ion beam
FW model – Finke-Watzky kinetic model
GaN – gallium nitride
ITO – indium tin oxide
LN – log-normal
MSA – 2-mercaptosuccinid acid
MUA – mercaptoundecanoic acid
NP – nanoparticle
OR – Oswald Ripening
PBS – phosphate buffered saline
p-MBA – *p*-mercaptobenzoic acid
PVP – poly(vinylpyrrolidone)
QD – quantum dot
SAXS – small-angle X-ray scattering
SDS – sodium dodecyl sulphate
SEM – scanning electron microscopy
SERS – surface enhanced Raman spectroscopy
SR – Smoluchowski Ripening
TEM – transmission electron microscopy
TMA – *N,N,N*-trimethyl(11-mercaptoundecyl)ammonium chloride ($HS(CH_2)_{11}N(CH_3)_3{}^+Cl^-$)
TOAB – tetraoctyammonium bromide
XRD – X-ray diffraction

Introduction

Abstract

Nanotechnology is a scientific area on the boundary of chemistry, physics, and material engineering. Its essential aspects are design, synthesis, and analysis of nano- and microobjects, as well as their organization into complex and ordered systems. Interestingly, despite years of intense research, our understanding of the processes occurring at the nanoscale is not complete. Usually we fail to predict the properties of new nanomaterials, and designing their synthesis is still a process of trial and error.

Unusual features of nanoparticles make them interesting objects of scientific research. Moreover, nanostructures, having uncommon optical, electrical, and magnetic properties have enormous application potential. They are used, for example, in medicine, the chemical industry, electronic and optical devices, but also in everyday consumer goods like cosmetics and household chemicals. The range of applications is constantly growing, so new types of nanomaterials and methods for their synthesis and manipulation are still needed.

In this dissertation I present the results of my research in the field of nanotechnology. The studied nanostructures are presented in order from the smallest to the biggest objects. First, the results on the organization of gold nanoparticles having 5 nm in diameter and functionalized with organic ligands are described. A new method for their immobilization on solid substrates is introduced, and a way of controlling the density of the deposit is presented. The described gold nanoparticles attach to the solid surface und undergo morphological changes: Their spherical shape flattens and the extent of this deformation depends on the composition of the organic protecting shell on the nanoparticle. Interestingly, I found that after cleaning such deposited nanostructures using oxygen plasma treatment, the particles partially restore their spherical shape. They become, however, larger and their arrangement on the substrate differs from the initial one. The reason is that during the plasma treatment the AuNPs behave like droplets of a non-wetting liquid, exhibiting an ability to move and merge. Experimental evidence suggests that the process of the re-formation of these small gold clusters orders their crystallographic structure, as a result changing their catalytic properties. This conclusion follows from the analysis of morphologies of the plasma-treated nanoparticles after their autocatalytic growth in various growth solutions. The obtained new shapes differ from those observed for nanoparticles prepared without plasma treatment.

The abovementioned findings are described in the first four sections of the Results chapter (4.1 – 4.4). The last two sections, namely 4.5 and 4.6, present microscopic gold structures called microflowers (AuMFs). The AuMFs are branched particles of ~2 μm in diameter and originate in the reaction of two reagents in an aqueous solution. I show that the morphology of these microstructures can be easily tailored by a proper composition of the reaction mixture as well as by the reaction time. In section 4.5, the kinetics of their synthesis is described and stages of their formation are analyzed. Also, the mechanism of the morphological changes of the AuMFs in time is proposed. In section 4.6 an exemplary application of the AuMFs is described. I demonstrate that the AuMFs form stable deposits on solid substrates and exhibit high enhancement of the Raman scattering. These features make them useful in fabricating analytical platforms for surface enhanced Raman spectroscopy (SERS). In this section a method for fabrication of a sensitive and repeatable new SERS platform, with several possible modifications, is described.

Streszczenie

Nanotechnologia to obszar wiedzy na pograniczu chemii, fizyki i inżynierii materiałowej. Istotnym jej aspektem jest projektowanie i synteza nano- i mikroobiektów, a także konstruowanie z nich złożonych i uporządkowanych układów. Co ciekawe, mimo lat intensywnego rozwoju nanotechnologii, nasze zrozumienie procesów zachodzących w nanoskali nadal nie jest pełne. Zazwyczaj nie udaje nam się przewidywać właściwości nowych nanomateriałów, a projektowanie ich syntezy to często proces empiryczny.

Ze względu na swoje właściwości, przede wszystkim optyczne, elektryczne i magnetyczne, nanocząstki stały się obiektem licznych badań naukowych. Znalazły również szerokie zastosowanie m.in. w przemyśle chemicznym, medycynie, produkcji urządzeń elektronicznych i optycznych, ale także w środkach codziennego użytku, takich jak kosmetyki czy środki czystości. Zakres zastosowania nanocząstek stale się poszerza, dlatego też nowe typy nanostruktur i coraz lepsze metody ich syntezy budzą duże zainteresowanie.

W niniejszej dysertacji prezentuję własne dokonania w dziedzinie nanotechnologii. Opis badanych przeze mnie obiektów uporządkowany jest pod względem rozmiarów nanostruktur: od najmniejszych do największych. W pierwszej części badań własnych przedstawione są złote nanocząstki o średnicy 5 nm, pokryte organicznymi ligandami. Zaprezentowana jest nowa metoda osadzania ich na powierzchni ciał stałych w procesie pozwalającym na sterowanie gęstością pokrycia. Tak unieruchomione nanocząstki ulegają przemianom morfologicznym, które analizowane były z użyciem skaningowej mikroskopii elektronowej. Kształt nanocząstek, początkowo kulisty, ulega spłaszczeniu, a stopień tej deformacji jest zależny od składu otoczki organicznej pokrywającej nanocząstkę. Co ciekawe, osadzone nanocząstki poddane czyszczeniu plazmą tlenową częściowo odzyskują swój kulisty kształt. Ich średnica jednak wówczas rośnie a gęstość pokrycia powierzchni ulega zmianie, gdyż pod wpływem plazmy nanocząstki wykazują cechy kropli niezwilżającej cieczy, zdolnych do zmiany miejsca położenia i do zlewania się ze sobą. W czasie tych przemian struktura atomowa nanocząstek prawdopodobnie ulega uporządkowaniu, na co wskazują ich właściwości katalityczne – inne, niż te obserwowane dla nanocząstek niepoddawanych czyszczeniu plazmą. Taki wniosek został wysnuty z eksperymentu, w

którym nanocząstki oczyszczone plazmą poddano procesowi autokatalitycznego wzrostu. Rozkład kształtów otrzymanych struktur różnił się od tego dla nanocząstek czyszczonych innymi metodami.

Przedstawione powyżej obserwacje zostały opisane w pierwszych czterech (4.1 – 4.4) podrozdziałach rozdziału „Results". Pozostałe dwa podrozdziały (4.5 i 4.6) poświęcone są większym złotym strukturom, tak zwanym mikrokwiatom. Mikrokwiaty to cząstki o mocno rozwiniętej powierzchni i średnicy około 2 μm, powstające w reakcji dwóch nieorganicznych związków chemicznych w roztworze wodnym. Morfologię tych struktur można łatwo modyfikować poprzez dobór odpowiedniej proporcji molowej reagentów oraz czas reakcji. W podrozdziale 4.5 opisana została kinetyka reakcji syntezy mikrokwiatów. Zaproponowano również mechanizm wyjaśniający przemiany morfologiczne, jakim cząstki te ulegają w czasie. Podrozdział 4.6 zawiera natomiast opis praktycznego zastosowania mikrokwiatów. Zaobserwowano, że te pofałdowane złote cząstki tworzą stabilne pokrycia na powierzchni ciał stałych i wykazują silne wzmocnienie sygnału Ramana. Cechy te czynią je przydatnymi narzędziami w otrzymywaniu platform analitycznych do SERS. W podrozdziale 4.6 zamieszczono opis metody wytwarzania nowej, czułej i powtarzalnej platformy do SERS oraz przetestowano kilka jej modyfikacji.

1 Introduction

1.1 Nanotechnology

The belief that in order to reach higher and farther one should first look around and understand the mechanisms that govern everyday phenomena has been accompanying people for centuries. It resulted in the development of chemistry and physics, which has deepened our understanding of the structure of matter. For scientists, however, simple understanding of the mechanisms that govern molecules, or even the sight of a single atom, is not enough. We want to *create* matter to build tools and machines of desired properties from the smallest building blocks. We want to put targeted therapeutic capsules into the thinnest blood vessels, detect a single molecule of toxin in a biological sample and store all the published knowledge on a data storage medium no bigger than a pinhead. It is obvious that the approach that leads to the achievement of the greatest goals is minimization. The engineering of nano-sized objects is classified today as a separate branch of knowledge – nanotechnology. According to the IUPAC definition, nanotechnology focuses on objects that have at least one dimension in the range of 1 – 100 nanometers. This includes the design, fabrication, and use of the nanomaterials.

Nowadays, nanotechnology allows the production of particles of various shapes from a range of materials. One can classify these particles with respect to their dimensionality. The smallest, nearly spherical particles are called conventionally zero-dimensional objects. They are, for example, semiconducting quantum dots, nanopores, or fullerenes. Among elongated, one-dimensional structures, one should mention nanotubes, nanorods, nanobelts, nanowires, nanowhiskers, or nanochains. Representatives of a third group, namely flat two-dimensional structures, are: graphene, Langmuir-Blodgett films, nanoplates, or monolayered coatings composed of nanoparticles (NPs). To the 3D structures belong larger NPs (spherical and polyhedral), branched nanostructures, nanodumbbells, nanodendrites, hollow NPs (spheres, cages, and frames), or more complex arrangements of the mentioned shapes.[1,2] It is worth noting that, typically, distinguishing between “small” 0D and “bigger” 3D spherical NPs is rather conventional and does not refer to the precise guidelines given in some publications.[3] The aforesaid nanostructures can be prepared from various materials,

including inorganic semiconductors,[4] metals (also magnetic ones),[5] and insulators. Typically, materials such as ZnS, CdS, ZnO, TiO_2, GaAs, Au, Ag, Fe, C, or SiO_2 are used. Also commonly used are NPs built of two or three types of materials that can be distributed uniformly over the entire volume of the particle, or divided into core-shell domains. It is also worth adding that plenty of nanostructures have to be, at least at the stage of synthesis, covered by an organic protecting shell. The layer of covalently or non-covalently bound ligands prevents the aggregation of neighboring particles and determines the chemical and physical properties of the nanoobject. For example, gold nanoparticles (AuNPs) are usually protected by long-chained thiols, but also disulfides, selenium compounds, amines, or carboxylic acids.[2,6] Molecules of thiols bind to gold with their sulfur atoms and, when their amount is sufficient, form an ordered monolayer on the surface of the AuNP (Figure 1). The hydrophobic chains of the adjacent molecules are oriented parallel to each other, while the entire molecule of the ligand is almost perpendicular to the surface of gold. This type of self-assembled organic structure is called a self-assembled monolayer (SAM).[7]

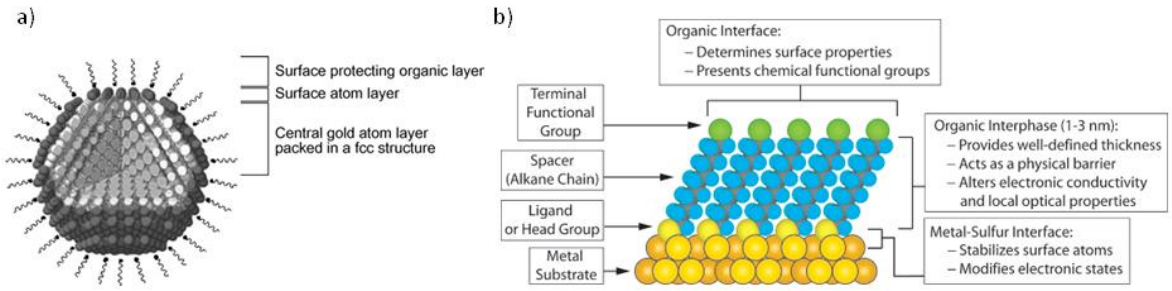

Figure 1 (a) Structural model of a single spherical AuNP, presenting organization of the gold atoms and the protecting layer of the ligand.[8] (b) Schematic diagram of an ideal SAM of alkanethiolates supported on a surface of AuNP.[7]

The choice of the protecting ligand is important because it determines the stability, solubility, and reactivity of the whole NP. For example, adequate functionalization of the surface of an inorganic NP can make it quasi-organic and biocompatible. Such functionalized NPs are used in medicine and biology and are called nano-biomaterials.[9] Their functionalization can add some biological functions or physical properties to the NP. An example of the former is the covering of the NP with polyethylene glycol, thus slowing recognition of the NP as a foreign body by the immune system, namely – its opsonization and phagocytosis.[10] It is also an attachment to the surface of NP antibodies, making NPs useful in immuno-tests[11] or allowing their directed distribution in living organisms. The latter type of modification – the addition of some

physical properties – can be carried out by covering with fluorescent ligands, thus enabling *e.g*. the tracing and optical detection of NP. It is also worth noting that often two or more types of ligands are present on the surface of a nano-bioparticle to provide its biocompatibility, stability, and bioactivity. Citing Ref. 9, proper functionalization makes nano-bioparticles useful in fluorescent biological labeling,[12] drug and gene delivery,[13] biodetection of pathogens,[14] detection of proteins,[15] probing of DNA structure,[16] tissue engineering,[17] tumor destruction via heating (hyperthermia),[18] separation and purification of biological molecules and cells,[19] magnetic resonance imaging (MRI) contrast enhancement,[20] or phagokinetic studies.[21] The wide spectrum of applications, possible thanks to the proper functionalization of the appropriate NPs, has led to the development of many commercial nano-bio-products. A sample list is presented in Table 1.

Table 1 Examples of commercialized nanomaterials for biology and medicine.[9]

Company	Major area of activity	Technology
Advectus Life Sciences Inc.	Drug delivery	Polymeric nanoparticles engineered to carry anti-tumour drug across the blood-brain barrier
Alnis Biosciences, Inc.	Bio-pharmaceutical	Biodegradable polymeric nanoparticles for drug delivery
Argonide	Membrane filtration	Nanoporous ceramic materials for endotoxin filtration, orthopaedic and dental implants, DNA and protein separation
BASF	Toothpaste	Hydroxyapatite nanoparticles seems to improve dental surface
Biophan Technologies, Inc.	MRI shielding	Nanomagnetic/carbon composite materials to shield medical devices from RF fields
Capsulution NanoScience AG	Pharmaceutical coatings to improve solubility of drugs	Layer-by-layer poly-electrolyte coatings, 8–50 nm
Dynal Biotech		Magnetic beads
Eiffel Technologies	Drug delivery	Reducing size of the drug particles to 50–100 nm
EnviroSystems, Inc.	Surface desinfectsant	Nanoemulsions
Evident Technologies	Luminescent biomarkers	Semiconductor quantum dots with amine or carboxyl groups on the surface, emission from 350 to 2500 nm
Immunicon	Tarcking and separation of different cell types	magnetic core surrounded by a polymeric layer coated with antibodies for capturing cells
KES Science and Technology, Inc.	AiroCide filters	Nano-TiO2 to destroy airborne pathogens
NanoBio Cortporation	Pharmaceutical	Antimicrobal nano-emulsions
NanoCarrier Co., Ltd	Drug delivery	Micellar nanoparticles for encapsulation of drugs, proteins, DNA
NanoPharm AG	Drug delivery	Polybutilcyanoacrylate nanoparticles are coated with drugs and then with surfactant, can go across the blood-brain barrier
Nanoplex Technologies, Inc	Nanobarcodes for bioanalysis	
Nanoprobes, Inc.	Gold nanoparticles for biological markers	Gold nanoparticles bio-conjugates for TEM and/or fluorescent microscopy
Nanoshpere, Inc.	Gold biomarkers	DNA barcode attached to each nanoprobe for identification purposes, PCR is used to amplify the signal; also catalytic silver deposition to amplify the signal using surface plasmon resonance
NanoMed Pharmaceutical, Inc.	Drug delivery	Nanoparticles for drug delivery
Oxonica Ltd	Sunscreens	Doped transparent nanoparticles to effectively absorb harmful UV and convert it into heat
PSiVida Ltd	Tissue engineering, implants, drugs and gene delivery, bio-filtration	Exploiting material properties of nanostructured porous silicone
Smith & Nephew	Acticoat bandages	Nanocrystal silver is highly toxic to pathogenes
QuantumDot Corporation	Luminescent biomarkers	Bioconjugated semiconductor quantum dots

There are many methods for fabrication of NPs. They can be classified into two major types: "top-down" and "bottom-up" approaches (Figure 2). The first type includes physical methods involving the milling, cutting or shaping of the bulk material into a nano-structured one. Reduction of the sizes requires expensive equipment, and takes place through sputtering, pulsed laser deposition, laser and ion-beam ablation, thermal evaporation, high energy ball milling, or nanolithography.[22] The "bottom-up" approach is in turn a Nature inspired way of creating nanostructures from small elements, like atoms. Here, wet-chemical methods are mainly used that are simple and convenient from the economic point of view. If required, the next level of the "bottom-up" method is implemented, *i.e.*, fabrication of more complex structures (ordered layers or 3D arrangements) with the use of the NPs as building blocks.

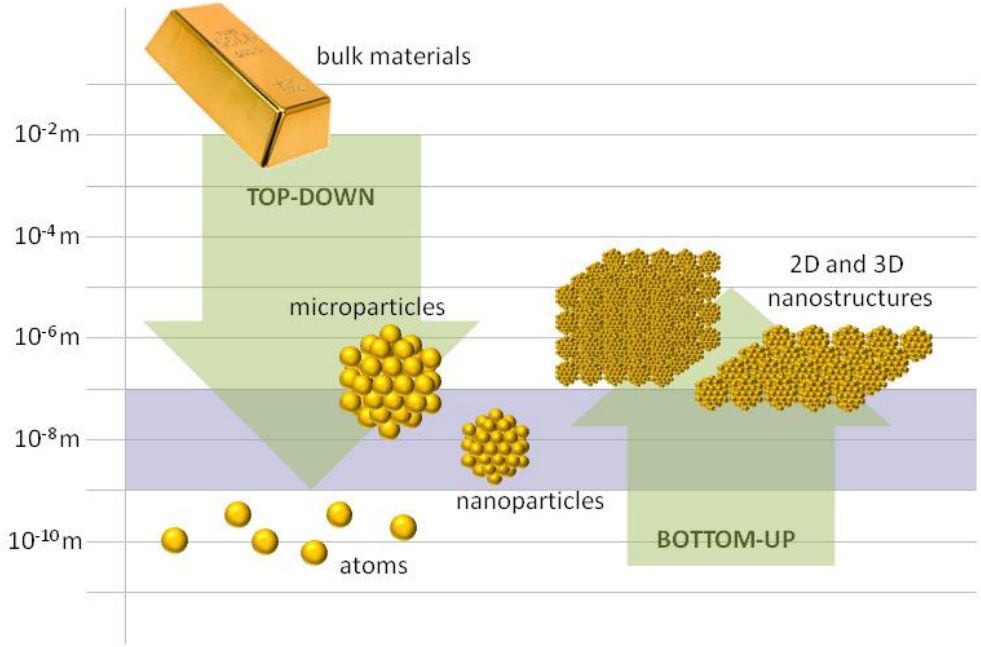

Figure 2 Cartoon illustrating two approaches to nanostructures preparation. The green arrows indicate the "top-down" method - from bigger to smaller objects, and the "bottom-up" approach - from smaller to bigger objects. The violet area corresponds to the nano-range. Image inspired by Ref. I on page 150.

1.2 Unique properties of NPs resulting from their size and shape

NPs are a popular subject of current research because of their extraordinary properties that significantly differ from those of atoms and bulk material of the same chemical composition. One can observe *i.a.* differences in color, transparency, melting point, hardness, conductivity, and reactivity. The exemplary untypical particular properties of nanomaterials are: conductivity, flexibility and strength of carbon nanotubes in contrast to features of coal, the navy blue color of AgNPs in contrast to the

metallic grey of bulk silver, transparency of ZnO NPs as opposed to its white bulk analog, or the catalytic properties of AuNPs, not observed for metallic gold. Apparently, by decreasing the diameter of a grain of material to the nano-scale, one changes not only its geometry, but also its chemical, optical, electrical, and magnetic features. These properties are then unique and hard to predict - they cannot be simply anticipated by extrapolating the properties of their bulk counterparts.[1]

The differences in optical properties exhibited by bulk materials and their nano-analogs result from the sizes of the nanoparticles that are often of the same order as their de Broglie wavelengths. In such cases the particles behave as zero-dimensional quantum dots (QDs) and their properties are described by the rules of quantum mechanics.[8] The dependence of the optical properties on the size is particularly visible in the case of semiconducting materials. In a bulk semiconductor, the absorption of a photon of energy equal or greater than the characteristic band gap energy (E_g) results in excitation of an electron from the valence to the conduction band. The positively charged orbital hole in the valence band and a negatively charged electron in the conduction band state an electrically neutral quasiparticle called an exciton.[23] Depending on the material, the size of the exciton expressed by the Bohr exciton diameter (d_B), varies from 1 nm to more than 100 nm. The spatial confinement of an exciton in the particle (often compared to a box) smaller than the exciton itself raises its energy.[23] Consequently, for grains of material smaller than d_B the absorption and fluorescence spectra, and – therefore – their color, strongly evolves with the size of the limiting box (Figure 3a and Figure 3c). The feature directly dependent on the size is here the electronic structure of the semiconductor NPs. In Figure 3b a chart of the electron structure of semiconductors is shown. Considering the increasing size of the object, one observes that discrete energy levels typical for single atoms or molecules evolve into continuous broad energy bands for bulk material. The decreasing of band gaps can also be clearly seen. For example, by varying the size of CdS from a single molecule to a macroscopic crystal, one can observe the evolution of the band gap from 4.5 eV to 2.5 eV.[24] Electronic states typical for QDs are, like their sizes, somewhere between molecules and bulk material. They exhibit a discrete structure of levels, like those observed in single molecules, but of much higher density, similar to bulk. The characteristic band gap of semiconducting nanomaterials is akin rather to the molecule's band gap, but strictly depends on the size of the particle. A slight increase of the size of

the QD results in a strong decrease of the band gap, which is reflected in a change of the color of QDs' suspension (Figure 3a). This easy control of the emitted fluorescent light across the whole visible spectrum makes QDs useful in many types of optoelectronic devices.[23]

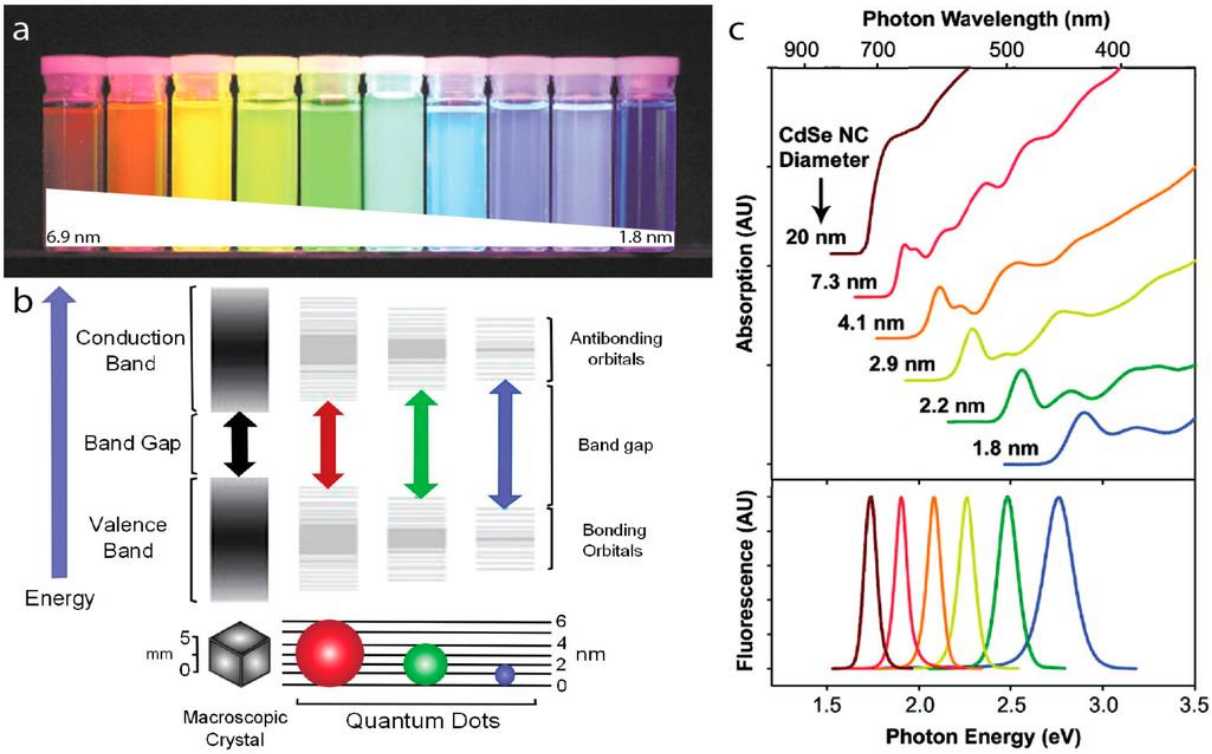

Figure 3 (a) CdSe/ZnS core/shell QDs with CdSe core diameters ranging from 6.9 nm to 1.8 nm in diameter. Presented QDs emit with peaks from 1.9 to 2.8 eV (655–443 nm) from left to right under UV illumination. (b) Schematic illustration of electronic structure of semiconductors. Electronic structure of quantum dots is an intermediate between single molecules and bulk materials. (c) Absorption (top) and emission (bottom) spectra of CdSe quantum dots. Source of the image: Ref. II on the page 150.

In the world of NPs, the shape of the particle also influences its optical properties. In macroscale, elongated, spherical or flat objects of the same chemical composition have the same color. Describing QDs, however, one should consider their various shapes as different shapes of the quantum confinement. From the various shapes of these "boxes", different absorption spectra result. In the above paragraph spherical QDs were described. They are systems where electron motion is confined in three dimensions. In the case of flat quantum wells, the electrons are confined in two dimensions; for elongated quantum wires – in one dimension.[25] Every type of confinement is characterized by a different density of states (Figure 4a) and different band gap (Figure 4b), predetermining the optical properties of QDs of different shapes. In Figure 4b the shift of the band gap of CdSe for quantum dots, wires, and wells is presented. It can be

seen that increasing the number of confined dimensions results in a wider range of tunability in the band gap.[23]

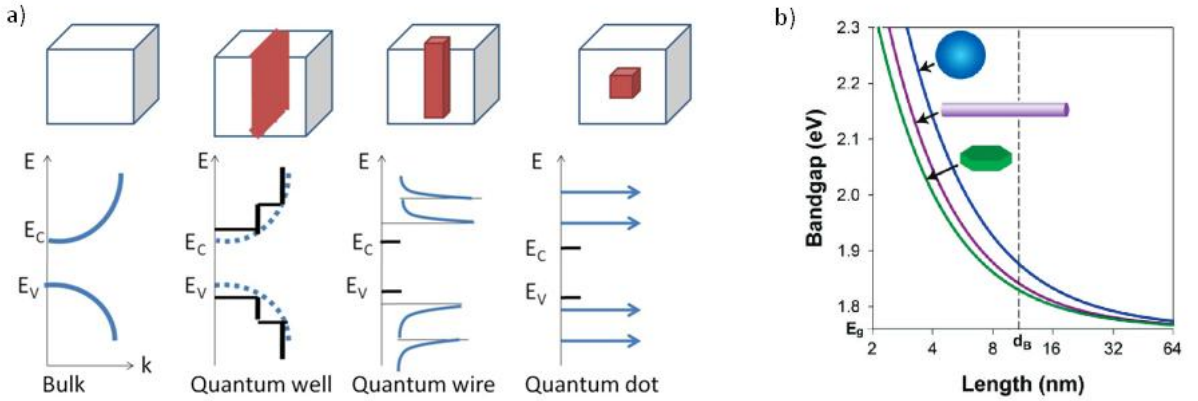

Figure 4 (a) Evolution of density of states for systems of different confinement: bulk, quantum well, quantum wire, and quantum dot. When the electron motion is restricted in more dimensions, the conduction and valence bands split into overlapping, successively narrower subbands.[25] (b) Impact of shape on the electronic properties of CdSe QDs. On the axes the band gap (E_g) and the diameter of the exciton (d_g) for bulk material are marked. Band gaps of the QDs of different shapes are plotted against the length of the confinement dimension. Thicknesses of the wire and the plate are fixed.[23]

From the small size of the NPs also result their other interesting features. Considering objects of several nanometers in diameter, one should keep in mind their discrete, atomic structure, shown in Figure 1a. The appreciable part of the atoms building the NP, state the ones on its surface. Although built like the others, they exhibit slightly different properties from the atoms located inside the particle. First of all, they have low coordination numbers, which make them responsible for the reactivity of the whole NP. This feature is particularly useful in catalysis – smaller particles, of the high surface atoms to bulk atoms ratio, are generally better catalysts than their bigger analogs. The catalysis is, however, a quite complex phenomenon that depends not only on the number of the catalysts atoms exposed to the reaction mixture. Primarily, by decreasing the size of the NP, one changes also other properties of the material, often in an unpredictable way. It is, for example, known that AuNPs smaller than 2 nm lose their metallic nature and become worst catalysts (Figure 5).[26] The NP size can influence also the binding affinity of the substrate and product, the surface-restructuring-coupled catalytic dynamic, or differential selectivity of the NP between parallel product dissociation pathways.[27]

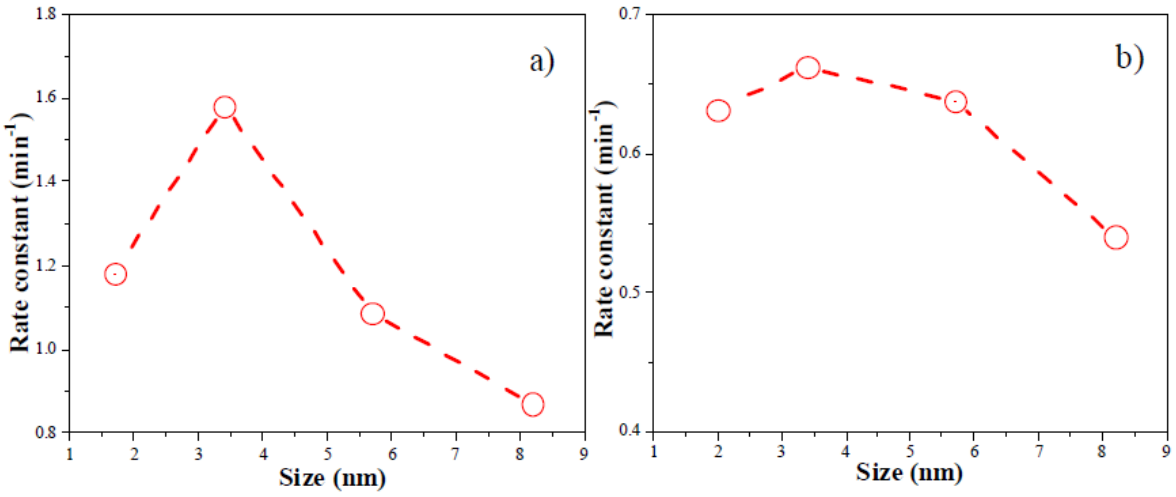

Figure 5 (a) Correlation between the reaction rate constant and the size of the catalyst. Data for the reduction of *p*-nitrophenol with $NaBH_4$ using colloidal AuNPs as the catalyst are shown. (b) An analogous graph for Au/Al_2O_3 catalyst.[26]

Low coordination numbers also result in higher mobility of the surface atoms and influence stability of the whole NP.[23] Thermodynamically, the most stable are spherical particles – their surface-to-bulk atoms ratio is smaller than for elongated or flattened ones. This is yet another example that not only size, but also the shape of the NP determines its properties. In Figure 6 the relation of surface atoms number on NP size and shape is presented. The number of surface atoms affects also other material properties. Namely, when the size of a particle decreases and – consequently – the fraction of surface atoms increases, the melting temperature of the material decreases. Because the number of surface atoms is proportional to the number of ligands that can be attached, by decreasing the particle size one decreases the "ligand/particle" ratio but increases the "ligand/mass of the material" ratio. This is of particular importance in the case when ligands not only protect particles from aggregation, but also provide an electrical charge or are responsible for other physical, chemical, or biological functions. Changing the size and shape of the NPs, one changes also the curvature of their surface, dominating crystallographic planes or diffusive kinetics. All these parameters will influence the range of potential applications of the nanoobject.

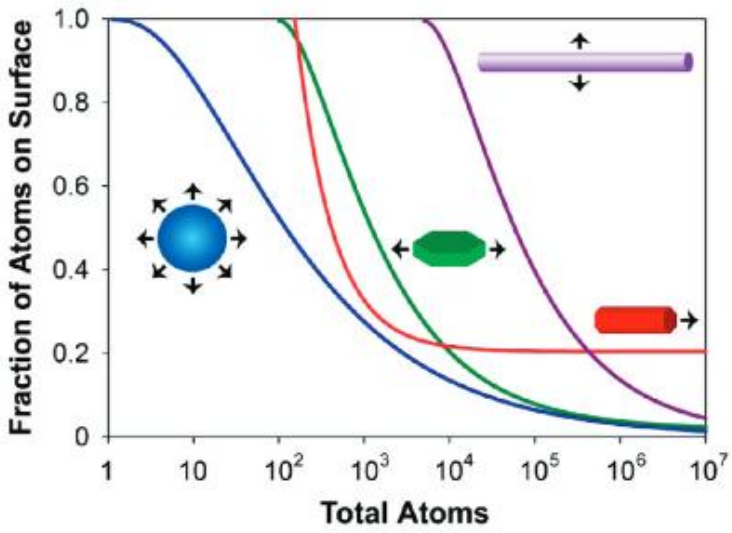

Figure 6 Impact of size and shape on the fraction of the surface atoms. Constant dimensions: the purple wire is 1 μm in length, the green disk is 20 nm high, the red rod is 4 nm in diameter.[23]

1.3 Gold nanoparticles

Gold possesses unique properties that have attracted interest since the most ancient times. People have always appreciated the natural purity of gold, its incorruptibility and ductility, while its scarcity and beauty have aroused a desire for it into the present day. Because of its nobleness, gold was considered to be a product of the gods and due to rulers and deities. The solid form of gold was used in jewelry and the production of other decorative pieces.[8]

In modern science gold is present mainly in its colloidal form, meaning suspensions of AuNPs. These AuNPs are the most stable metal NPs[6a] and can be synthesized in a wide range of sizes and shapes. The observable acceleration of studies of AuNPs and exponentially increasing number of articles is correlated with advances in analytical methods (especially electron and atomic force microscopy) that have taken place in recent decades. Although colloidal gold was being used already before Christ, mainly for production of ruby glass and for curative purposes, the development of research into its physical and chemical nature falls on the 19th century and is associated with the work of such scientist as Alphonse Buisson, Michael Faraday, Henry Debray, and Richard Adolf Zsigmondy.[28]

This great interest in AuNPs is due to their interesting properties, so different from the features of bulk gold. The difference, which can be seen at first glance, is the color. Unlike the macroscopic state, colloidal gold is usually red or purple. This is a consequence of localized surface plasmon resonance (LSPR) occurrence. This

phenomenon is also responsible for a slight change of color (and different optical and electrochemical properties) with the change of size, shape, and distance between neighboring NPs. For various nano-morphologies, the LSPR electric field is confined within various metallic boxes (particles), and interacts with the incident light in various ways. The optical properties of AuNPs are described in more detail in section 1.4.

In contrast to chemically inert macroscopic gold, the AuNPs exhibit interesting chemical reactivity. This is a consequence of (typical of all nanoobjects) the high ratio of surface to bulk atoms. When the size of a particle decreases, the fraction of surface atoms increases, so about 60% of the atoms of the AuNP having 2 nm in a diameter are surface ones. Having few neighboring atoms (low coordination number), the surface atoms can vibrate around their normal locations. As a consequence, the surface of the nanoparticle exhibits reactivity which differs from that of bulk gold. In particular, it possesses strong catalytic activity. The exemplary reactions catalyzed by the AuNPs are: oxidation of carbon monoxide (CO), synthesis of hydrogen peroxide (H_2O_2), hydrogenation of carbon-carbon multiple bonds, and selective oxidation of organic molecules.[8] Another consequence of the high content of surface atoms in the NPs is a change in the melting point in comparison with the bulk material. For 2 nm AuNPs it is a decrease from 1337 to about 600 K.[8]

Catalysts based on AuNPs are used, among others, in the environmentally important elimination of CO and nitrogen oxides. In these reactions, both colloidal gold and AuNPs supported on oxides (*e.g.* on TiO_2, Fe_2O_3, NiO, Al_2O_3, SiO_2) are used.[29] Many effects can contribute to the catalytic activity of the AuNPs. First of all, as was mentioned, is the size of the particle. In Figure 7a a correlation between CO oxidation activity and the diameter of the AuNPs is presented.[29] It can be seen that the oxidation rate for the smallest (2-3 nm) particles is about two orders of magnitude larger than for 20 nm AuNPs. The second factor in the hierarchy of contributions to catalytic activity is a high concentration of low-coordinated sites, depending on the particles' size and shape. The low-coordinated gold atoms exhibit higher Au-O binding energies, stronger than O-O bonds, allowing dissociation of O_2 and efficient oxidation of CO (Figure 7b).[29] Also the strength of the Au-CO bond depends strongly on the coordination number of Au. For the Au(111) surfaces, where every gold atom has 9 neighbors, atoms' *d* states are too weak to interact strongly with the O 2*p* valence states. For atoms in an Au_{10} cluster having a coordination number of 4, in turn, the CO and O adsorption energies are

lowered by up to 1 eV. As a result, at a pressure of 1 bar and at 300 K, the coverage of the gold catalyst by CO increases from 10^{-13} for the Au(111) surface atom to ~ 1 for the atom with the coordination number of 4.[29] From this, one could assume that only the corners of the AuNPs are responsible for their catalytic activity.

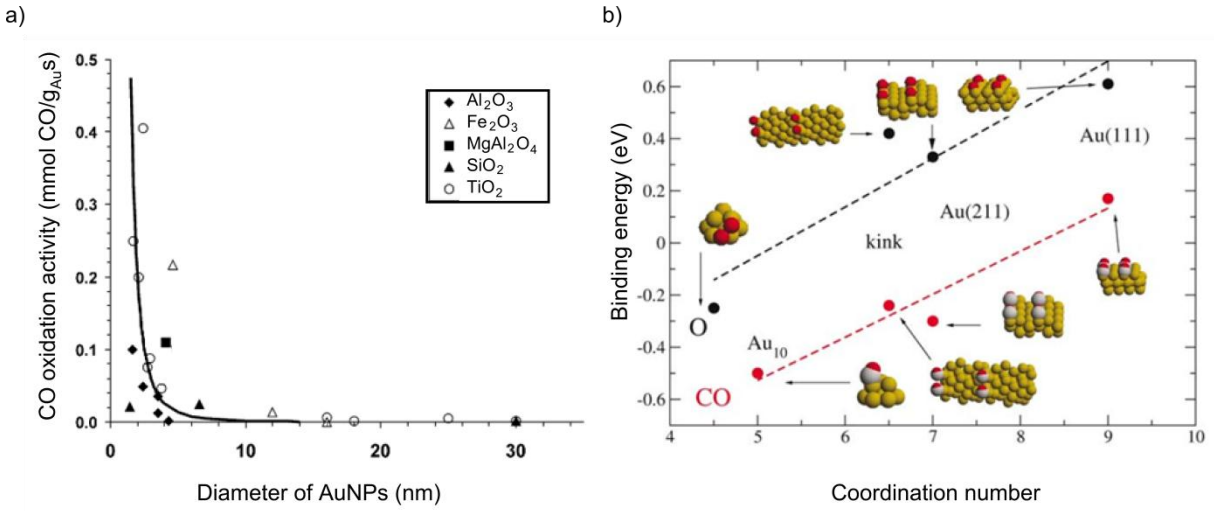

Figure 7 Data collected for oxidation of CO at 273 K over different Au-based catalysts. (a) Measured oxidation activities as a function of the average catalyst grain size, on various supports. The curve is a guide to the eye corresponding to $1/d^3$. It shows that the activity of the catalyst depends on the number of low-coordinated atoms at the corners of the AuNPs. (b) Binding energy as a function of the coordination number of Au atoms in various configurations. Binding energies are referred to gaseous CO and O_2; for O_2 the values are given per one O atom.[29]

The next factor contributing to the catalytic activity of the AuNPs is related to support. In Figure 7a the oxidation activities for particles of gold catalyst supported on various oxides are shown. Comparing the reactivity of a catalyst of the same diameters but supported on various oxides one can deduce that reactivity for the reducible oxides (TiO_2, Fe_2O_3) is higher than for irreducible (Al_2O_3, $MgAl_2O_4$, SiO_2) ones by a factor of 2-4. According to Ref. 30, the reducible oxide supplies oxygen which then forms then an active site of the gold catalyst. In literature one can find also other factors of a similar level of contribution, like *e.g.* the intrinsic particle size, the effect of metal-insulator transitions, the effect of charge transfer, and the strain effect, listed and briefly described in Ref. 29.

Due to the properties mentioned above, combined with the ease of chemical functionalization, AuNPs can be utilized in many branches of technology. Besides catalysis, these particles are used in industry in soldering pastes and conducting thin films.[8] Because of the oxidation resistance of the thin gold coatings, transparency to visible light, and high reflectivity in infrared radiation frequencies, AuNPs are also used in the production of spectrally-selective surfaces (*e.g.* glass) blocking IR waves. Like

centuries ago, the purple colloidal gold can be also employed to stain textiles, glass, or ceramics. In medicine, AuNPs play an important role in diagnosis and therapy. Diagnosis is based on the LSPR sensing methods or on usage of the AuNPs as contrast agents in bio-imaging. Therapy utilizes *i.a.* the photothermal properties of AuNPs, applying NPs as nanoscale heat sources under light irradiation, or uses them as targeted drug carriers.

1.3.1 Synthesis of spherical gold nanoparticles

In the 20th century various methods for the synthesis of AuNPs were developed. Generally, they are bottom-up methods consisting of reduction of gold cations in the presence of a capping (protective) agent. The oldest of the most popular, and still commonly used, was reported by Turkevich[31] in 1951 and refined by Frens[32] twenty two years later. This one-pot method involves the citrate reduction of the auric acid, $HAuCl_4$, in water. Trisodium citrate acts as a reducing agent for Au^{3+} ions and a capping agent for the newly formed AuNPs, preventing them from aggregation. The appropriate molar ratio of two reagents can lead to the synthesis of AuNPs in the 10-150 nm size range, but the best monodispersity is achieved for those AuNPs having from 10 nm to 20 nm in diameter. This method, however, has been being continuously improved since the 1970s, and many modifications of the original Turkevich protocol have been published to date.[33]

The second groundbreaking synthesis method was published in 1994 by Brust *et al*. (the Brust-Schiffrin method)[34] and gave the opportunity to synthesize AuNPs of reduced dispersity and controllable size. In this method one can obtain small (diameters < 5.5 nm), thiolate-capped AuNPs soluble in organic solvents. The original two-phase synthesis protocol uses $HAuCl_4$ as a source of gold ions, tetraoctyammonium bromide (TOAB) as the phase-transfer agent, sodium borohydride as a reducing agent, and dodecanethiol (DDT) as the capping agent. Since TOAB also acts as a weak capping agent, the method can be slightly modified: instead of adding DDT to the reaction mixture, one can isolate NPs covered with TOAB and then replace this weakly bound ligand with a desired compound. The Brust-Schiffrin synthesis without the addition of DDT is presented in Figure 8.

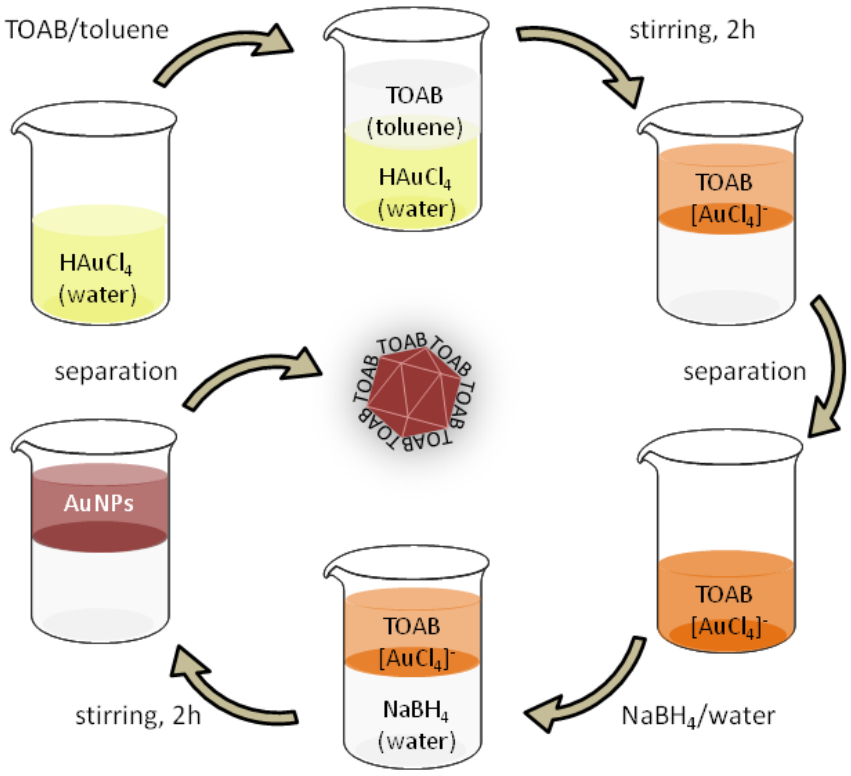

Figure 8 Synthetic steps in the two-phase Brust-Schiffrin synthesis of AuNPs. Image inspired by Ref. III on page 150.

To date, dozens methods for the synthesis of AuNPs have been developed and plenty of stabilizing ligands, imparting desired chemical and physical properties, have been applied.[2,6,8] Besides the liquid-phase chemical methods, electro-, photo-, and sonochemical, microwave-assisted or radiolytic methods are used. Generally, they lead to a less contaminated product than chemical methods do, but are not as convenient to parameter control or scale enlargement.[8]

1.3.2 Synthesis of non-spherical particles

Spherical NPs are the most commonly used and synthesized types of gold nanoobjects, but we can also distinguish another, anisotropic morphologies of nanostructures. Among them, typically used are nanorods, less often nanoplates (usually triangle or hexagonal flat prisms), nanowires, branched structures, nanocubes, and dumbbells (sample shapes are shown in Figure 9). Although each year new methods for synthesis of nanostructures are published, controlling the morphology of non-spherical particles is still challenging. The reason is a weak understanding of the processes that govern the formation of particular shapes of a desired size and aspect ratio.[35] Consequently, one usually obtains a mix of shapes as a product of the synthesis.

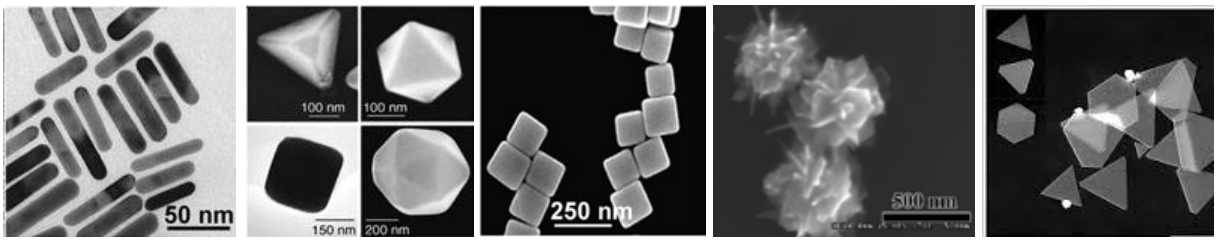

Figure 9 TEM and SEM images showing various types of AuNP morphologies.[35,135,172]

There are, however, some empirical rules of thumb that help in the planning of anisotropic particles synthesis. First of all, the process of formation of these structures should be a two-step seeding approach. In the first step, gold nanospheres are synthesized and then, in the second step, the spheres are grown into particles of desired shapes. While the first step should be a rapid synthesis, with a fast growth of all crystal surfaces, the growth stage is much slower, proceeds under milder reducing conditions, and is controlled by the composition of the growing mixture.

The second rule is the addition of shape templating surfactants, halides or silver ions, of experimentally proved influence on the selective growth of particular gold facets, to the growing reaction mixture. For example, it can be observed that the addition of silver ions promote formation of gold nanorods. There is no commonly accepted mechanism explaining how shape control works, but it is widely believed that silver atoms block the Au (110) surface, inhibiting its further growth. The gold nanorod tips, comprised of (100) facets, grow relatively faster, leading to the formation of a one-dimensional product.[35] Interestingly, this silver-promoted mechanism works for seeds capped by cetyltrimethylammonium bromide (CTAB) ligands, but for seeds protected with citrate this leads to the formation of bipyramidal NPs.[36] A hypothesis about the blocking of the particular crystallographic planes is also used for halides. These additives, in turn, probably strongly bind to (111) facets and block their growth, leading to the formation of nanoplates.[37] It is noteworthy that, to date, the synthesis of gold nanorods is relatively well studied and allows for 90% reaction yields, while nanoplates represent usually no more than 40% to 65% of a product and vary in size and shape.

According to the third rule, gold nanoseeds used in the growing procedure should be as uniform as possible. This requirement is, however, difficult to meet because the shape called a “nanosphere” is represented by a group of about twenty different shapes (Figure 10). Potentially each of them can grow in a different manner, leading to the formation of various products of the same reaction. In practice, two shapes prevail in the

population of small nanospheres: icosahedrons and decahedrons. This fact makes selective production of anisotropic particles feasible.

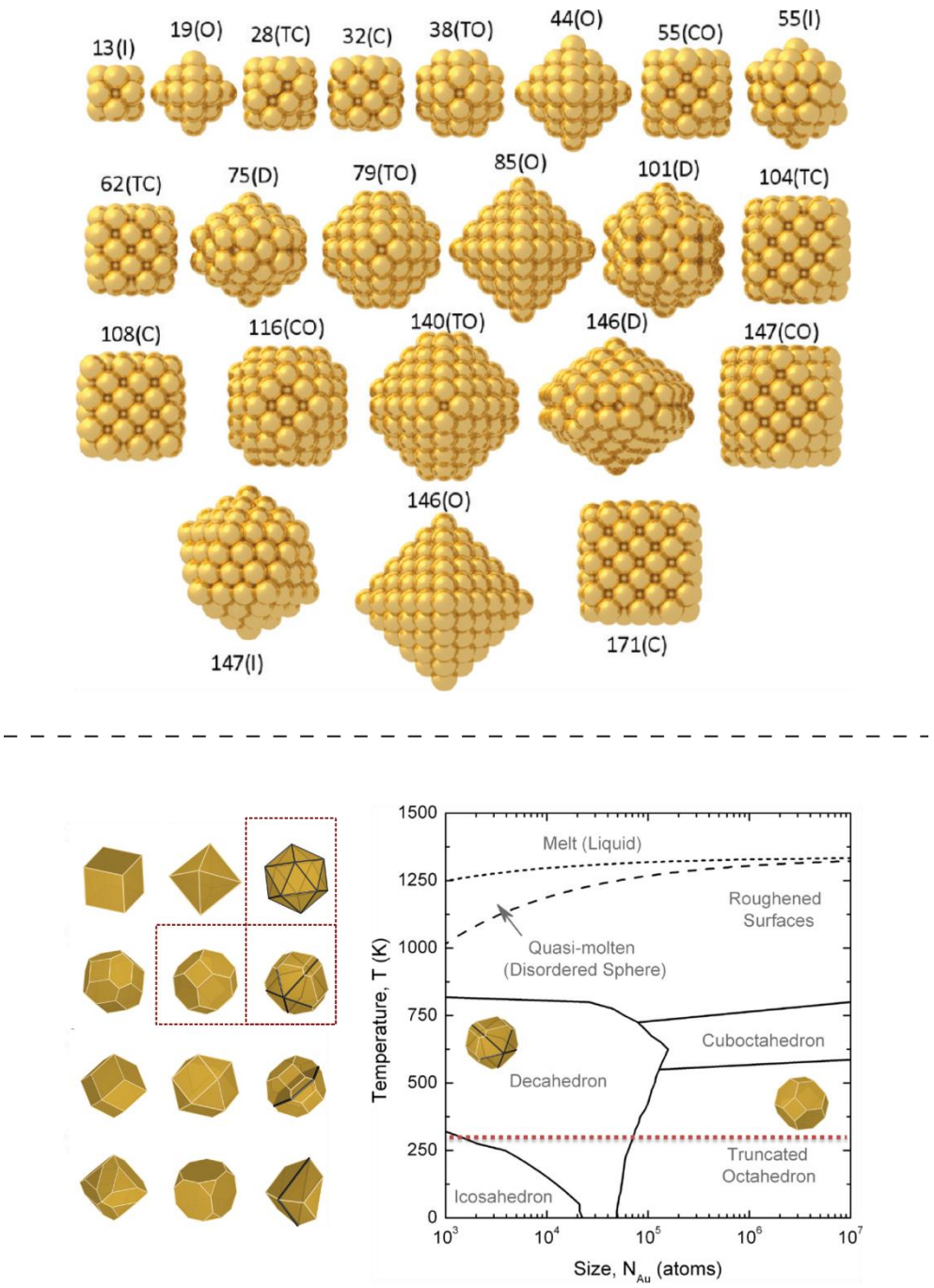

Figure 10 Upper image: Possible shapes of AuNPs built from less than 200 atoms, 1 – 3 nm in diameter. *N*(X) denotes the size and shape, where *N* is the number of atoms, and I = icosahedron, O = octahedron, TO = truncated octahedron, CO = cuboctahedron, TC = truncated cube, C = cube, and D = decahedron. Theoretically predicted stability: TO > O > TC > CO.[38] Bottom image: Thermodynamically preferred structures containing more than 10^3 gold atoms. Red dotted line on the phase diagram shows room temperature (rt) and, on the structures gallery, the most common morphologies present in rt.[39,40]

In the study described in this dissertation, mainly spherical and flower-like particles are presented. The latter are classified as branched particles, together with

multipods, nanostars, and urchins. They are synthesized in one-step or multi-step routes and usually require untypical additives or non-spherical seeds. Gold branched NPs have so far been applied in biosensing, imaging, photothermal therapy, and targeting.[2]

1.3.3 Functionalization of gold nanoparticles

In the case of AuNPs, every chemical wet synthesis of the NPs results in an immediate covering of gold with compounds present in the reaction mixture. There could be some factors used as surfactants or as reducing agents for the gold salt, like organic acids or amines. Sometimes such ligands are inorganic and very small, like hydroxyl groups[41] or oxoborates[42]. More often, however, the AuNPs are covered by tailored ligands, giving them desired physical, chemical, and biological properties. Those ligands usually are thiols because of their ability to form a covalent bond between gold and sulfur atoms. Thiols consist of a sulfur atom (S) responsible for the bonding and an organic group (R) conferring the properties to the AuNP. Other sulfuric derivatives used in the functionalization of AuNPs are xanthates, thioethers, and disulfides. These ligands can be introduced to the reaction mixture in the stage of the formation of the AuNPs or deposited on the gold surface later, in a ligand-exchange reaction.

Because of its wide use, gold-sulfur bonding is the object of many studies.[43] This strong chemisorption has bond dissociation energy of (253.6 ± 14.6) kJ/mol, similar to the Au-Au bond [(226.2 ± 0.5) kJ/mol] (both values concern diatomic molecules).[44] For bulk gold or bigger NPs with large Au(111) areas, thiols are typically highly ordered into dense SAMs (see Figure 1b in the 1.1 section). These structures represent the standing-up configuration of ligands. For the most densely packed thiols, hydrocarbon chains adopt tilt angles of 30 degrees to 40 degrees in relation to the surface normal.[43c] Many investigations have shown that the structure of the Au-S interface on the surface of macroscopic gold is different from that on the small NP. On the curved surface of small AuNPs, compared with the flat Au(111), the surface coverage is typically higher and exceeds 33%. Also, on the AuNPs the chemical stability of the Au-S bond against thiolate degradation to disulfides is better. This results from the presence of surface defects, where thiolates are bonded more strongly.[43c]

The SAMs serve as external shells determining the properties of the surface, such as its wettability or adhesion. The structure of such layers was determined in the late 80s and early 90s by atomic force microscopy (AFM) and electron diffraction studies (EDS).[43b] The studies revealed that the sulfur atoms adopt the hexagonal structure of the

Au(111) surface underneath. The S-S distance in SAMs built of the alkanethiols was determined as 4.97 Å.[43b] As mentioned above, thiols are connected strongly to the gold, but the true nature of the Au-S bonding is still a subject of research. The standard Au-S binding model, shown in Figure 11a, is at present challenged by other shown binding modes. According to new experimental and theoretic data, in low- and medium-coverage SAMs an important structural unit may be a RS-Au(I)-RS staple complex.[43d] In this complex a bridging Au atom in a +1 oxidation state is present (Figure 11c). The sulfur atom, bound to two different gold atoms, the R group and the electron lone-pair, is here a stereogenic centre.

The RS-Au(I)-RS staple model is also currently proposed in describing the Au-S interface on the small gold clusters. In the work of Jadzinsky *et al.* a AuNP of 102 atoms, covered with 44 molecules of aromatic thiol (*p*-mercaptobenzoic acid, *p*-MBA), was investigated.[43a,e] It found that 79 of the gold atoms build an ordered, truncated-decahedral core with Au-Au bond lengths consistent with the bulk material, while the remaining atoms form a shell around the core. These outer atoms interact strongly with the thiolate sulfur atoms, as is schematically shown in Figure 11b, while the polar interaction of sulfur with the grand core was found to be much weaker. All sulfur atoms are located in a radius (8.3 ± 0.4) Å from the center of the gold cluster. Gold atoms located in a radius up to 5.5 Å do not contact sulfur atoms, those located 6.0 Å to 6.3 Å from the center bind to one sulfur, and atoms in a radius 8.0 Å bind with two sulfides. On the Au-S interface, monomeric SR-Au-SR staple motifs are present. Interestingly, for smaller gold clusters ($Au_{25}(SR)_{18}$ and $Au_{38}(SR)_{24}$), dimeric motifs of various steric configurations were also found (Figure 11d).[43b] Investigation of the Au-S interface between *p*-MBA and flat Au(111) gave, however, no evidence for gold ad-atoms, suggesting that the ad-atom structure is rather a feature of curved gold surfaces.[43c]

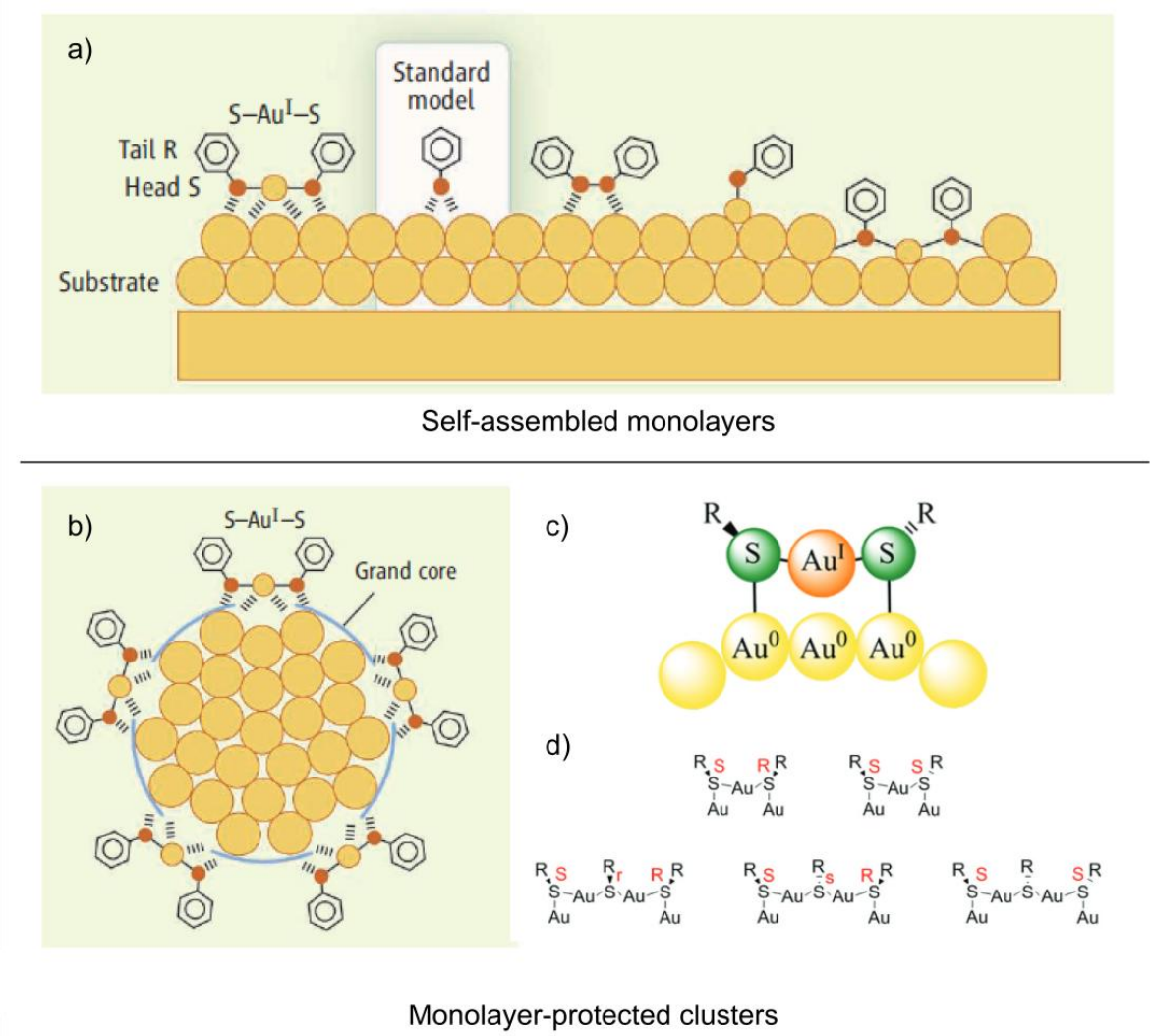

Figure 11 Schematic presentation of bonding motifs between thiols and gold. (a) Several suggested bonding modes for thiols on the close-packed gold substrates.[43a] (b) Aromatic thiol-protected gold nanocluster. Carboxylate groups of the *p*-MBA acid are not shown.[43a] (c) Monomeric RS-Au-RS staple motif. Regarding the orientation of the R substituents in relation to a staple plane, one distinguishes *cis* and *trans* isomers of the motif.[43b] Conversion between the two positions is easy due to a low energy barrier.[43d] (d) Stereochemistry of monomeric and dimeric staple motifs.[43b]

There is much evidence that the Au-S interface is neither rigid nor static.[43b] Thiolates can easily move on the surface of the AuNP or bulk gold, as well as disconnect from the surface and be replaced by other thiol molecules. For example, Imabayashi *et al.*[45] investigated two separated domains of different thiolates attached to gold and observed their complete mixing after 300 h at 60˚C. The experiments were conducted in water as well as in air. The authors estimated the diffusion coefficient of 10^{-18} cm^2/s which corresponds to about 1 nm per hour lateral diffusion. The diffusion of the thiolates on gold, on the other hand, can lead to formation of some domains from the homogeneous SAM. This is especially pronounced for mixed coatings, consisting of two or more different thiolates, on the AuNPs. After deposition, distribution of the mixed

thiols is rather random. Mobility of the thiols allows reaching a thermodynamic stability by, *e.g.*, a complete separation of the two types of ligand on two hemispheres of the AuNPs and the formation of so-called Janus particles.

Covering the AuNPs with ligands determines their interactions with the environment. The entire nature of these interactions depends on the chemical and steric properties of the ligands. In Figure 12 and Figure 13 sample ligands used in the functionalization of the AuNPs are shown. The cartoons present 5 nm gold cores and space-filling models of ligands drawn to scale.

A spherical NP coated with a dense shell of radially oriented molecules contacts its surrounding almost exclusively with the terminal chemical groups determining the NPs' solubility, charge, reactivity, affinity, *etc*. For example, the long-chained ligand *N,N,N*-trimethyl(11-mercaptoundecyl)ammonium chloride ($HS(CH_2)_{11}N(CH_3)_3^+Cl^-$, (abbreviation: TMA), despite its hydrophobic aliphatic chain, makes AuNPs entirely soluble in water. TMA itself dissolves only in organic solvents, but its $-N(CH_3)_3^+$ group is polar and, when oriented on the surface of the functionalized AuNP, makes it hydrophilic. The quaternary ammonium cation is also responsible for the positive charge of the TMA-coated AuNPs. The charge, naturally, affects various properties of the NP – it changes interactions between the NP and its environment as well as interactions with other NPs. For example, a solution of TMA coated NPs is stabilized not only via steric, but also electrostatic repulsion between organic ligands tethered to the adjacent NPs. The repulsion prevents the NPs from undesired aggregation and precipitation from the solution. Speaking of the NP-environment interaction one can also mention the electrophoretic mobility of the charged particles or their deposition on oppositely charged solids.

The surface charge also plays a key role in many applications of the NPs, for example in microbiology. It is known that negatively charged particles do not penetrate the surface of bacteria cells, which is also charged negatively. Positively charged particles, in turn, are able to get through the cell wall, disrupting it. This feature is nowadays being investigated as an antibacterial mechanism – in the face of the increasing drug resistance of pathogens, NPs are considered as a new class of antibiotics.[46] Interestingly, the highest antibacterial activity, combined with low toxicity against mammalian cells, is achieved for zwitterionic[47] or mixed, positive and negative,

ligands on the surface of the NPs. Their proper ratio increases the efficiency and can even lead to a Gram-selectivity of the NP-based new antibiotics.[48]

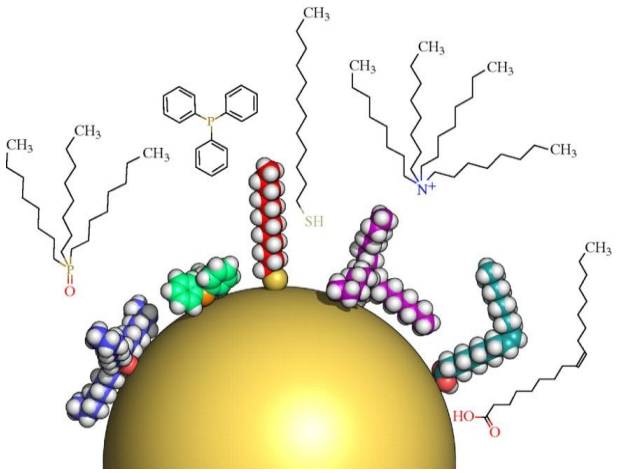

Figure 12 Hydrophobic ligands deposited on the surface of the NP of a 5 nm core diameter. The particle is idealized as a smooth sphere and only space-filling models are drawn to scale. Left to right: trioctylphosphine oxide (TOPO), triphenylphosphine (TPP), dodecanethiol (DDT), tetraoctylammonium bromide (TOAB), oleic acid (OA). Source of the image: Ref. IV on page 150.

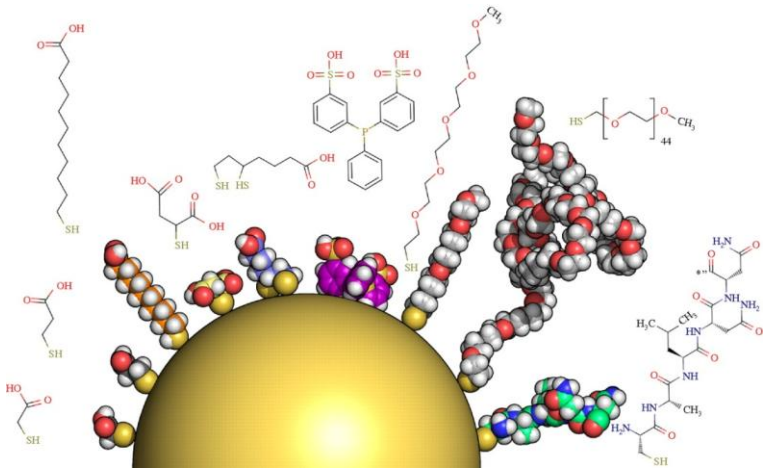

Figure 13 Hydrophilic ligands deposited on the surface of the NP of a 5 nm core diameter. The particle is idealized as a smooth sphere and only space-filling models are drawn to scale. Left to right: mercaptoacetic acid (MAA), mercaptopropionic acid (MPA), mercaptoundecanoic acid (MUA), mercaptosuccinic acid (MSA), dihydrolipid acid (DHLA), bis-sulphonated triphenylphosphine, mPEG5-SH, mPEG45-SH (2000 g mol^{-1}) and a short peptide of the sequence CALNN. Source of the image: Ref. IV on page 150.

The application of NPs in medicine sometimes involves their introduction into the human cardiovascular system. A method for their further removal from blood can also be based on the presence of the electric charge on the surface of the NPs. In 2015 engineers from the University of California proposed for this purpose a dielectrophoresis collection chip.[49] The chip is made of hundreds of electrodes generating a rapidly oscillating electric field and works efficiently even with the high salt

concentrations observed in human blood. A similar dielectrophoretic device could be also used in environmental and industrial applications in which NPs with a non-zero net charge are applied.

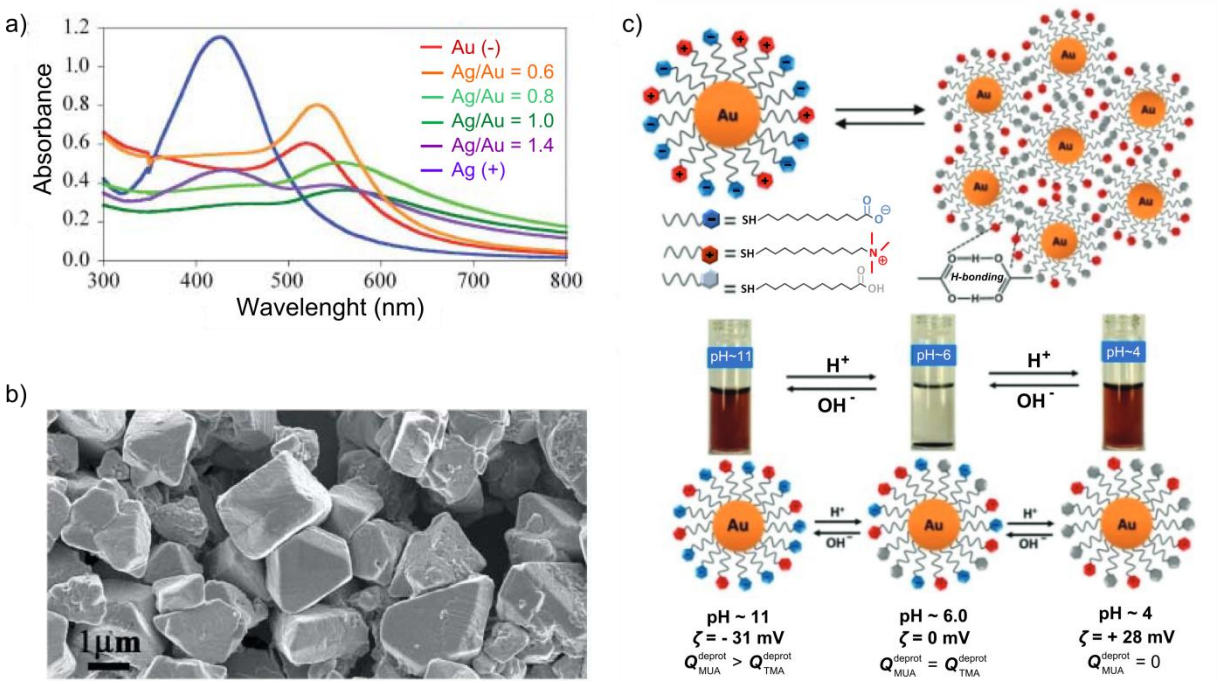

Figure 14 (a) The Uv-Vis spectra for the titration of Au(-)NPs with likely concentrated Ag(+)NPs solution. Precipitation, visualized as decreasing of the SPR band, begins at 0.7 equivalents and is completed at 0.9 eq. of Ag(+)NPs.[50a] (b) SEM image of the large crystals obtained by precipitation, dissolution and slow growth.[50a] (c) AuNPs covered with a mixed layer of ligands and their behavior in solutions of various pH values. Changing the pH one changes the level of protonation of the carboxylic groups and, consequently, the attraction/repulsion nature of the interaction between the NPs. [50b]

Charged NPs are interesting also as building blocks for the fabrication of 3D crystals made of thousands or millions of NPs. Their potential applications include bio-sensing, optoelectronics, and catalysis. Great advances in the field of their synthesis have been made by researchers from the scientific team of Professor Bartosz A. Grzybowski.[50] Using aqueous solutions of gold and silver NPs similar in size, covered with carboxylic (neutral or negative charge, depending on pH) or quaternary amine (positive charge) ligands, they have been able to organize nano-matter into diamond-like structures. The most regular crystals were produced by, first, fast precipitation from mixtures of oppositely charged particles (Figure 14a). Then the precipitate was dissolved and left to the complete evaporation of the solvent. The procedure leads to the formation of regularly faceted crystals with dimensions up to 3 µm (Figure 14b).[50a] Similar results were also observed for NPs covered with mixed negative and positive organic coatings. Researchers were able to change the net charge on the NPs by changing the pH of their

solution, and achieve crystalline precipitates only at the pH at which the net charge on the NPs was zero (Figure 14c).[50b]

1.4 Nanostructures as substrates in surface enhanced Raman spectroscopy (SERS)

Among numerous applications of nanostructures, an important role is played by those based on the optical properties of NPs. In medicine, relevant branches of applications are: bio-imaging in cancer diagnosis (often connected with drug delivery), photothermal therapy, and LSPR-related biomolecule sensing.[51] In this section basic optical features of AuNPs are presented and their application in surface enhanced Raman spectroscopy (SERS) is outlined.

1.4.1 Optical properties of metal nanoparticles

Optical properties of metal NPs are unique because the de Broglie wavelength of the mobile conduction electrons is of the same order as the size of the nanoparticle. Consequently, when light interacts with the metal nanostructure, it excites the whole electron cloud and makes it oscillate in the entire bulk of the particle. For spherical AuNPs of the diameter ~10 nm the typical exciting wavelength is ~500 nm. The electron gas density oscillations between the opposite ends of the nanoparticle, triggered in this way, are called LSPR, and the quanta of these oscillations are called plasmons.

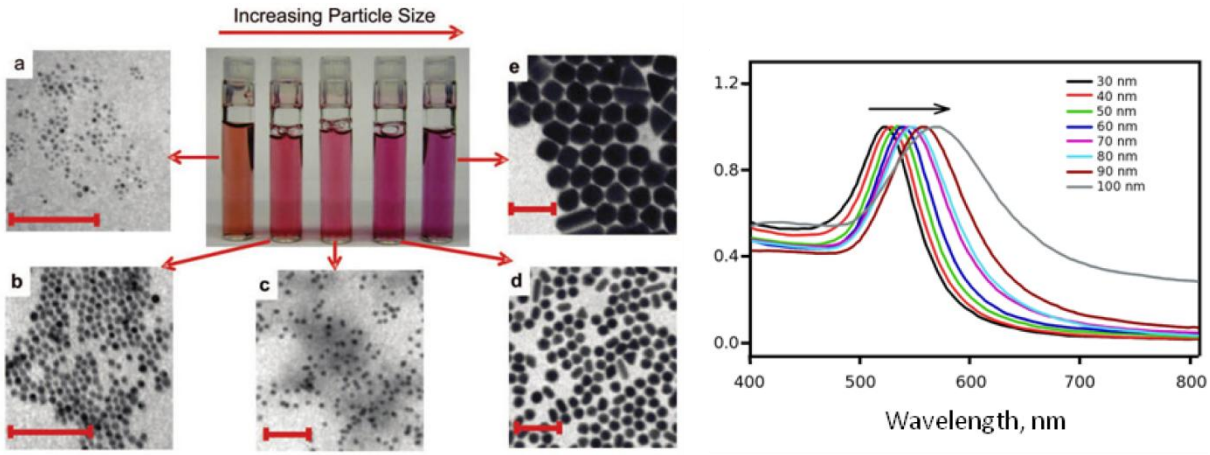

Figure 15 Left panel: Five solutions of AuNPs having 4 – 40 nm in diameter and their TEM images. Scale bar is 100 nm.[51c] Right image: UV-Vis absorption spectra of AuNPs having 30 – 100 nm in diameter.[52]

LSPR is responsible for: (i) the color of the NP solutions and (ii) the characteristic plasmon resonance band. For example, for spherical AuNPs in the 5 – 50-nm-diameter range it is observed near 530 – 550 nm in the absorbance spectrum. As shown in Figure

15, both the color and the absorbance spectrum can be used to determine the size of the AuNPs.

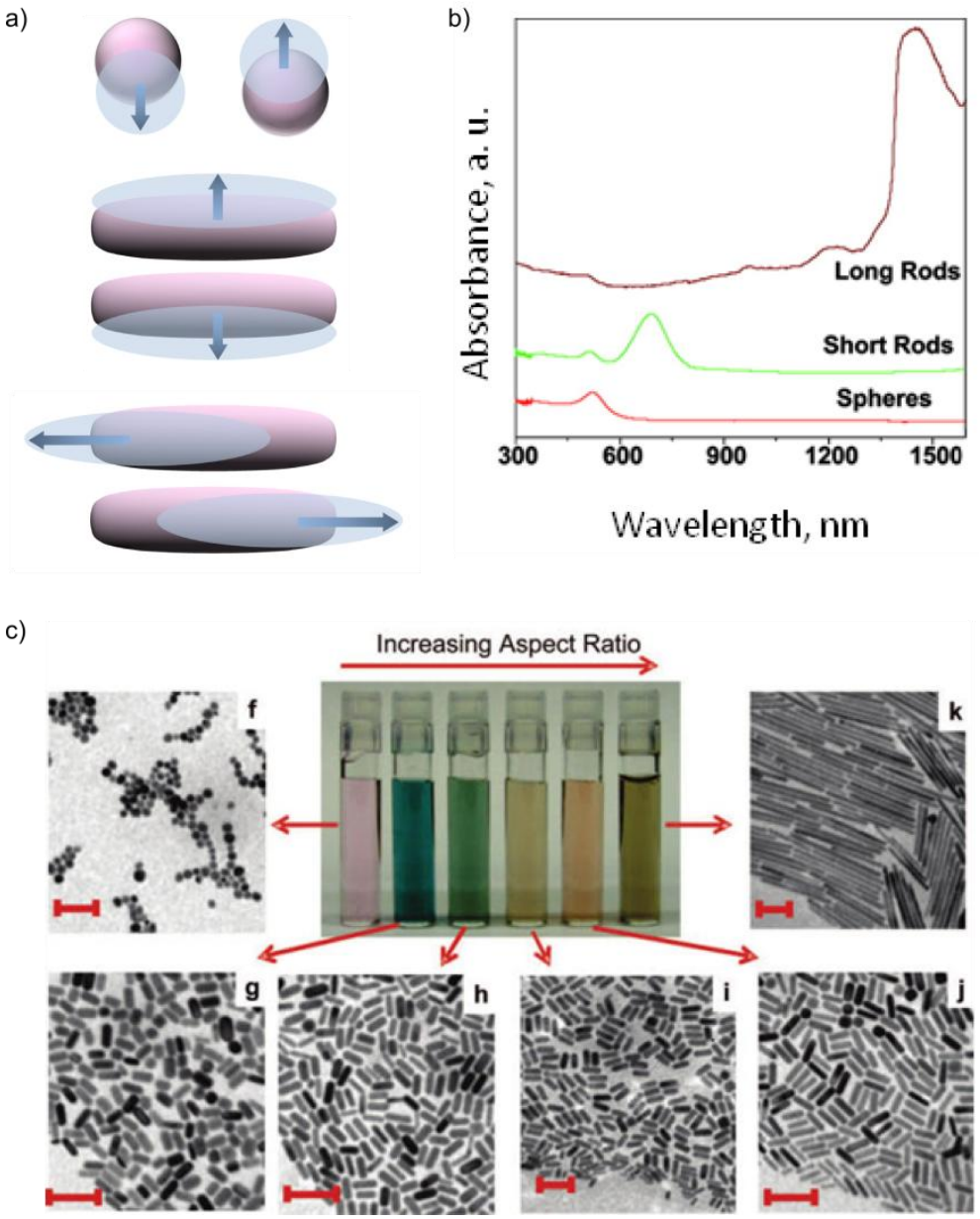

Figure 16 (a) Cartoon presentation of electron gas density oscillations typical for the spherical and elongated AuNPs. Unlike the spheres, gold nanorods display two types of oscillation of the free electron gas density – transverse and longitudinal ones. (b) Absorption spectra of gold nanospheres (diameter 8 nm, red line) and nanorods (aspect ratios 3 and 20, green and purple line respectively).[51c] (c) Six solutions of elongated AuNPs having aspect ratio from 1.3 to 5 for short rods (TEM images f-j) and 20 (TEM k) for long rods.[51c]

The interaction with light is slightly different for NPs of elongated shapes, like nanorods. In this case one observes two absorption bands corresponding to two possible types of oscillation of the free electron gas density, namely perpendicular (the transverse band) or parallel (the longitudinal band) to the major axis of the nanorod (Figure 16a). Similarly to spherical NPs, the absorption band of the gold nanorods is red-

shifted with the increasing size of the particle, expressed by the long to the short axis length ratio, the so called aspect ratio. In the case of elongated particles, differences in the absorption maxima and color of the solutions are much more pronounced than for spherical NPs (Figure 16).

The measurable effects related to the LSPR excitation, like the absorption band at the characteristic plasmon resonance frequency, are very sensitive to changes of the dielectric constant in the closest surroundings of the surface of the NP. Such an exemplary change could be due to the appearance or chemical transformation of some organic molecule near the NP surface. This results in the change of polarity of the surroundings and in the shift of the maximum of the characteristic band in the absorption/reflectance spectrum. This measurable response is commonly used in modern science in several types of sensing, especially in biomedical applications.

1.4.2 Enhancement of local electric field

Considering the electric field around the illuminated AuNP, one should see it as a sum of the incident field and the field produced by the NP. The second component is maximized for a properly chosen wavelength of incident light that is different for various dielectric permitivities of the surrounding media, so the appropriate wavelength is different for particles in water or in air. According to Ref. 8, the field radiated by gold nanospheres, E_{out}, is expressed as

$$E_{\text{out}} = E_0 \frac{3\varepsilon_{\text{m}}}{\varepsilon_{\text{m}} + 2\varepsilon_{diel}}, \qquad (1)$$

where E_0 is the excitation field, and ε_{m} and $\varepsilon_{\text{diel}}$ are dielectric functions of metal and the surrounding medium, respectively. In air, at λ = 530 nm, E_{out} is five times larger than E_0. This enhancement of the local field has become a basis for some spectroscopic methods, including SERS, multiphoton imaging, and two-photon induced luminescence.[8] SERS is a technique based on detection of Raman scattering. Like other spectroscopic methods, it allows for identification of analyte thanks to its specific interaction with light. When an incident electromagnetic wave hits a molecule, it induces transitions between vibrational states in the molecule, typically in the IR frequency, in the range (2 to 12) × 10^{13} Hz. The light could be then scattered in an elastic (the majority of scattered light) or inelastic way. The latter way means that resulting photons have energy different from the energy of incident ones. This phenomenon is called Stokes- and anti-Stokes Raman scattering and occurs approximately for 1 molecule in 10 million. These small

differences between energy before and after interaction with a molecule correspond to the energy required to excite a molecule to a higher vibrational mode, and are unique for every chemical structure. Because this type of scattering involves only a small fraction of molecules, the resulting Raman signal is weak and difficult to detect. This is the reason why enhancement of this signal is crucial in Raman spectra improvement.

In SERS the enhancing effect of localized plasmon resonance is used. The sensitivity of this spectroscopic technique depends on the geometry of the nanosensor (the size, shape, and arrangement of NPs), the surrounding medium, and the type of analyte. In standard analytical procedure the two latter parameters are imposed by the probe to be analyzed, so the only element that can be improved to enhance the signal is the geometry of the nanosensor. It is known that nonspherical particles are, in general, much better enhancers than spheres. The sharp edges of nanostars, nanoflowers, nanorods, or nanopyramids give rise to so-called hot spots. The hot spots produce a very intense electromagnetic field, and, consequently, the magnitude of the scattered signal is enhanced by a factor 10^6 – 10^8.[53] Regardless of shape, the interparticular distance between adjacent NPs also has a strong influence on the sensitivity. Specifically, the nanometer-sized gap is a place of high light concentration, making NP dimmers several times more sensitive than isolated particles (Figure 17).[8,54] Similar enhancement can also be observed for a single AuNP deposited on a gold surface. These types of junctions allow even for detection of single analyte molecules.[55]

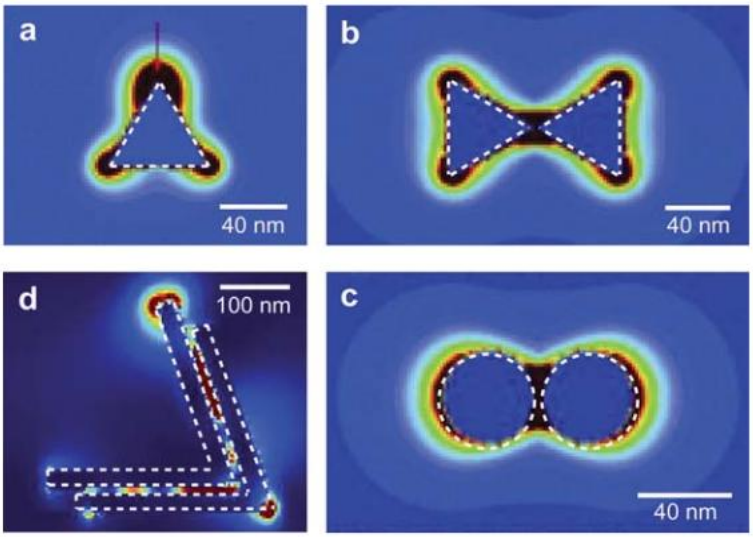

Figure 17 Calculated electric field intensities for different metal NP shapes and dimmers at LSP resonance wavelength. It is visible how much the intensity increases on edges and in gaps between adjacent NPs.[54c]

For the reasons mentioned, high enhancements are observed for closely-packed arrays of sharp-edged NPs. Such arrays can be fabricated by lithography or controlled deposition of NPs from solutions. Solid substrates decorated this way are called SERS-platforms and allow for analysis of molecules chemi- or physisorbed on/near to their surface. Compared to classical Raman scattering measurements, SERS leads to achievement of a signal enhanced thousands, millions, or billions of times, allowing for analysis of more diluted solutions and the use of smaller samples.

1.5 Self-assembled two-dimensional nano-structures

The term "self-assembly" (SA) was introduced in this dissertation in section 1.1. It concerned the spontaneous deposition and ordering of the molecules of thiols on a surface of gold (see Figure 1). The phenomenon of SA is however ubiquitous in nature and is observed at all scales.[56] In nanotechnology SA is an interesting aspect of the formation of the ordered structures consisting of NPs. In my dissertation this phenomenon appears in sections devoted to deposition of the charged AuNPs on a solid substrate (section 4.1) and preparation of a SERS-platform covered with gold microflowers (4.6).

In general, SA is a type of organization of molecules/particles that does not require any external control. Typically, entropic effects, intermolecular interactions (van der Waals or capillary forces), electrostatic and magnetic forces are responsible for the SA. Among the mentioned forces, the ubiquitous van der Waals ones play a crucial role in all types of NPs and, because of their rather attractive nature, are responsible for undesired aggregation and precipitation of the NPs from the solution.[57] The omnipresence of the van der Waals interaction could be thus adverse, but used properly may lead to fabrication of organized nanoparticulate systems in a bottom-up way (Figure 18). In two-dimensional systems the presence of van der Waals interaction is typically demonstrated by the presence of hexagonally packed NP arrays. In the case of polydispersed NPs one can also observe a size-selective sorting. Bigger particles are organized in the inner area of the assembly while smaller (or differently shaped) ones are located at the periphery.[57]

Two types of SA are distinguished: static and dynamic.[56] We talk about "static self-assembly" (SSA) when structures organize autonomously into stable, ordered arrays. The driving force for the SSA is a reduction of energy and the consequent achievement of thermodynamic equilibrium. For this reason structures formed by the SSA are quite stable and do not undergo further transformations. In dynamic SA (also called dissipative SA or DySA), in turn, the organized structures are far from the thermodynamic equilibrium, so their formation requires a constant supply of energy. Energy is subsequently dissipated *via* production of entropy.[58,59,60] In practice, all processes of self-assembly that lead to the formation of stable and applicable nanoparticulate structures belong to the class of the static SA.

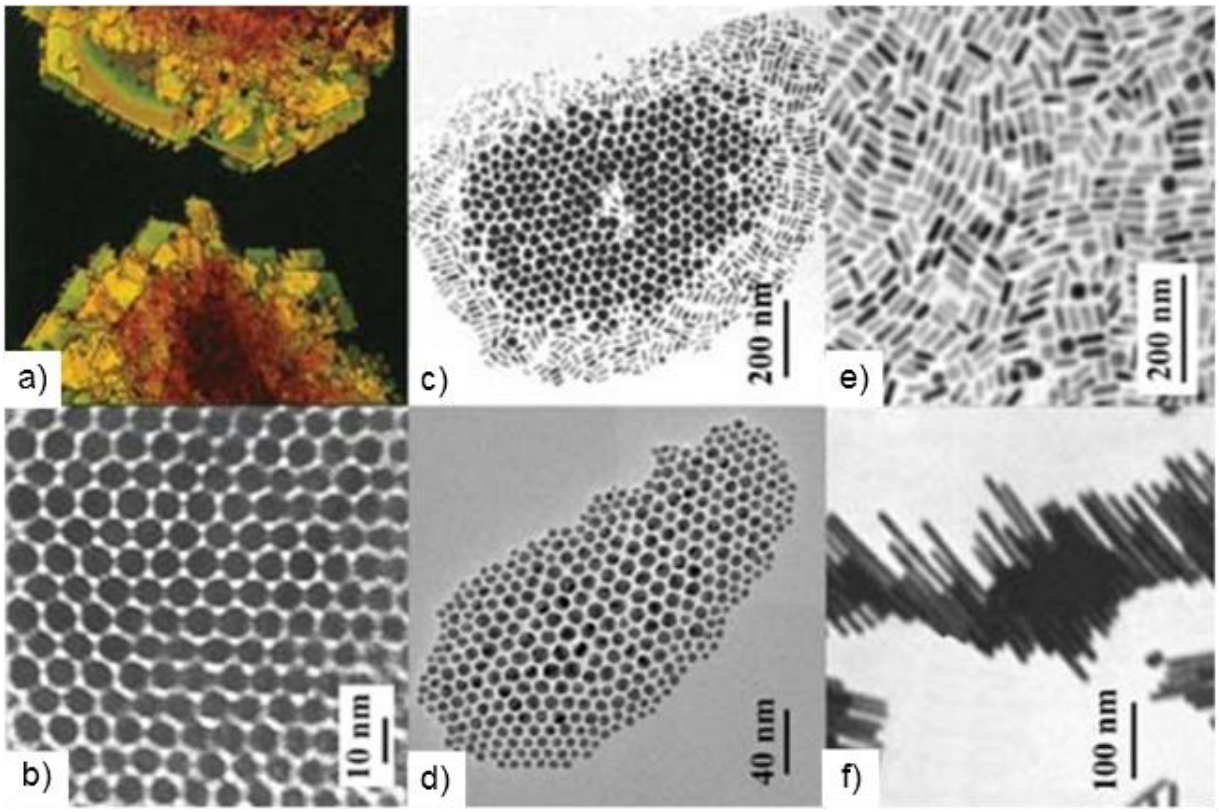

Figure 18 Various assemblies driven by van der Waals interactions. Not only close-packing, but also shape-segregation, size-segregation of nanospheres, and side-by-side organization of nanorods are visible.[57]

Static SA is a spontaneous process, but typically it requires a rational design of the building elements to obtain properly organized microscopic structures for technological applications. This design could be achieved by proper choice of the size and shape of the NPs which are supposed to become efficient building blocks. It can be also provided by the functionalization of the "bricks". The ligands play a key role in the SSA assembly process. Their type determines the steric, physical, and chemical

interactions between NPs. It also influences the way NPs interact with their environment. For example, by choosing proper ligands one makes the NPs susceptible to an external directing field (*e.g.* electric). The third type of design of the SSA process is modification of an environment by application of some templates. The presence of these steric factors can lead to selective assembly of particles. Typical templates are small particles, acting like spacers between the NPs, as well as periodical scaffoldings in which assembling structures are immersed. Also, changes in temperature, pH, or the polarity of the environment can affect the interparticle interactions and trigger the SSA of the NPs.[61]

Because the NPs have to be free to move to assemble, the SA usually occurs in a solution or on solid/liquid, liquid/liquid or liquid/gas interfaces. Assemblies in bulk solution lead rather to 3D products, but interfaces are convenient templates for two-dimensional (2D) ordering. A well-known example of this type of ordering are Pickering emulsions.[62] The immobilization of the particles at the liquid/liquid interface, driven by the reduction in interfacial energy, is the first stage of such an ordering. The next is orientation of the single particle in relation to the plane of the interface: non-spherical NPs are usually forced to lay flat. The third phenomenon related to assembly on the interfaces is energetically-promoted size segregation of the NPs. This is a consequence of the fact that, for particles as small as NPs, the thermal energy responsible for special fluctuations is comparable to the interfacial energy.[63] In the case of limited interface area and the presence of particles of various sizes in the bulk solution, the trapping of particles with a bigger radius is thermodynamically promoted, while smaller ones are pushed into the bulk. This results in higher reduction of the Helmholtz free energy than would be observed for smaller particles migrating from the bulk to the interface. The described relation concerns not only the NPs deposited on the water/oil, but also on a liquid/gas interface.

By using solid/liquid interfaces one is able to achieve more types of assemblies than for purely fluid interfaces. Utilization of chemical or physical sorption onto a solid surface offers the opportunity to form mono- and multilayers that are more stable than those assembled on a fluid interface. In the case of nano- and micro-particles, SA layers (including columnar arrays) are prepared *e.g.* by capillary and convective forces during evaporative drying,[64] thanks to electric or magnetic fields, a combination of fields (like

electric and magnetic fields, electric field and flow,[65] magnetic field and flow[66]) or even, for larger particles, by gravity[67].[61]

The self-assembled layers of the NPs have attracted considerable scientific attention because of their great application potential. For example, 2D structures consisting of metallic (Ag, Au)[68,69] or semiconductor (CdSe, CdS)[70,71] NPs can be used as solar cells,[72,73] in sensing,[74] light emitting devices,[69,71] storage media,[71,75] photodetectors,[71] semiconductor nanorods epitaxial growth,[76] electrode modification,[77] corrosion protection,[78] antireflective films,[79] nanosphere lithography,[80] or heterogeneous catalysis.[81]

2 Motivation

From the literature on nanotechnology emerges a fascinating picture of the nano-world. The hundreds of types of NPs of different shapes, sizes, and chemical composition have aroused interest because of their huge application potential. They are also interesting from a purely scientific point of view because their physical and chemical properties are different from the features of their macro analogues, and difficult to predict. It is not surprising therefore that nanotechnology is a very rapidly evolving field of knowledge. Our understanding of the mechanisms governing the world of nanostructures is becoming greater every year, and new methods for NPs synthesis and organization into desired structures are appearing. In fact, however, there is still so much to discover and improve: the fabrication of nanostructures could be more precise, efficient, and environmentally friendly; the explanations of many mechanisms free of doubt and unconfirmed hypotheses; the scale of application – wider. For these reasons, I decided to choose nanotechnology as the subject of my research.

My goal was to contribute to the development of nanotechnology, especially in the aspect of its applicability. In this dissertation I present both a purely scientific analysis of the formation and properties of nano- and microstructures, as well as useful methods for their synthesis, manipulation, and utilization. I believe that my results will find application, especially in medical diagnosis and treatment.

Experimental section

3 Experimental section

In this chapter I describe the materials and experimental procedures employed in the research presented in this dissertation. Specific information on the experimental methods related to individual parts of the research are placed in the "Preparation and analysis of samples" sub-sections of each section of chapter 4 ("Results").

3.1 Analytical techniques used

3.1.1 Scanning electron microscopy (SEM) and energy-dispersive X-ray spectroscopy (EDX)

SEM is one method used for studying different aspects of the morphology of NPs. It produces high resolution images by recording signals coming from interactions of the sample and an electron beam. Electrons originating from an electron gun are accelerated to reach the desired kinetic energy. They travel through a set of lenses (magnetic or electrostatic) that, cutting some electrons off, assemble and focus the beam. Schematic presentation of the microscope is shown in the Figure 19.

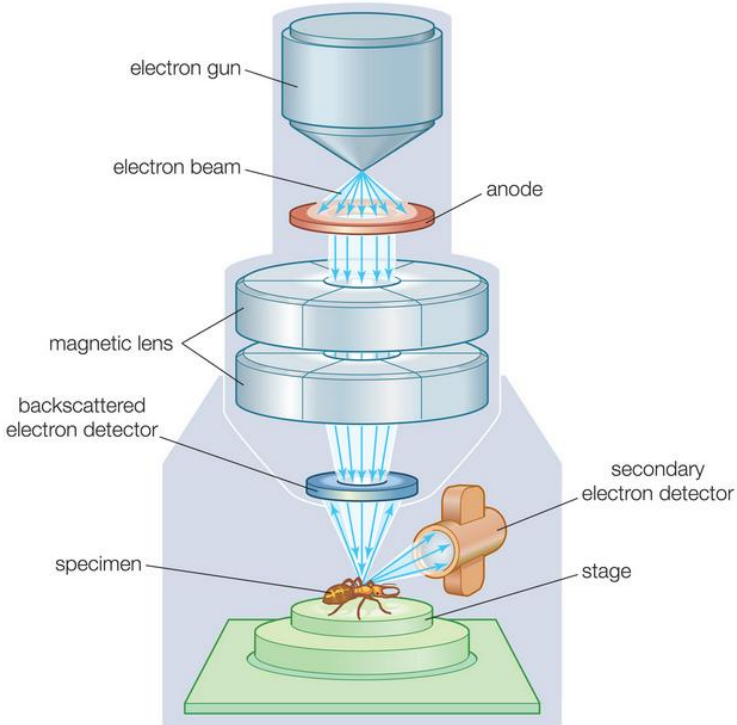

Figure 19 Schematic of SEM. Source of the image: Ref. V on page 150.

The results of energetic bombardment of the probe are different types of signals, which provide various sets of structural information about the sample. The collected

signals can be, depending on the detector employed, secondary electrons (SE), back-scattered electrons (BSE), characteristic X-Rays, cathodoluminescence (CL), specimen current and transmitted electrons. Secondary electron imaging (SEI) provides with type SE1 secondary elements which carry high-resolution and surface-sensitive details about the sample, or with type SE2 carry lower-resolution information. Singly scattered backscattered electrons (BSE1) are connected with compositional contrast, while multiple scattered backscattered electrons (BSE2) are used to determine the composition and crystalline structures of a sample. Analysis of characteristic X-Ray lines can be used for mapping the distribution of elements in a sample. The CL detectors analyze emitted light leading to discovery of certain trace impurities in minerals. To obtain a sharp image using SEM, the analyzed objects must be conductive. They can be imaged in a wide range of magnifications, over a range of about 6 orders of magnitude.

Apart from SEM imaging, in the presented studies EDX was also used. In this method a high-energy beam of electrons ejects an electron from the inner shell of the analyzed atom. In this way a hole is created. An electron from a higher-energy shell fills the hole and releases the energy difference in the form of a characteristic X-ray wave. Detection and analysis of these X-rays enables elemental analysis of the sample.

In this work, nanostructures deposited on silicon substrates were analyzed by field emission scanning electron microscopy (FE-SEM) using a Neon 40 - Auriga Carl Zeiss instrument in the InLens detection mode, applying 5 kV beam voltage, unless indicated otherwise. Elemental analysis of the silver-gold MFs was done by energy-dispersive X-ray spectroscopy using EDX-system QUANTAX 400 Bruker attached to the SEM. Milling of the AuMFs was done by ablation using FIB attached to the Cross-Beam. A Zeiss Auriga FIB/SEM system equipped with a Cobra-focused gallium ion beam column, a Schottky field emission gun and a Gemini electron column, was employed. For FIB milling, a 30 keV Ga ion beam with a 20 pA current was employed.

3.1.2 Surface enhanced Raman spectroscopy experiments

Theoretical background of this analytical method is presented in section 1.4. In this dissertation, in order to estimate a Raman scattering enhancement of AuMFs, regular Raman and SERS measurement were conducted. Typically, the acquisition time was 20 min for regular Raman, and 30 – 60 s for SERS experiments.

For the model analyte, *p*-mercaptobenzoic acid (*p*-MBA), SERS spectra were obtained by excitation with a 785 nm laser. This model molecule was used for

estimation of enhancement factors (EFs) of the new SERS platforms presented in the section 4.6. The EF is a parameter comparing the signal intensity on the SERS platform to the signal of the same analyte in a regular Raman measurement and was calculated according to the formula:

$$EF = I_{SERS}N_{NR}/(I_{NR}N_{SERS}), \quad (2)$$

where N_{SERS} refers to the number of molecules adsorbed on the SERS probe within the laser spot area and N_{NR} refers to the number of molecules probed by Raman spectroscopy. I_{SERS} and I_{NR} correspond to the SERS intensity of the analyte on the modified surface and to the normal Raman scattering intensity of the same analyte in bulk. Both intensities were measured at 1077 1/cm.

In the experiments presented in the "Bottom-up preparation of a stable and efficient SERS platform" (in sub-section 4.6.4.5) the SERS samples were prepared by soaking of the SERS platform in a solution of the analyte (1.0×10^{-6} M, 9.0 mL). The beam of laser was 5 μm in diameter. The normal Raman spectrum was collected for a cell filled with a pure *p*-MBA liquid (154.19 g/mol) of density 1.06 g/cm^3. The effective illuminated volume for the setup was 1.96×10^3 μm^3. The excitation light was passed through a line filter, and focused on a sample mounted on an X-Y-Z translation stage with a 20× microscope objective. The acquisition of the Raman signal was conducted by the same objective through a holographic notch filter blocking the Rayleigh scattering. An 1800-groove/mm grating was used to provide spectral resolution of 5 1/cm. The Raman scattering signal was detected by the 1024 × 256-pixel RenCam CCD detector.

The reproducibility of spectra, presented in the same section, was determined with a Savitzky-Golay second derivative method, using a window size of 50 data points with second order polynomial. Correlation coefficients between all nonidentical spectral pairs ($i \neq j$) in the same data set were found using the formula:

$$P_{i,j} = \frac{\sum_{k=1}^{W}\left(I_i(k) - \overline{I_i}\right)\left(I_j(k) - \overline{I_j}\right)}{\sigma_i \sigma_j} \quad (3)$$

where *i* and *j* are indexes of the spectra in the data matrix, *k* is the wave number index of the individual spectra, *I* – the spectral intensity, *W* – the spectral range, and σ_i – the standard deviation of the spectrum. To evaluate the reproducibility of multiple

measurements, the average of the off-diagonal correlation coefficients, Γ, was determined as follows:

$$\Gamma = \frac{2\sum_{i=1}^{N}\sum_{j=i+1}^{N} P_{ij}}{N(N-1)} \quad (4)$$

Parameter Γ varies in the 0 – 1 range, where 1 – identical spectra and 0 – completely uncorrelated spectra.

3.1.3 Zeta-potential measurements

Zeta-potential (ζ-potential), is the name for electric potential in a conventional interface between a double layer and the bulk medium (the so-called slipping plane), in which a charged particle is suspended. As is shown in Figure 20, the sample negatively charge particle is covered by two layers of ions. The closer one, the so called Stern layer, is made of positive ions, strongly attracted to the surface of the particle by electrostatic forces. The outer layer of ions, the diffusive layer, also contains positive ions attracted by the particle, as well as negative ions attracted by the Stern layer. Outside of the diffusive layer the electrostatic influence of the negatively charged colloid decreases rapidly with increasing distance from the surface of the particle.

Application of an electric field in the dispersion makes particles with Zeta-potential move toward an electrode of opposite charge. The velocity of movement is proportional to the magnitude of the ζ-potential. Owing to electrokinetic phenomena, Zeta-potential is measured indirectly. In colloidal dispersions ζ-potential can be used as an indicator of possible coagulation in the colloidal system, being therefore an indicator of stability. The higher the value of Zeta potential, the greater the stability. In this study, the Zeta-potential of the charged AuNPs was measured using a Malvern Zetasizer NanoZS (Malvern Instruments, U.K.) analyzer, at 25˚C.

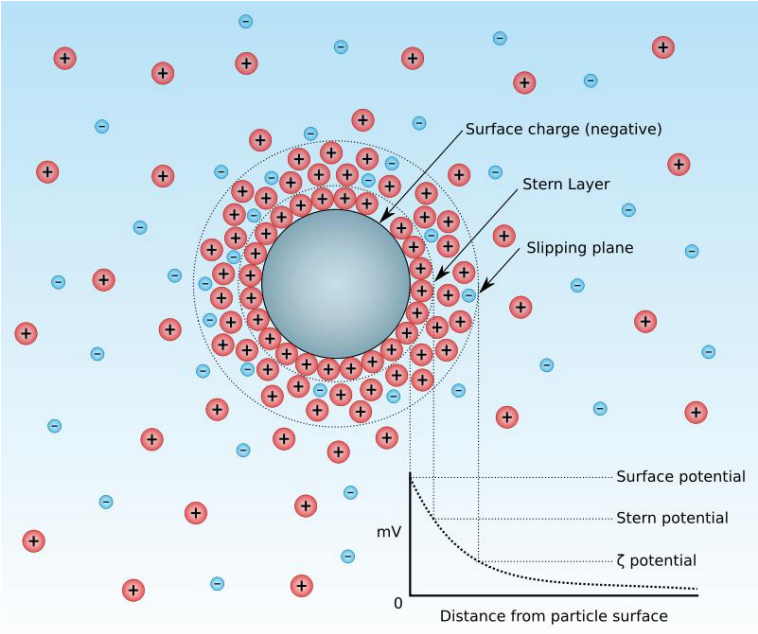

Figure 20 Negatively charged particle in a colloidal dispersion. Diagram shows the concentration of ions and potential as a function of distance from the charged surface. Source of the image: Ref. VI on page 150.

3.1.4 UV-Vis spectroscopy

When incident light passes through the probe, part of its intensity is absorbed by molecules of analyte. The wavelength of the absorbed electromagnetic wave depends on the electronic structure of analyte, while the level of absorption is linearly proportional to its concentration. According to the Lambert-Beer law

$$Absorbance = log_{10}\frac{I_0}{I} = \varepsilon_{\text{abs}} cl, \tag{5}$$

where I_0 denotes intensity of incident light, I – intensity of transmitted light, c – molar concentration of sample, l – length of the absorption path, and ε_{abs} – molar absorption coefficient.

In this study, absorption spectra in the ultraviolet-visible (UV-Vis) range were recorded in several research subjects, and made using diverse equipment. Specific apparatus type and conditions of the measurement are described in the "Preparation and analysis of samples" sub-sections of each section in chapter 4.

3.1.5 Small-angle X-ray scattering (SAXS)

SAXS is a technique used to determine the size, shape, and arrangement of nanoparticles in disordered or partially ordered systems. It is an analogue for powder diffraction and can be used both for liquid and solid probes. In SAXS a monochromatic X-ray beam is directed at a sample. Some of the waves are scattered. The elastically

scattered ones, detected at angles smaller than 10 degrees, form a scattering pattern characteristic for the properties of the sample.

In this dissertation, SAXS measurements were used to determine the size of the AuNPs. The SAXS patterns were obtained with the Bruker Nanostar system; the patterns were registered with a Vantec 2000 area detector. The CuK (α = 1.54 Å) radiation was used. The samples were prepared in Lindemann capillaries (1.5 mm in diameter). The signal intensities were obtained through integration of the 2D patterns over an azimuthal angle. Measurements were carried out at a temperature of 25°C.

3.1.6 X-ray diffraction (XRD)

X-ray crystallography is an analytical method including diffraction of an electromagnetic wave (the X-ray) on the crystal structure of an analyte. The incident X-ray encounters the regular array of scatterers – electron clouds of the atoms building the crystal – and each of these strikes produces a secondary spherical wave. The repeating arrangement of the scatterers leads to production of many spherical waves that at some points in space cancel or add to each other. The set of such waves land on a detector (*e.g.* a piece of film) making a diffraction pattern. By analyzing the intensity and positions of the diffracted beams, one can deduce the spatial arrangement of the density of electrons within the analyzed crystal. This information allows *i.a.* for determining the mean positions of the atoms in the crystal.

In this dissertation, XRD was used to determine the crystal structure of the AuNPs. XRD spectra were recorded using Bruker D8 Discover equipped with Vantec linear detector and at CuKα radiation in reflection geometry. All measurements were carried out at room temperature.

3.2 Materials

Sulfuric acid, hydrogen peroxide, hydrochloride, sodium chloride, potassium thiocyanate, sodium carbonate, sodium acetate, sodium nitrate, potassium sodium tartrate and nitric acid were purchased from Chempur. *N*,*N*,*N*-trimethyl(11-mercaptoundecyl)ammonium chloride ($HS(CH_2)_{11}N(CH_3)_3^+Cl^-$, TMA), was synthesized according to a known procedure.[82] Acetone and methanol from Chempur, and deionized water (15 MΩ) were used as solvents. For SERS measurements, DNA-oligomer (from Genomed) and virus λ (courtesy of University of Gdańsk) were applied. All other reactants were purchased from Sigma-Aldrich. The reagents were all analytical grade

and used without further purification. GaN substrates were purchased from TopGaN. The silicon wafers (orientation 100) were purchased from Cemat Silicon. The glass microscope slides were obtained from Roth. Before use, the wafers and glass slides were cut manually into strips and cleaned by sonication in water and then in acetone. Next, the plates were immersed in a freshly prepared piranha solution (3:1 H_2SO_4:30% H_2O_2) for 3 h. Finally, the plates were rinsed with deionized water and then with methanol, and dried in air.

3.3 Methods

3.3.1 Synthesis and functionalization of gold nanoparticles

Gold nanoparticles were synthesized according to known procedure.[83] First, a solution of didodecyldimethylammonium bromide (DDAB, 1.295 g, 2.8 mM) in toluene (28 mL) was prepared. Then, $HAuCl_4 \cdot 3H_2O$ (19.4 mg, 0.05 mM) was dissolved in 5 mL of DDAB solution by sonication. To the prepared mixture, dodecylamine (DDA, 180 mg, 0.97 mM) was added and dissolved by sonication. Next, tetrabutylammonium borohydride (TBAB, 50 mg, 0.2 mM) dissolved in 2 mL of the DDAB solution was injected do the reaction mixture during stirring. In this step small AuNPs ("seeds") were formed and the reaction mixture became brown. Seeds were then grown by, firstly, addition of the reaction mixture to 50 mL of solution of $HAuCl_4 \cdot 3H_2O$ (194.6 mg, 0.5 mM), DDAB (1 g, 2.16 mM) and DDA (1.85 g, 9.98 mM) in toluene (50 mL) and finally, by slow dropwise addition of anhydrous hydrazine (128 mg, 4 mM) in 20 mL of DDAB solution. The obtained solution of AuNPs became wine red and was stable for at least a few days. The procedure for AuNP synthesis and subsequent functionalization is presented in a simplified way in Figure 21.

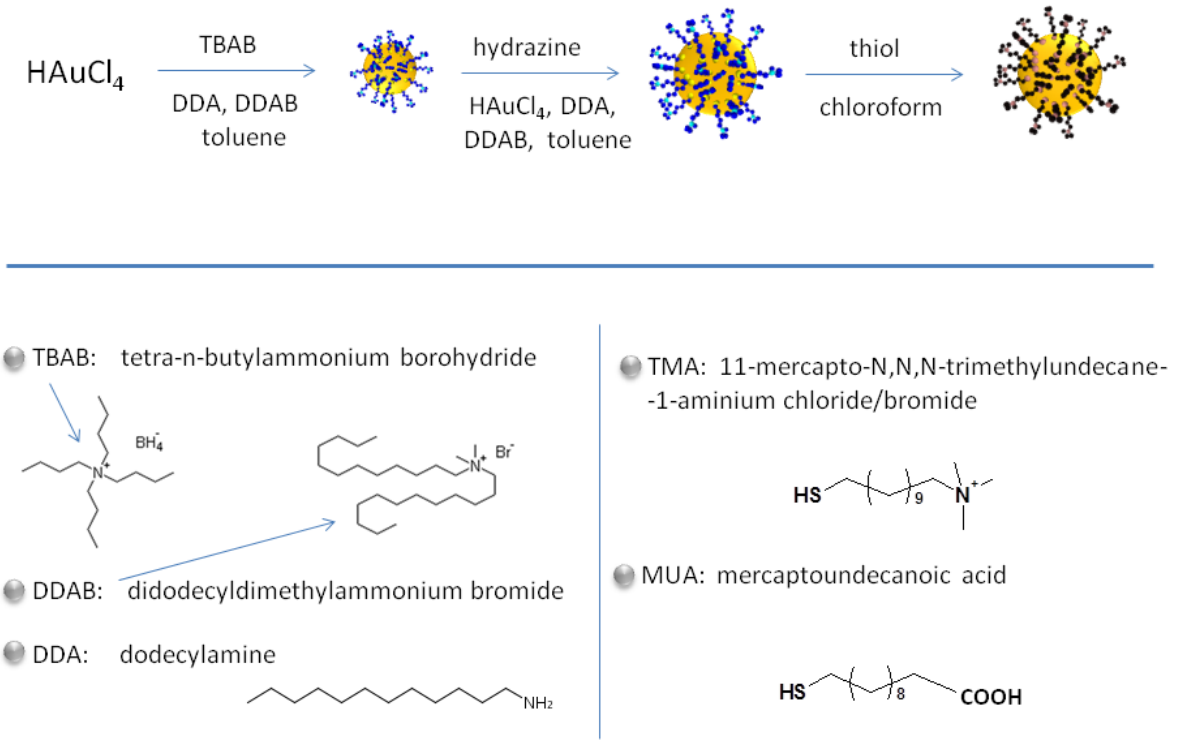

Figure 21 Upper panel: The procedure of the synthesis and functionalization of the AuNPs: In the first step small particles are formed that then grow in a solution containing a new portion of gold salt. In the bottom panel chemical structures of the reagents used are shown.

To provide a **positive charge** on the NPs, the hydrophobic amine ligands were replaced with the *ω*-functionalized alkanethiol, *N,N,N*-trimethyl(11-mercaptoundecyl)ammonium chloride ($HS(CH_2)_{11}N(CH_3)_3$ $^+Cl^-$, TMA). To carry out the ligand exchange reaction, I applied the following procedure: From the toluene solution (10 g, 7.05 mM, 0.075 mmol Au) the Au@DDA NPs were precipitated with methanol (70 mL), then dissolved in chloroform (15 mL) and added dropwise to the solution of TMA (30 mg, 0.11 mmol) in methanol (5 mL). The mixture was stirred overnight. After this time, and after the addition of isopropanol (2 mL), the AuNPs were precipitated with hexane and centrifuged (30 min, 7000 rpm). Supernatant was decanted and the black precipitate of AuNPs was dissolved in methanol (1.5 mL) and isopropanol (1.5 mL), precipitated with hexane (~40 mL), and centrifuged (15 min, 6000 rpm). The dissolution and precipitation process was repeated five times. Eventually, the purified and dried AuNPs were dissolved in 35 mL of deionized water yielding a 0.73 mg/mL gold solution. The average radius of the metal core of the Au@TMA NPs, determined from the SAXS spectrum of the AuNP solution, was 2.5 nm with the polydispersity 0.43 nm. The thickness of the TMA protecting monolayer on the AuNPs, calculated using ChemSketch software, was about 1.8 nm.

The **negatively charged** AuNPs were prepared in a manner analogous to that employed to obtain the positively charged ones. The same procedure was used, but mercaptoundecanoic acid (MUA) instead of TMA was applied. In the final step the Au@MUA NPs were dissolved in methanol.

3.3.2 Deposition of AuNPs on solid substrates

Preparation of the solid substrates

In my experiments, glass and silicon as substrates were employed. The glass slides and silicon wafers were cut manually into stripes with a size of 11 mm x 50 mm, which allowed me to place glass plates vertically in a spectrophotometer cell. The plates were washed with deionized water and then with acetone. Next, the stripes were treated with a piranha solution (95% H_2SO_4:30% H_2O_2, 3:1 v/v). Then the stripes were washed with deionized water and with methanol, and finally dried in air. Both glass and silicon substrates exposed to aqueous solutions of NPs and salt at pH ~9.5 developed a negative surface charge.

Covering substrates with nanoparticles using ionic- strength-controlled method

In general, the method for covering solid substrates with AuNPs consists in immersing of the substrate in the water solution of AuNPs and inorganic salt (usually sodium chloride, NaCl). The mixtures of AuNPs and salt with appropriate component concentrations were prepared from the stock solution of AuNPs, and concentrated aqueous solutions of salts, whereas the solution of AuNPs was always added last. Irrespective of the salt content, four AuNP concentrations were used. The highest concentration of gold was 0.15 mg/mL (corresponding to about 3.7×10^{-7} M NP concentration). In my dissertation, I refer to this solution as C_{100}. I applied also three smaller AuNP concentrations: 0.75, 0.50, and 0.25 × C_{100}, which are denoted as C_{075}, C_{050}, and C_{025}, respectively. I carried out experiments for the NaCl concentrations in the range from 1.0 mM to 4.6 M. (With my procedure, I could prepare mixtures containing NaCl in concentrations no higher than 4.6 M, which was achieved by adding the AuNP solution to the saturated 6.15 M solution of NaCl.) All the mixtures used were alkaline because of the residue of amines that were used during the synthesis of the AuNPs. For example, the pH of the C_{100} AuNP solutions containing 2.0 M NaCl was around 9.5.

A slide of material to be coated was immersed in a vertical position for a prescribed period of time in ~100 mL of a mixture of AuNPs and salt. The slide was then removed from the solution and rinsed with deionized water to wash out the salt and

residual AuNPs that were not adsorbed on the surface. Finally, the slide was dipped in methanol for about 10 s and dried by placing it in a vertical position on a filter paper so that the slide contacted the paper with the bottom edge only. The analysis of the surfaces of silicon coated with AuNPs, performed using the scanning electron microscopy (SEM), revealed that, for all salts used, the AuNPs always formed a single layer on the substrate. All experiments were performed at room temperature (about 25°C).

In some experiments I describe samples as **"low-density"** and **"high-density" coatings**. To deposit the AuNPs precisely this way, a silicon plate was immersed for 10 min. in 4 mL of aqueous solution of AuNPs (0.18 mg/mL) and sodium chloride (1 mM and 2 M for the low- and high-density coating, respectively). The slide was then removed from the solution and rinsed with deionized water to wash out the salt and residual AuNPs that were not adsorbed on the surface. Finally, the slide was dipped in methanol for about 10 s, and dried by placing it in a vertical position on a filter paper.

Results

4 Results

In this chapter I present a structured description of my research regarding gold nano- and microparticles. The presented study concern the synthesis and further modifications of the small gold objects and, above all, behavior, properties and applications of two-dimensional arrangements made of them.

The chapter "Results" is divided into six sections. The first one (4.1) is devoted to the smallest objects I investigated, namely AuNPs having about 5 nm in diameter. A new method for their immobilization on solid substrates – an adsorption onto negatively charged substrates occurring in solutions containing positively charged NPs and salt – is presented.

In the sections 4.2 and 4.3 morphological changes that the AuNPs undergo in two-dimensional deposit are analyzed. Section 4.2 presents detailed research on deformations of the AuNPs due to their deposition on solid substrate. This section is based on the article published in the *Journal of Physical Chemistry C*.[84] In the section 4.3 influence of the oxygen plasma on the AuNP deposit is studied. Results presented in the section 4.3 have been published in *RSC Advances*.[85]

Section 4.4 refers to the process of growing of small AuNPs deposited on the silicon plate. Hydroxylamine hydrochloride, ascorbic acid, and 2-mercaptosuccinid acid are investigated as reducing agents leading to the formation of more dense gold coverages, composed of the enlarged AuNPs of different shapes.

Section 4.5 is focused on the synthesis and morphological modifications of the big branched particles called microflowers (AuMFs). Results presented in this section have been partially published in *Plasmonics*.[86]

In the section 4.6 methods for fabrication of various gold coatings made of the AuMFs and their application in SERS are described. Both different metallic films as well as various solid substrates are examined. A part of the results shown in this section has been published in *Plasmonics* and *Chemistry of Materials*.[87]

4.1 Deposition of AuNPs using ionic strength-controlled method

4.1.1 Introduction

At present, two-dimensional coating consisting of metallic or semiconductor NPs can be prepared by several well-established methods, including: the Langmuir-Blodgett technique,[74] electrodeposition,[88] spin-casting,[69] drop-casting,[68] dip-casting,[76] grafting,[89] contact printing,[90] or the sol-gel technique.[91] All these methods have some drawbacks. They require special equipment, are confined to a limited set of surfaces, or they can be employed on flat or small-sized areas only. Moreover, there is a need to search for new coating methods that would allow one to cover quickly and cheaply large areas of substrates with charged NP monolayers. There is experimental evidence[92] that — due to lateral electrostatic repulsion — it is impossible to obtain dense coatings in the solutions of like-charged AuNPs in low ionic strengths. The addition of salt can reduce the electrostatic forces but, for concentrations of the order of 10^{-1} M, renders the system unstable against AuNP aggregation. So far, the effect of salt concentration on the adsorption of charged AuNPs has been studied[93] for relatively small ionic strengths (up to 15 mM). Higher salt concentrations have been investigated[94] in the context of the layer-by-layer deposition protocol, in mixtures containing one type of charged NPs and polyelectrolytes.

In this section, the effect of ionic strength on adsorption of positively charged NPs onto negatively charged substrates is investigated. The deposition process is studied in a wide range of salt concentrations, spanning from 0 to 4.6 M. It is found that, surprisingly, the salt has a stabilizing effect on the plating solution. For high ionic strengths, above ~2 M, the AuNP aggregation process is suppressed and the AuNPs adsorb on the substrate to form dense layers with surface coverage reaching about 50%. This finding provides a facile method to coat surfaces of materials with AuNPs. Using this method, substrates that develop a negative charge on their surfaces, such as glass or silica, can be coated by immersion in an aqueous solution of charged AuNPs and simple inorganic salt. The deposition process is fast, and the substrates to be covered do not require any special treatment. The AuNP monolayers obtained with the method are stable in air and in common organic solvents. The density of the coating depends on and can be easily controlled over a wide range by AuNP and/or salt concentration and by the immersion time. Low-density coatings composed of single AuNPs separated from each other, which

are difficult to achieve by other means, can be easily obtained with the method presented. Such low-density monolayers can be potentially applied in fields of research where chemical or physical processes on a single AuNP are investigated; for example, in spectroscopy[95] or semiconductor nanorod epitaxial growth.[76]

4.1.2 Preparation and characterization of samples

Preparation of the nanoparticles

AuNPs were synthesized according to known procedure.[83] The radii of the AuNPs, determined using SAXS measurements, were R = 2.02 ± 0.48 nm. To generate a positive charge, the NPs were coated with TMA, as was previously described (see the Experimental section, "Methods – synthesis and functionalization of gold nanoparticles").[50a] The thickness of the TMA protecting monolayer[50a] on the AuNPs was 1.8 nm. The functionalized NPs were dissolved in deionized water (15 MΩ Millipore) yielding a 0.6 mg/mL gold solution (the stock solution). Preparation of solid substrates and deposition of NPs on them is described in the Experimental section. To demonstrate the versatility of the salting-out deposition method, I employed also a C_{100} AuNP solution containing the following salts: KSCN (potassium thiocyanate), Na_2CO_3 (sodium carbonate), $NaC_2H_3O_2$ (sodium acetate), $NaNO_3$ (sodium nitrate), and $KNaC_4H_4O_6$ (sodium-potassium tartrate) in a concentration of 2.0 M.

Instrumentation

UV-Vis absorption spectra were recorded on a Shimadzu MultiSpec-1501 instrument in the 300-700 nm range. The baseline was measured for clean glass slides. During the absorbance measurements, the glass slides were fixed in the spectrophotometer cell perpendicularly to the light beam.

Determination of the Adsorption Kinetics

To monitor the kinetics of the AuNP adsorption, I measured the absorbance, φ, of the surface of the glass slides covered with NPs as a function of the immersion time, t. To obtain the dependence $\varphi_i(t_i)$ for n different immersion (dipping) times, $t_1 < ... < t_n$, I carried out n independent experiments. In each experiment, the glass slide was dipped for the time t_i in the solution of the AuNPs and NaCl. The absorbance of the slides was measured, based on the UV-Vis spectroscopy. Each value of the absorbance, φ_i, corresponding to a given immersion time, t_i, was taken as an average of three experiments carried out for three different slides.

I found that the shape of the absorption spectrum of the AuNPs adsorbed on the glass surface was similar to that exhibited by the AuNPs in the bulk solution. For very low AuNP coverages, the position of the absorbance peak was located at λ_{max} = 534 nm and was red shifted as compared with the AuNP solution, λ_{max} = 518 nm. This shift of the peak position can be attributed[96] to the increase of the average dielectric constant of the medium surrounding the AuNPs deposited on the glass substrate. The red shift increased with increasing surface density of the adsorbed AuNPs. For the highest AuNP coverages (obtained for the C_{100} solution and 2 M NaCl concentration), the peak was observed at λ_{max}~550 nm. Examples of five UV-Vis absorbance spectra recorded for a glass slide dipped in the C_{075} solution (2 M NaCl) for five different times are shown in Figure 22.

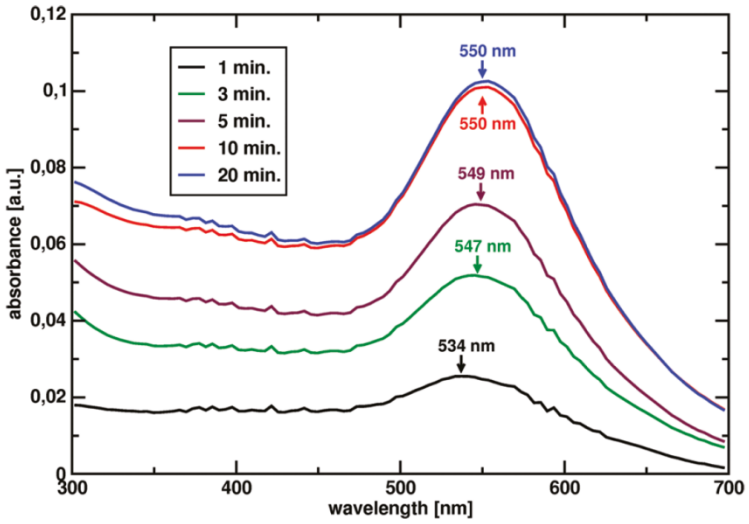

Figure 22 UV-Vis absorption spectra of a glass slide covered with the AuNPs. Results for five immersion times, 1, 3, 5, 10, and 20 min, are presented. The solution contained AuNPs in a concentration of C_{075} and 2.0 M NaCl. The position of the absorption maximum red shifts as the coverage of the glass surface increases.

The coverage-dependent red shift originates from the dipole-dipole interactions[97,98,99,100] between the metal cores of the neighboring NPs. The strength of the plasmonic coupling decreases rapidly when the distance between the cores increases. Thus, the red shift $\Delta\lambda_{max}$ = 16 nm observed indicates that patches of closely packed AuNPs are formed for the highest surface densities. Note here that the strength of the plasmon coupling depends on the ratio $D/2R$, where D is the center-to-center distance between the metal cores and R is the radius of the metal core. A strong red shift of the absorbance peak is observed[96,100] for values of $D/2R$ below, approximately, 1.5. The radius of the core of the AuNPs used was R = 2.02 nm, the outer radius of the NPs, being a sum of R and the thickness of the TMA layer, was 3.92 nm. It follows that, for two

AuNPs in contact, $D/2R \approx 2$. For this reason, in our experiments, we observed a relatively small red shift of λ_{max}, even for the highest AuNP coverages. Importantly, note that the method based on the UV-Vis spectroscopy allowed me to determine the actual adsorption rate. That is, because the residual (unadsorbed) AuNPs were washed out prior to the measurements, the absorbance φ was due only to the AuNPs bound to the surface.

4.1.3 The Model

To explain the obtained results, I assumed that the adsorption process follows the first-order kinetics.[93,101,102] In the present approach, the equilibrium of the AuNP adsorption and desorption is given by the equation

$$S + \text{AuNP} \leftrightarrow S\text{AuNP}, \tag{6}$$

where S denotes a vacant site on the surface and SAuNP stands for a nanoparticle bound to the surface site. The deposition kinetics of AuNPs is characterized in terms of the fractional coverage of the surface, θ, by the following equation:

$$\frac{d\theta}{dt} = k_{ads}\, B\,(\theta) - k_{des}\theta \tag{7}$$

where the coefficient k_{ads} is the limiting deposition flux of the NPs onto the uncovered surface and the product $k_{des}\theta$ is the flux of the NPs desorbing from the surface. It is assumed that k_{des} does not depend on the coverage of the surface nor on the concentration of NPs in the solution. The quantity $B(\theta)$ is referred to as the blocking function[93,102] and measures the fraction of the surface that is available for the oncoming AuNPs. The blocking function obeys the following conditions: $B(\theta) = 1$ for $\theta = 0$, and $B(\theta) = 0$ for $\theta = \theta_{max}$, where θ_{max} is the maximum coverage of the surface. I apply the blocking function in its simplest form:

$$B(\theta) = \theta_{max} - \theta. \tag{8}$$

In eq. (7), the coefficient k_{ads} is proportional to the concentration, $C_{NP}^{ads}(\delta_a)$, of the AuNPs in the adsorption layer[93,102,103,104] at a distance δ_a from the surface. It can be written as the following product:

$$k_{\mathrm{ads}} = k_{\mathrm{a}} C_{\mathrm{NP}}^{\mathrm{ads}}(\delta_{\mathrm{a}}), \tag{9}$$

where k_{a} is the adsorption rate constant. The concentration of NPs in the adsorption layer grows with the bulk concentration of AuNPs, C_{NP}. The exact form of the relationship between C_{NP} and $C_{\mathrm{NP}}^{\mathrm{ads}}$ is, however, not needed in our discussion. What is important is that the coefficient k_{ads} does not depend directly on the bulk concentration of the AuNPs, but on $C_{\mathrm{NP}}^{\mathrm{ads}}$. Note also that, if the coefficient k_{ads} was proportional to the NP bulk concentration, that is, $k_{\mathrm{ads}} = k_{\mathrm{a}} C_{\mathrm{NP}}$, eq. (7) would represent the Langmuir adsorption equation (the Langmuir isotherm). In the Langmuir isotherm, no interaction between adsorbing particles is assumed. In the present study, significant interactions between the AuNPs, especially in the adsorption layer, are anticipated. This is the reason why the coefficient k_{ads} follows the dependence given by eq. (9).

Under the assumption that C_{NP} is constant during the adsorption process, the solution of eq. (7) with the blocking function given by eq. (8) reads

$$\theta(t) = \theta_{\mathrm{sat}} \left[1 - \exp(-(k_{\mathrm{ads}} + k_{\mathrm{des}})t)\right] \tag{10}$$

where the saturation value of the fractional coverage, θ_{sat}, is given by the following formula:

$$\theta_{\mathrm{sat}} = \theta_{\mathrm{max}} \frac{k_{\mathrm{ads}}}{k_{\mathrm{ads}} + k_{\mathrm{des}}} \tag{11}$$

To check if the amount of the AuNPs adsorbed on the glass slide affects the bulk NP concentration, I compared the absorbance of five different glass slides that were dipped consecutively in the same AuNP solution for about 30 min. Within experimental error, no difference in the absorbance kinetics between the first and the last slide could be observed, even for the lowest AuNP concentration used (C_{025}). This result justified the assumption that the NP concentration was constant during the process and the adsorption of AuNPs did not alter either k_{ads} nor φ_{max}. Otherwise, if the amount of AuNPs adsorbed affected the bulk AuNP concentration, the absorbance kinetics of the last slide immersed would be different from that of the first one.

The absorbance, φ, of the glass interface is measured in arbitrary units. I treat it here simply as a dimensionless quantity. It is proportional to the surface density of the adsorbed AuNPs for a wide range of surface coverages.[105] For this reason, eq. (10) describes the time evolution of both the fractional surface coverage, $\theta(t)$, and the absorbance $\varphi(t)$. While fitting the kinetic model to the experimental absorbance data, I employed φ instead of θ. In my calculations, I treated the maximum absorbance, φ_{max}, and the two coefficients, k_{ads} and k_{des}, as the fitting parameters. In the following, I refer to eq. (10) as the model of the time evolution of the absorbance, $\varphi(t)$.

4.1.4 Experimental Validation of the Model

For low salt concentrations, below ~20 mM, the deposition process is driven by electrostatic interactions and the adsorption of the AuNPs is highly irreversible.[93] I conducted a series of experiments to check to what extent the process is irreversible for higher ionic strengths, above 2.0 M. I found that the absorbance data collected for the mixtures of AuNPs and a 2.0 M solution of NaCl follow the time dependence given by eq. (10) for all component concentrations employed. (I found that the data obtained for mixtures of AuNPs and other salts also followed the kinetic model, but systematic studies involving different component concentrations were carried out for NaCl only).

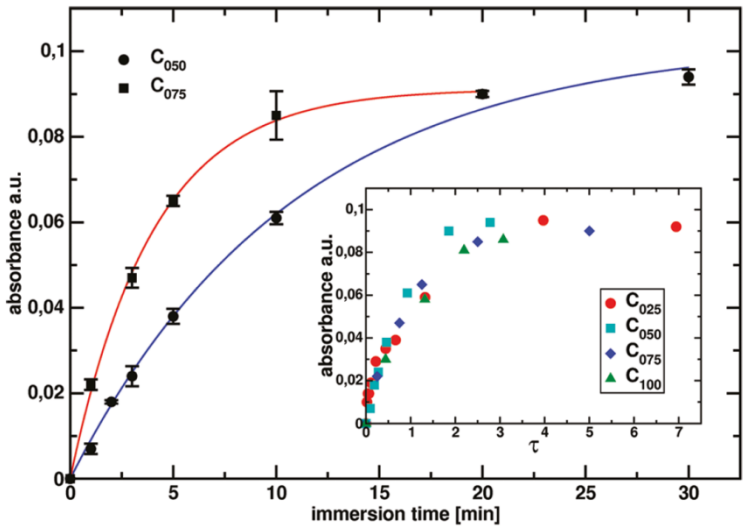

Figure 23 Dependence of the absorbance, φ, on the immersion time, t, for the salt concentration C_{salt} = 2.0 M for two NP concentrations, C_{050} and C_{075}. Inset: time dependence of the absorbance for four NP concentrations, C_{100}, C_{075}, C_{050}, and C_{025}, plotted in the rescaled time $\tau = t \times k_{ads}$.

The absorbance data for two selected AuNP concentrations, C_{075} and C_{050}, are shown in Figure 23. Also, in Figure 23, the dependencies of the absorbance are plotted in the rescaled time, $\tau = t \times k_{ads}$. As seen, after the rescaling, the functions $\varphi(\tau)$, collapse onto a single curve.

The most remarkable property of the plots presented in Figure 23 is that the saturation value of the absorbance, φ_{sat}, was, within experimental error, the same for all mixtures used, irrespective of the AuNP concentration. The bulk concentration of the AuNPs affected only the adsorption rate, and for higher AuNP concentrations, φ_{sat} was reached faster. This follows that the AuNP bulk concentration in all mixtures was high enough to provide the same value of saturation coverage. . It follows that the fraction in eq. (11), $k_{ads}/(k_{ads} + k_{des}) = k_a C_{NP}/(k_a C_{NP} + k_{des})$, does not depend on the NP concentration, C_{NP}. In terms of the model's parameters this condition is fulfilled when $k_{ads} >> k_{des}$ so that the fraction is close to unity, $k_{ads}/(k_{ads} + k_{des}) \approx 1$. Consequently, the adsorption process can be, to a good approximation, regarded as irreversible for the AuNP concentrations used. According to eq. (9), the value of the adsorption coefficient, k_{ads}, increases with C_{NP}, whereas the desorption coefficient, k_{des}, does not depend on the concentration of AuNPs in the bulk solution. It follows from eq. (11) that, if the adsorption process was reversible, one would observe a decrease of the value of the saturation absorbance with decreasing C_{NP}, and the saturation absorbance would approach the limiting value, φ_{max}, for sufficiently high AuNP concentrations. To verify whether the desorption of the AuNPs can be neglected in the model, additional series of experiments were carried out. I simulated a sudden change of the AuNP concentration from C_{100} to zero in the solution. In each experiment, the glass slide was immersed in a solution containing 2.0 M NaCl and AuNPs in different concentrations for a time (2 h) that was sufficient to reach the saturation coverage of the surface. The slide was then removed from this solution and transferred immediately into 2.0 M aqueous solution of NaCl. (Note that, after drying, the layer of AuNPs adsorbed became permanently bound to the surface.) The slide was kept in the solution of the salt for a long time (up to 24 h) and then investigated using UV-Vis spectroscopy. I found that the absorbance of the glass slide hardly decreased after transfer into the salt solution. To quantify the AuNP desorption process, I fitted eq. (10) to the experimental data, assuming that, after immersion in the aqueous solution of NaCl, only desorption of the AuNPs from the surface takes place. The absorbance of the slide, $\varphi(t)$, decays then exponentially with time, according to the following equation

$$\varphi(t) = \varphi_{sat} \exp(-k_{des} t) \qquad (12)$$

where φ_{sat} is the absorbance corresponding to the saturation coverage of the glass slide. From the least-squares fit of the experimental data to eq. (12), I estimated the value of the desorption coefficient as k_{des} ~10^{-5} 1/s. The solid lines in Figure 23 represent the least-squares fits of eq. (10) with $k_{des} = 0$

$$\varphi(t) = \varphi_{max}\,[1 - \exp(-k_{ads}t)] \qquad (13)$$

to the adsorption data. The obtained values of k_{ads} varied – from k_{ads}~ 7.3 × 10^{-3} 1/s for the highest AuNP concentration, C_{100}, to k_{ads} ~3.7 × 10^{-4} 1/s for the lowest AuNP concentration used, C_{025}. (The dependence of the adsorption coefficient on the bulk concentration of NPs is discussed in more detail later in this section.) It follows that, for all AuNP concentrations employed, k_{des} was significantly smaller than k_{ads}. Therefore, the desorption of AuNPs can be neglected and eq. (13) can be employed to model the deposition process.

4.1.5 Effect of Salt Concentration

To investigate the effect of salt concentrations on the adsorption process, I studied the adsorption process in mixtures containing AuNPs in a concentration of C_{100} for 10 different NaCl contents: C_{salt} = 0.001, 0.01, 0.1, 0.50, 0.75, 1.0, 2.0, 3.0, 4.0, and 4.6 M. For each salt concentration, I determined the dependence $\varphi(t)$ and calculated the quantities φ_{max} and k_{ads} from the fit of eq. (13) to the absorbance data. The saturation absorbance and the adsorption coefficient are plotted as functions of the salt concentration in Figure 24. For all salt concentrations the kinetic model with k_{ads} >> k_{des} was employed. The values of the ζ-potential as a function of C_{salt} are shown in Figure 25. It was found that, for salt concentrations in the range from 0.6 M to 1.75 M, the mixtures were unstable against aggregation. On the basis of the results presented in Figure 24 and Figure 25, combined with the stability data, one can distinguish the following four adsorption regimes for different salt concentration ranges:

Regime I for $C_{salt} \leq 0.5$ M. The system was stable against aggregation, and the values of the ζ-potential decreased from about 49 mV for the mixture containing no salt to about 12 mV for C_{salt} = 0.5 M. For the lowest salt concentrations, the saturation absorbance was achieved relatively fast, but the deposited AuNPs formed a sparse layer.

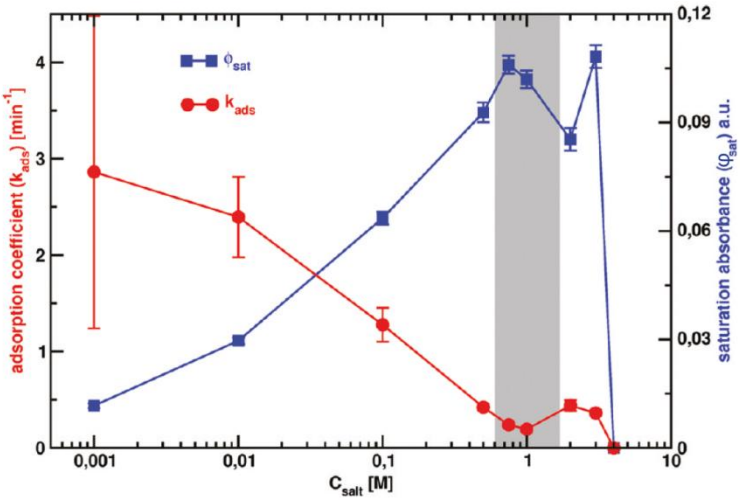

Figure 24 Dependence of the adsorption coefficient, k_{ads}, the red plot, and the saturation absorbance, φ_{sat}, the blue one, on the concentration, C_{salt}, of NaCl in the solution. The results were obtained for mixtures containing AuNPs in a concentration of C_{100}. The unstable regime is marked in gray.

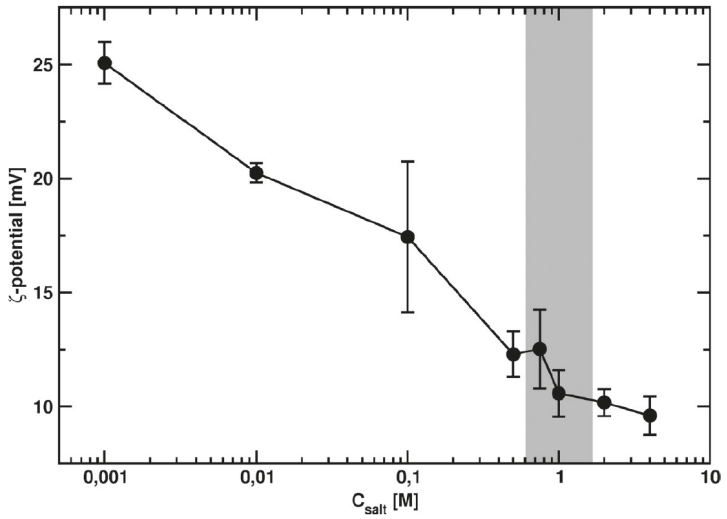

Figure 25 Dependence of the ζ-potential on the concentration, C_{salt}, of NaCl in the solution. The unstable regime is marked in gray.

The values of k_{ads} decreased and φ_{max} increased, to a good approximation exponentially, with increasing salt concentration. For C_{salt} = 0.5 M, both the saturation absorbance and the adsorption coefficient attained values that did not change much for higher salt concentrations. An SEM image of the NPs adsorbed on the silicon surface in this regime, for C_{salt} = 1.0 mM, is shown in Figure 26a.

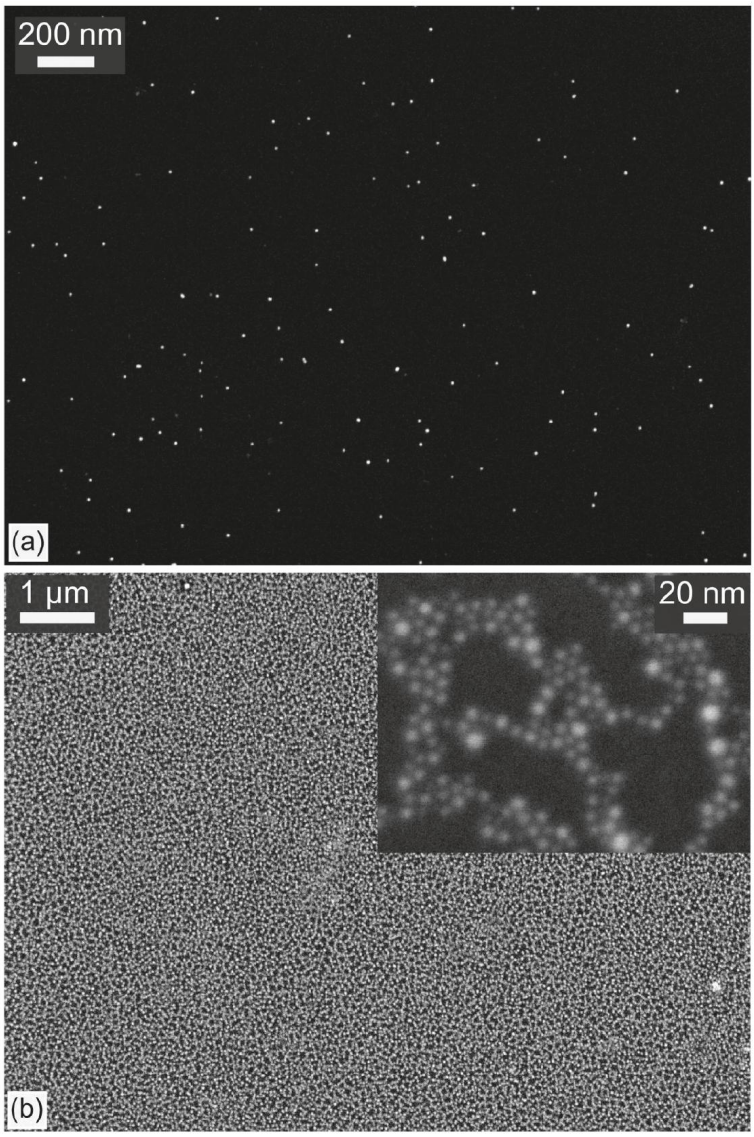

Figure 26 Effect of salt content on the saturation coverage. SEM images of the coverage obtained for C_{salt} = 1mM (a) and C_{salt} = 2M (b). In both cases, the AuNP concentration C_{100} was employed. The inset picture shows details of the image in (b).

Regime II for 0.6 M ≤ C_{salt} ≤ 1.75 M. In this regime, the system was unstable, and the ζ-potential decreased from ~12 to ~10 mV. The aggregation of AuNPs occurred very slowly, and a precipitate appeared after a few hours. The adsorbed AuNPs formed a dense layer on the surface (surface coverage of 50%). In Regime II, both k_{ads} and φ_{max} slightly decreased with the salt concentration.

Regime III for 2.0 M ≤ C_{salt} ≤ 3.0 M. The system was stable against AuNP aggregation, and the values of the ζ-potential were around 10.5 mV. The values of the saturation absorbance were similar to those observed for the unstable solutions, in Regime II. In this regime, k_{ads} and φ_{max} exhibited non-monotonic behavior with increasing salt concentration: k_{ads} and φ_{max} attained, respectively, local minimum and

maximum in this regime. An SEM image of the NPs adsorbed on the surface for C_{salt} = 2.0 M is shown in Figure 26b.

Regime IV for C_{salt} ≥ 4.0 M. The system was stable, and the ζ-potential attained the value of ~10.0 mV and slightly decreased with increasing salt concentration. In this regime, the adsorption was not observed. (As I checked, the same behavior was observed also for C_{salt} = 4.6 M).

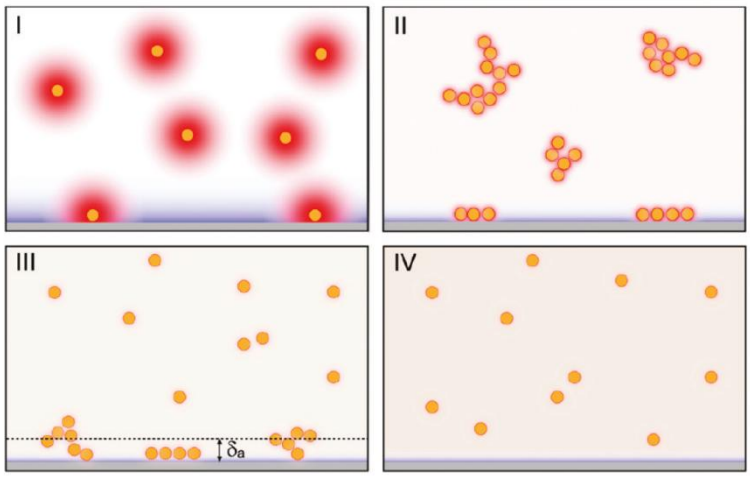

Figure 27 Cartoon representation of the system's behavior in the four adsorption regimes: (I) The adsorption is driven mainly by the electrostatic interactions. Positively charged NPs adsorb onto the negatively charged surface and form sparse layers. The adsorption rate decreases, whereas the saturation coverage increases rapidly with the salt content. (II) The system is unstable, and the AuNPs adsorb and form dense layers. (III) The system is stable, and the AuNPs adsorb via surface-induced aggregation, which takes place in the adsorption layer of the thickness δ_a, to form dense layers. (IV) The system is stable, and no adsorption occurs.

The behavior of the system in the four regimes is summarized in Figure 27. The deposition of AuNPs observed for low salt concentrations (Regime I) is driven by the electrostatic interactions of positively charged NPs and the negatively charged substrate. Under the assumption that the ζ-potential is the potential at the particle surface, the effective charge, Q_{eff}, over each AuNP can be estimated from the following formula:

$$Q_{eff} = 4\pi\varepsilon_0\varepsilon\zeta R \qquad (14)$$

where ε_0 is the permittivity of a vacuum, ε is the dielectric constant of the solvent, and ζ stands for the ζ-potential. For low salt concentrations ε ~80. For a solution containing no salt (ζ = 49 mV), eq. (14) yields Q_{eff} = 10.8 e, where e is the elementary charge. For C_{salt} = 1.0 mM, one gets Q_{eff} = 5.5 e. The Debye screening length is estimated from the relation $K^{-1} = (\varepsilon_0\varepsilon k_B T/2C_{salt}e^2)^{1/2}$, where k_B is the Boltzmann constant and T is the

temperature. For the solution containing 1.0 mM NaCl, K^{-1} ~10 nm. Thus, the high values of k_{ads} observed can be attributed to the long-range electrostatic attraction between the AuNPs and the charged surface. The AuNPs adsorbed form a positively charged layer that prevents NPs from the bulk of solution from approaching the surface. Interestingly, I checked that the layer of AuNPs adsorbed from the solution containing 2.0 M NaCl, which is much denser than those obtained for low salt concentrations, is stable after being transferred into solutions of low salt concentration. Specifically, using the UV-Vis spectroscopy, I found that such a layer remained unchanged for several hours after the immersion in pure deionized water and in a solution containing 0.5 M NaCl. This result indicates that the values of φ_{max} attained in Regime I are small because of the repulsive electrostatic barrier created by the deposited AuNPs. As the concentration of NaCl increases, both the Debye length and the effective charge on NPs decrease. Eventually, the dispersive (van der Waals) interactions start to dominate over the repulsive electrostatic forces between the AuNPs. This renders the system unstable, and in Regime II, aggregation of NPs takes place in the bulk solution. Because the aggregates (clusters) possess a positive net charge, they are attracted by the negatively charged substrate. However, because the screening length is very short in this regime (below 1 nm), the clusters are adsorbed only when they diffuse close to the surface. For this reason, the values of the adsorption coefficient are significantly smaller than those observed for low NaCl concentrations. On the other hand, because K^{-1} is small, the electrostatic barrier is very weak and, consequently, AuNPs can form a layer that is much denser as compared with those in Regime I for a small salt content.

Surprisingly, for higher salt concentrations, in Regime III, the system regains stability. I checked that the AuNP aggregation did not occur even for several months after the mixture preparation. For C_{salt} = 2.0 M, ε ~55[106] and, from eq. (14), one gets Q_{eff} ~1.5 e. In this regime, K^{-1} ~0.1 nm. It follows that the electrostatic repulsive interactions between the AuNPs can be completely ignored. Most likely, for the stabilizing effect, other repulsive forces are responsible that are induced by the presence of the Na^+ and Cl^- ions, such as structural (hydration) forces.[107] These forces arise from hydration of adsorbed counterions and charged functional groups on the surface. The repulsion is due to the work that is needed to remove water molecules when two surfaces approach each other. Note also that the surface charge density on the silicon substrate increases with the ionic strength of the solution.[108] This effect is especially pronounced for pH ≥ 7.

Probably, the growth of the surface charge density caused by the increase of the ionic strength is sufficient to overcome the repulsive forces, and AuNPs can adsorb on the surface to form dense layers. The mechanism of the adsorption in this regime is discussed in more detail in the next section.

I also checked that the effect of the high ionic strength of the salt on the AuNP deposition is observed for other systems. I investigated the adsorption process for the following salts: KSCN, Na_2CO_3, $NaC_2H_3O_2$, $NaNO_3$, and $KNaC_4H_4O_6$. Mixtures containing AuNPs in a concentration of C_{100} and salts in the 2.0 M concentration were employed. For each salt used, the adsorption took place and the slide was covered with a durable layer of AuNPs. The values of the saturation absorbance were similar to that obtained for NaCl.

For the highest salt concentrations, in Regime IV, the repulsive hydration forces dominate also over the electrostatic interactions between the surface and the AuNPs. The system is stable against aggregation, and the adsorption is not observed. Using the UV-Vis spectroscopy, I found that the AuNP layer formed in the solution containing 2.0 M NaCl (that is, in Regime III) vanishes completely after being immersed in 4.0 M NaCl solution. The AuNP desorption process was fairly fast and was completed after a few minutes.

4.1.6 Dependence of the Adsorption Rate on the NP Concentration in Regime III

As mentioned in the previous section, in Regime III, for C_{salt} = 2.0 M, the rate of adsorption increased with the concentration of AuNPs. To quantify this observation, I determined the dependence of the adsorption coefficient, k_{ads}, on the NP concentration, C_{NP}, in mixtures containing 2.0 M NaCl. I found that the function $k_{ads}(C_{NP})$ follows the power law

$$k_{ads} \sim {C_{NP}}^{\alpha} \tag{15}$$

with the exponent α = 2.12 ± 0.09. The dependence of k_{ads} on C_{NP} is plotted in Figure 28.

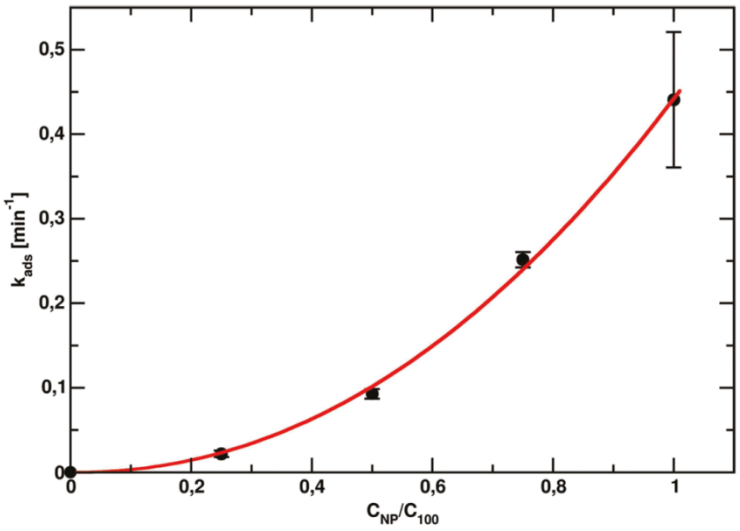

Figure 28 Dependence of the adsorption coefficient, k_{ads}, on the concentration of the NPs, C_{NP}, expressed relative to the concentration C_{100}. The fit of the power-law function to the data (solid line) yielded the exponent $\alpha = 2.12 \pm 0.09$.

The fact that k_{ads} grows—with a good approximation—with the square of C_{NP} indicates that some collective effects, such as aggregation or flocculation of AuNPs, must be involved in the adsorption process. Additional evidence for the presence of the aggregation effects is provided by the SEM images of the AuNP layers on silicon substrates. Figure 8 shows an SEM image of a portion of a silicon surface covered with AuNPs. The layer is sparse because the adsorption process was terminated at the early stage. As can be seen, the AuNPs form small two-dimensional clusters on the surface. Typically, the clusters are composed of 10-20 AuNPs.

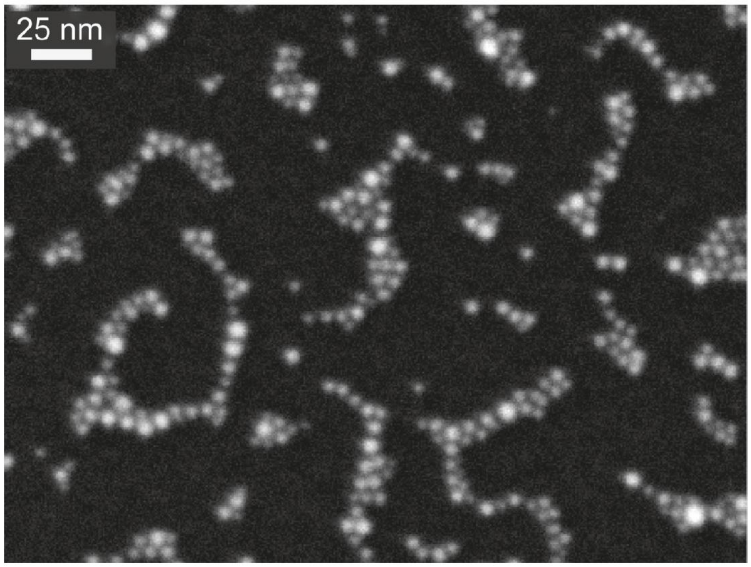

Figure 29 SEM image of a silicon surface covered with NPs. The silicon slide was immersed for 1 min in a solution containing NPs in a concentration of C_{100} and 2.0 M NaCl.

Because the solution is stable, I can infer that the aggregation process takes place only in the region close to the surface and stops when all available sites are occupied by the AuNPs, that is, when θ reaches θ_{max}. Although the mechanism responsible for the surface-induced AuNP aggregation has yet to be explained, the power-law dependence given by eq. (15) can be derived based on Smoluchowski's theory[109] of flocculation. According to this theory, the total number, N, of particles undergoing aggregation follows the second-order kinetics and is described by the following rate equation

$$\frac{\mathrm{d}N}{\mathrm{d}t} = k_{\mathrm{agg}} {C_{\mathrm{NP}}}^2 \tag{16}$$

where k_{agg} is some effective aggregation constant. As was discussed in the previous section, the adsorption coefficient is the flux of the AuNPs ongoing on the surface. It follows, therefore, that $k_{ads} \sim \mathrm{d}N/\mathrm{d}t$ and, consequently, $k_{ads} \sim {C_{NP}}^2$, as observed in my experiments.

4.1.7 Conclusions

In this section I describe the effect of salt on the kinetics of the adsorption of positively charged AuNPs on negatively charged substrates. The deposition process was studied for a wide range of salt concentrations, from 0 (no salt) up to 4.6 M. The studies revealed that, depending on the salt content in the solution, the following four adsorption regimes can be distinguished: (1) For small salt concentrations, the adsorption proceeds quickly but gives low surface coverage. In this regime, the process is controlled by the electrostatic forces. The saturation coverage increases, whereas the adsorption rate decreases rapidly with the salt concentration. (2) For sufficiently high salt concentrations (about 0.6 M), the system becomes unstable and aggregation of the AuNPs occurs in the bulk. This is the salting-out effect caused by the screening of the electrostatic repulsion between the AuNPs. In this regime, the AuNPs adsorb to form dense layers with the surface coverage reaching about 50%. (3) Unexpectedly, I found that the system regains its stability upon increasing the salt concentrations above 2.0 M. This effect can be attributed to the repulsive solvation forces that dominate over the dispersive (van der Waals) attraction. In this regime, adsorption takes place and the AuNPs form dense layers. It was also found that the adsorption constant grows with the square of the AuNPs' concentration and can be argued that the adsorption process

occurs through the surface-induced aggregation. (4) Further increase in the ionic strength (above 4.0 M for NaCl) results in cessation of the adsorption process. To my knowledge, the present study is the first to report the formation of monolayers by charged AuNPs in a high salt concentration regime. These findings provide a facile method for coating solid substrates with a layer of AuNPs of prescribed density, which can be controlled by the deposition time, as well as by salt and AuNP concentration.

4.2 Deformations of the shape of AuNPs caused by a deposition on a solid substrate

4.2.1 Introduction

Deposition of AuNPs on a solid substrate followed by oxygen plasma treatment is a commonly used protocol for surface functionalization. Surprisingly, the effect of the deposition process on the morphology of the AuNPs is usually overlooked in research. Here, I investigated morphological changes caused by adsorption of small ligand-capped AuNPs (~5 nm in diameter) onto a silicon substrate. AuNPs coated with positively and negatively charged, as well as uncharged, ligands have been investigated. I found that upon the adsorption the AuNPs undergo plastic deformations and their shapes can be approximated by spherical caps. The degree of the deformation depends strongly on the AuNP organic coating.

4.2.2 Preparation and analysis of samples

Preparation of silicon strips

In this experiment the samples are silicon strips covered with AuNPs. Before use as a solid substrate, the bare wafers were cut manually into strips and cleaned by sonication in water and then in acetone. Next, the plates were immersed in a freshly prepared piranha solution (95% H_2SO_4:30% H_2O_2, 3:1 v/v) for 3 h. Finally, the plates were rinsed with deionized water and then with methanol, and dried in air. Note that the outer layer of the silicon plate is readily oxidized to SiO_2. However, it is not known either what portion of the surface is oxidized or the depth of the oxidized layer. For this reason, in the present dissertation I refer to the substrate as to the silicon or SiO_x one.

Preparation of AuNPs

In the experiments described below, I examined both hydrophobic and hydrophilic (positively or negatively charged) AuNPs The uncharged AuNPs were synthesized according to the procedure of Jana and Peng,[83] in which hydrophobic AuNPs covered with dodecylamine (Au@DDA NPs) are formed. The obtained Au@DDA NPs had an average radius of 2.5 nm with polydispersity 0.71 nm, as determined from the SAXS spectrum of the AuNP solution. To provide a positive or negative charge on the AuNPs I applied the method described in the Experimental section.

Immobilization of the AuNPs on the silicon strips

Positively-charged AuNPs were immobilized on the silicon using the ionic-strength controlled deposition method[84] described in detail in section 4.1. This method facilitated the obtaining of coatings of different densities. In the presented experiments I investigated two types of AuNP coatings: low- and high-density ones. In experiments where drop casting instead of an ionic-strength controlled method was used, I simply put a drop of AuNP solution on the silicon. I waited until all the solvent evaporated, and then rinsed the silicon plates consecutively with water and methanol and dried them in the air.

Analysis of samples

The percentage surface coverage, θ, was determined using a histogram tool in the graphic software. The AuNP number and projected radii were determined manually.

4.2.3 Geometry of the AuNPs before and after deposition

The morphology of the TMA-covered AuNPs deposited on the silicon substrate was investigated with SEM microscopy. In the case of low-density coating the AuNPs were distributed uniformly (Figure 30, left image) and formed a sparse layer. The percentage surface coverage, calculated as the ratio of the sum of the projected areas of all objects to the area of the image analyzed, was θ ~7%. In the case of the high-density coatings, the AuNPs were arranged in a network of connected patches (Figure 30, right image), covering about 20% of the surface.

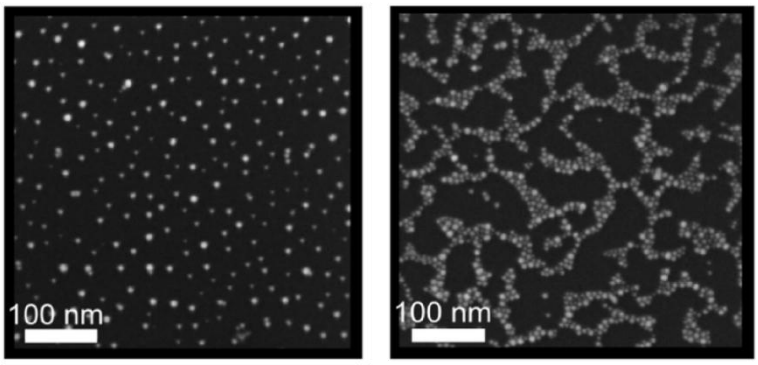

Figure 30 SEM images illustrating low-density (left) and high-density coating.

In both the cases, the average projected (apparent) radius of the adsorbed AuNPs, R_a, calculated from the SEM images, was R_a = (3.94 ± 0.08) nm. This value of the projected radius was significantly larger than that of the non-adsorbed AuNPs in the solution, R_0 = 2.5 nm, calculated based on SAXS measurements. Analysis of the side-view

SEM images revealed that the increase of the projected radius was caused by the deformation of the shapes of the AuNPs. As can be seen in Figure 31, the AuNPs attached to the surface are clearly flattened and resemble portions of spheres. It was also found that the average contact angle, φ_a, of the AuNPs was $\varphi_a = (54.3 \pm 3.9)°$.

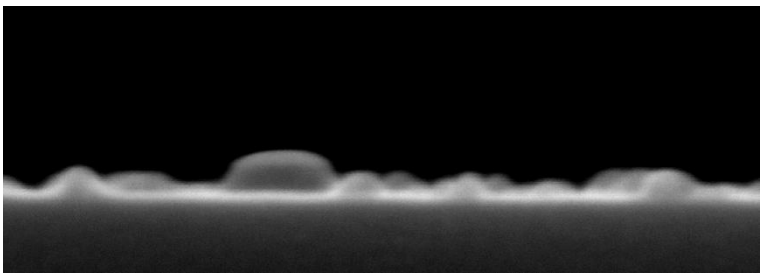

Figure 31 Side-view SEM image of the AuNPs deposited on the silicon.

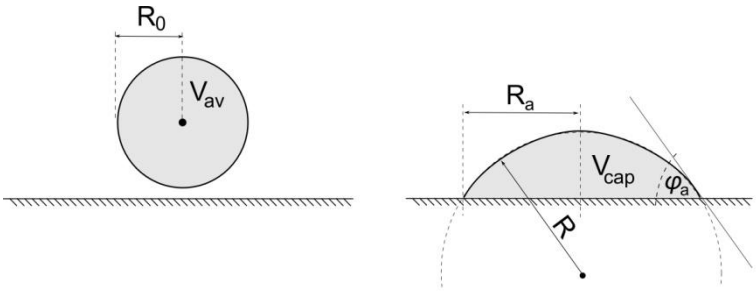

Figure 32 Geometry of the AuNP in the solution (left), and after deposition on the substrate (right).

The flattening of the metal cores that occurs during the adsorption process should be taken into account when estimating the sizes of AuNPs based on SEM or TEM images. The shapes of the adsorbed particles can also significantly affect the physical and chemical properties of the metal coating, such as its catalytic surface area. Thus, it is quite surprising that the effect of the deposition on the AuNP core is largely overlooked. In the following, I demonstrate that the shapes of the adsorbed AuNPs can be approximated as spherical caps. To show this, I start with the observation that the average volume of the AuNPs adsorbed on the substrate is equal to that of the average volume, V_{av} (see Figure 32), of the AuNPs in the bulk solution,

$$V_{av} = \frac{4}{3}\pi R_0^3 . \qquad (17)$$

The average volume of the AuNPs adsorbed on silicon is calculated as a volume of the spherical cap, V_{cap}, that is the following function of the contact angle, φ_a, and the radius, R, of the sphere (see Figure 32):

$$V_{cap} = \frac{\pi}{3} R^3 (2\text{-}3\cos\varphi_a + \cos^3\varphi_a). \quad (18)$$

The condition $V_{av} = V_{cap}$ yields the following expression for the radius R:

$$R = R_0 4^{1/3} \left(2\text{-}3\cos\varphi_a + \cos^3\varphi_a\right)^{-1/3}. \quad (19)$$

The projected area of the AuNP is the base of the cap, and its radius, R_a, is related to the radius R and the contact angle φ_a through the following relation:

$$R_a = \begin{cases} R\sin\varphi_a, & for\ \varphi_a \leq 90° \\ R, & for\ \varphi_a > 90° \end{cases} \quad (20)$$

The projected radius, R_a, is a quantity that is obtained directly from the SEM images. Equation (20) enables determination of the contact angle, φ_a, as a function of the ratio R_a/R_0. For R_0 = 2.5 nm and R_a = (3.94 ± 0.08) nm eq. (20) yields φ_a = (62.5 ± 4.4)°. It follows that – within statistical error – this value agrees with that determined directly based on the side-view SEM images. This result supports the assumption that the shapes of the deposited AuNPs can be approximated by spherical caps. Thereby, it rules out the possibility that those shapes visible in the SEM images may be due to the organic material present in the bottom of the particles.

The most plausible cause of the observed shape deformation of the AuNPs is the electrostatic attraction between the positively charged TMA ligands and negatively charged surface of the SiO_x substrate. The extent of the deformation indicates that – surprisingly – the AuNP core becomes plastic under the stresses caused by the electrostatic forces. To examine the effect of the electrostatic interaction on the resulting NP shape, I carried out experiments with AuNPs coated with both positively (TMA) and negatively charged (MUA) and uncharged (DDA) ligands. All types of the AuNPs were deposited with the same drop casting technique (the ionic-strength controlled method can be applied only for positively charged coating). To quantify the degree of deformation I calculated the ratio R_a/R_0 of the projected radius after deposition to the radius in a bulk solution, and the contact angle, φ_a. The contact angle was calculated from eq. (20) based on the R_a/R_0 ratio. The results are collected in Table 2. I found that positively charged AuNPs undergo the most significant deformations. Their average

projected radius is more than 150% of that in the bulk solution. For the DDA-coated uncharged NPs the degree of deformation is smaller (134%). This can be explained by the lower attraction between the AuNP ligand and the substrate surface. The negatively charged Au@MUA NPs that are electrostatically repelled from the silicon surface are only slightly deformed, and the increase of their projected radii, caused by the deposition, is less than 10%. I observed that the contact angle increased with decreasing attraction between the AuNP and the substrate. The value of φ_a changed from 62.2 degrees (corresponding to the "wetting" geometry) for positively charged TMA ligands to 113 degrees ("non-wetting" geometry) for negatively charged MUA ligands. The results shown in Table 2 suggest that the electrostatic interaction between organic ligands and solid substrate has a profound effect on the shape of the deposited AuNPs. Electrostatic forces are strong enough to make gold atoms move within the AuNP, and lead to significant deformation.

Table 2 Characterization of the degree of deformation for ligand-coated AuNPs deposited on a SiO_x substrate.

AuNP type	R_0, radius in bulk (nm)	R_a, projected radius (nm)	R_a/R_o	Contact angle (deg)
Au@TMA[1]	2.50	3.94 ± 0.08	1.58	62.5 ± 4.4
Au@TMA[2]	2.50	3.95 ± 0.06	1.58	62.2 ± 3.3
Au@DDA[2]	2.53	3.40 ± 0.07	1.34	82.4 ± 3.3
Au@MUA[2]	2.16	2.35 ± 0.04	1.09	112.9 ± 7.4

[1] Deposited using the ionic-strength controlled method.
[2] Deposited using drop casting method.

The analysis of the effect of plasma on the AuNPs shape presented in the following sections was done for Au@TMA NPs deposited using an ionic-strength controlled method that allowed the obtaining of coatings of various densities. I checked whether the morphology of the AuNP deposits obtained with this method is the same as for the simple drop casting technique. It was found (see Table 2) that the average projected radius for the drop casting method was (3.95 ± 0.06) nm. This value agrees very well with that obtained for the ionic-strength controlled method, (3.94 ± 0.08) nm. Thus, the changes of the AuNPs shapes do not depend on the deposition technique used.

The structure of the most deformed NPs (Au@TMA) deposited on the silicon substrate was also investigated by X-ray diffraction (XRD) analysis. The XRD studies revealed that – despite significant deformation of the initial spherical shapes – the adsorption process did not destroy the crystal structure (fcc) of the AuNPs. The XRD

pattern of the AuNP coating displayed one broad peak at 2θ = 38.3 degrees, corresponding to the Au (111) plane.

4.2.4 Conclusions

In this section I investigated changes in the morphology of ligand-capped AuNPs caused by deposition onto a silicon substrate. I studied deposition of the AuNPs coated with positively and negatively charged as well as uncharged ligands. I found that electrostatic forces between the ligand and substrate are strong enough to displace Au atoms within the core. In the process, the AuNPs undergo plastic deformations and take shapes that can be approximated as spherical caps. The final shape of the particle depends on the charge of the ligand coating. The strongest deformations (flattening) of the AuNP core were observed for positively charged ligands that are electrostatically attracted to the substrate. The smallest deformations occurred for a negatively charged coating that is repelled from the surface.

These findings reveal the interesting adjustability of the gold nanocrystals and present a new type of impact of the organic shell on the properties of the whole nanoparticle. These results also highlight an important aspect of determining particle size from the SEM or TEM spectra – using such methods one should remember that the radius of the immobilized NPs differs from the radius of the same particle suspended in a solution.

4.3 Morphological changes of AuNPs due to oxygen plasma treatment

4.3.1 Introduction

Two-dimensional (2D) structures formed by AuNPs deposited on a solid substrate are widely employed in light emitting devices, solar cells, and antireflective films, as catalysts for carbon nanotubes growth, or for the vapor-liquid-solid growth of inorganic nanowires.[110] AuNPs used in deposition procedures are typically covered with an organic protecting layer that prevents AuNP aggregation in a solution. After immobilization on a surface, this organic layer is usually no longer needed and often has to be removed from the AuNPs. The removal of the organic material involves either thermal or plasma treatment. In the present study I have focused on the latter cleaning method.

Treatment with oxygen plasma is a technique utilized both in the purification of bulk gold[111] and AuNPs.[112,113,114] In the highly reactive gas, organic compounds are oxidized and removed by a vacuum system as carbon, sulfur, and nitrogen oxides. Surprisingly, despite the popularity and usefulness of the plasma treatment, knowledge about the processes which take place in a plasma cleaner is poor. There are conflicting opinions in the literature on this issue. In particular, the discrepancies concern the impact of the oxygen plasma on the structure of the AuNP deposit. Some authors report that long exposure of AuNPs to oxygen flow did not alter either their regular structure or the initial arrangement of the AuNPs on the substrate.[113,115] According to other reports, even short-time and low-power (10 W) plasma cleaning significantly alters the initial morphology of the deposit, causing coarsening of the AuNPs.[116] One can also find the opinion that high oxygen plasma power (>300 W) is needed to destroy the structure of the deposit. In this case, a break in the linkage between the AuNPs and the SiO_x substrate takes place, resulting in the removal of AuNPs from the surface.[112] Given such diverse opinions on the effects of oxygen plasma treatment, it is obvious that the nature of this process is far from being well-understood.

In this section I present the results of my work on the effect of the plasma cleaning process, and elucidate its impact on the morphology of the AuNPs. I apply low-power oxygen plasma to the AuNPs immobilized on a silicon substrate using the ionic strength-controlled deposition of charged NPs[84] described in section 4.1. I show that during the plasma treatment the AuNPs behave like droplets of a non-wetting liquid,

exhibiting the ability to move and merge. I also argue that the AuNP coarsening is dominated by a diffusion coalescence mechanism and show that time evolution of the surface AuNPs density follows the Smoluchowski coagulation equation. The diffusivity of the AuNP scales with its mass as $D(m) \sim m^{-\alpha}$ with $\alpha = 2.6$.

4.3.2 Preparation and analysis of samples

In the presented experiments I used silicon plates covered with AuNPs, prepared with the ionic-strength controlled method[84] described in section 4.1 and in the Experimental section. So prepared, the samples were kept in the plasma cleaner for a prescribed time and then analyzed with SEM. The droplet (AuNP) surface densities were determined independently for each plasma treatment time and calculated as averages for three independent experiments and for three SEM images in every experiment.

The plates covered with the AuNPs were treated with oxygen plasma for various times at 29.6 W in Harrick Plasma Cleaner PDC-002 (Harrick Plasma, USA). The percentage surface coverage, θ, was determined using a histogram tool in the graphic software. The AuNP number and projected radii were determined manually.

4.3.3 Morphology of the AuNP deposit after the plasma treatment

In the previous section (4.2), changes in the morphology of ligand-capped AuNPs caused by deposition onto silicon substrate were described. I found that in the process the AuNPs undergo plastic deformations and take shapes that can be approximated as spherical caps. As is presented below, cleaning with oxygen plasma also considerably affects the AuNP shape.

After the plasma treatment, a significant coarsening of the AuNPs was observed in both low- and high-density coating. In the case of the low-density coating the resulting particles possessed circular projected shapes of an average radius R_p = (7.51 ± 0.36) nm (see Figure 33a). The sizes of the particles span from about 4 to 16 nm. The percentage surface coverage, θ, decreased about 2.3 times (from ~7% to ~3%). After the plasma treatment, the number density of the AuNPs was reduced 5.2 times. In the case of high-density coatings, the plasma cleaning led to the formation of objects possessing rather irregular and elongated shapes, up to 70 nm in length. The average projected particle radius was about 12 nm. (Due to irregular shapes of plasma-treated AuNPs, their radii were calculated as radii of spheres of the same projected area.) Interestingly, the plasma treatment resulted in a 2.2-fold decrease of the initial surface coverage (from ~20% to

~9%), which is close to that observed for the low-density coatings. The number density of the AuNPs on the substrate was 6.1 times smaller than before the process of the plasma treatment.

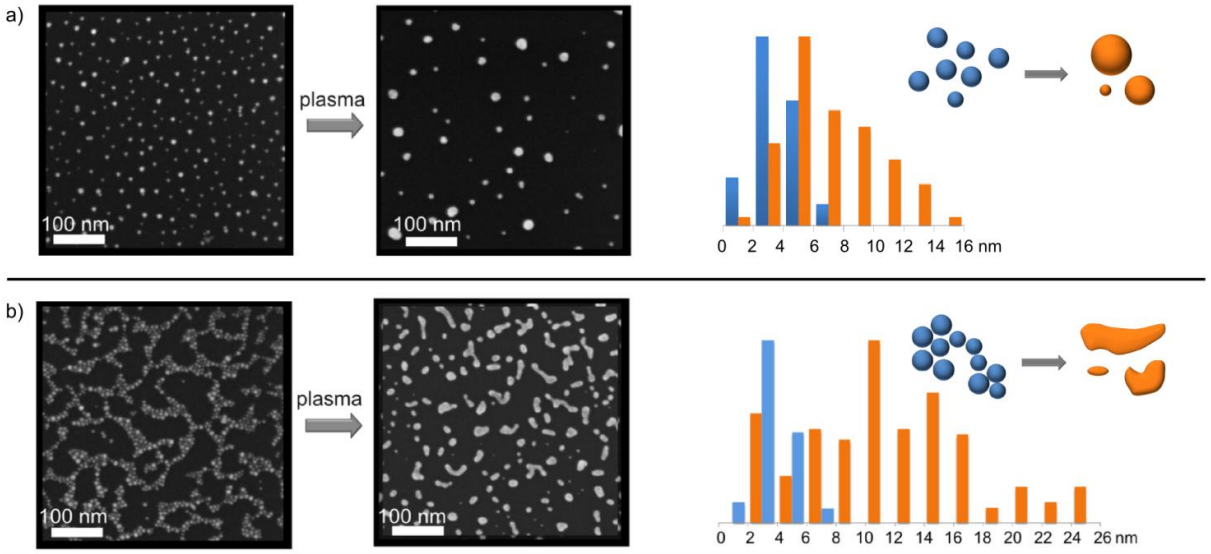

Figure 33 SEM images illustrating the effect of the plasma treatment on the AuNPs deposited on a silicon plate for low-density (a), and high-density (b) coatings. The histograms show distributions of the AuNP projected radii before (blue) and after (orange) the plasma treatment. For the high-density coating the radii were calculated as radii of spheres of the same projected area.

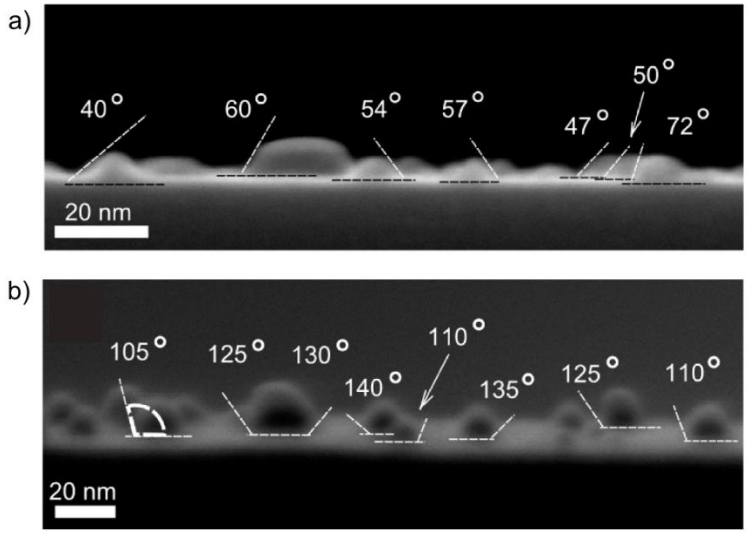

Figure 34 Side-view SEM image of the AuNPs deposited on the plate (a) before and (b) after the plasma cleaning. Values of the contact angles for selected AuNPs are shown.

From the side-view SEM images (shown in Figure 34b and Figure 35c) I found that the average contact angle, φ_p, of the particles formed after the plasma treatment was φ_p = (122.5 ± 4.5) degrees. However, only small- and medium-sized particles (<20 nm) had shapes that could be approximated by portions of spheres. Larger particles exhibited less regular shapes. Despite a visible change in the shape of the AuNPs, their

crystallographic structure is preserved. The XRD pattern after the plasma treatment displayed a broad peak at 2θ = 38.3 degrees that corresponds to the Au(111) plane.

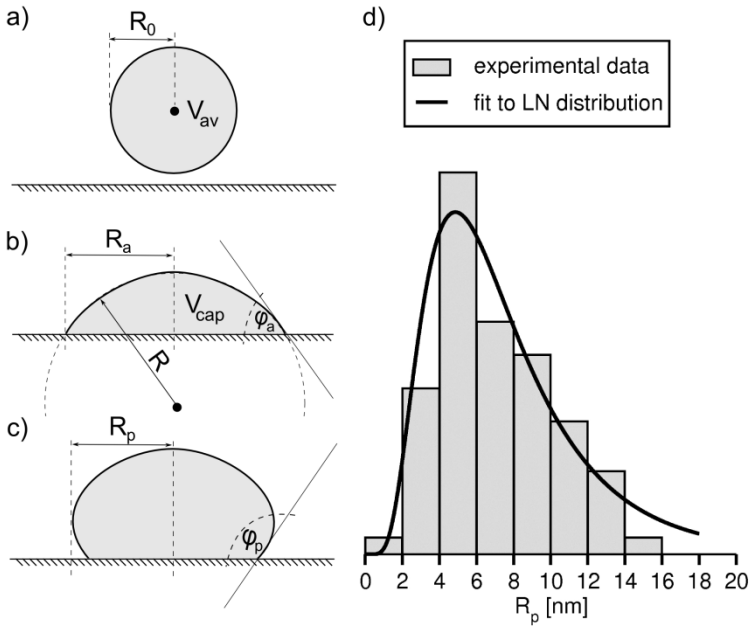

Figure 35 Geometry of the AuNP (a) in the solution, (b) after deposition on the substrate, and (c) after the plasma treatment. (d) Distribution of the projected radii, R_p, of the AuNPs after the plasma treatment. The solid line is the fit of the log-normal (LN) distribution.

The resulting distribution of the projected radii of the droplets was investigated. In my studies, I analyzed the low-density coatings because only in this case did the projections of the AuNPs possess well-defined circular shapes (see Figure 33a). Distribution of the droplet radii after the plasma treatment process exhibited a clear positive skewness, as shown in Figure 35d. To quantify this distribution, I fitted to the obtained frequency the log-normal (LN) distribution function given by

$$f_{\mathrm{LN}}(R_{\mathrm{p}}) = \frac{1}{\sqrt{2\pi}\sigma R_{\mathrm{p}}} \exp\left[-\frac{1}{2}\left(\frac{\ln R_{\mathrm{p}} - \ln\mu}{\ln\sigma}\right)^2\right], \qquad (21)$$

where $\ln\mu$ and $\ln\sigma$ are the mean and standard deviation of $\ln R_{\mathrm{p}}$, respectively. The fitting procedure yielded μ = 6.590 nm and σ = 1.824. To check whether the frequencies shown in Figure 35d follow the LN distribution, the Chi-square goodness-of-fit test was carried out. For the LN distribution function, given by eq. (21) fitted to the experimental data, the test statistic was χ^2 = 4.492. For four degrees of freedom $P(\chi^2 > 4.492)$ = 0.34. It follows that the P-value > 0.05, and that the hypothesis, that the LN distribution describes the observed frequencies, can be accepted. Note also that the average size of

the AuNPs, determined from the formula $\mu\exp[\ln^2(\sigma)/2]$, is 7.89 nm and agrees fairly well with R_p obtained directly from the SEM images (7.51 nm).

4.3.4 Evolution of the AuNP coating during the plasma treatment

The growth of the AuNPs during the plasma cleaning can occur through two different mechanisms: First, the growth can be caused by migration of single Au atoms between the particles. This process is often referred to as the Oswald Ripening (OR).[117,118] During OR the diffusion-mediated mass transport of atoms allows for the growth of large particles at the expense of small ones. The OR mechanism governs thermal sintering processes of metal clusters,[119,120,121] and coarsening of Ag/Ag(111) and Cu/Cu(111) adatom islands.[122] Second, the growth of the AuNPs can occur when the particles are free to move on the substrate surface and undergo collisions that lead to coalescence. This second process is expected to be operative for small clusters that exhibit the ability to move on a substrate.[121,123,124] This process is also referred to as Smoluchowski Ripening (SR) because of the long-established Smoluchowski coagulation rate equation.[125] The SR mechanism governs, for instance, the growth of Ag/Ag(100) and Cu/Cu(100) islands.[126,127] Both SR and OR processes have recently been reported[121] to be involved in the sintering of metal clusters. In the following, I discuss theoretical predictions of both OR and SR models and compare them with experimental data.

Smoluchowski Ripening

Denote the surface density of the droplets of mass m as $n_m(t)$. Assuming that the coarsening occurs only through collisions between pairs of the NPs, the evolution of $n_m(t)$ is governed by the following Smoluchowski coagulation rate equation:[125]

$$\frac{d}{dt}n_m(t) = \frac{1}{2}\sum_{m'} k(m, m\text{-}m')\, n_{m'}(t) n_{m\text{-}m'}(t) - n_m(t)\sum_{m'} k(m, m')\, n_{m'}(t) \qquad (22)$$

where $k(m, m')$ denotes the rate constant of collisions between two droplets of masses m and m'. Assuming that the diffusing droplets are spatially uncorrelated, in 2D the rate constant is given by the relation[128]

$$k(m, m') = D(m) + D(m'), \qquad (23)$$

where $D(m)$ is the diffusion coefficient of the droplet of mass m. In Smoluchowski's model of coagulation, it is assumed that the diffusion coefficient is related to the mass of the droplet by

$$D(m) = D^{*} m^{-\alpha} , \tag{24}$$

where D^{*} is a temperature-dependent prefactor, and α is an exponent that depends on the specific mechanism governing the movement of the droplets. So far, the scaling relationship given by eq. (24) has been investigated only for the diffusion of flat (2D) clusters composed of atoms adsorbed on a solid surface. Theoretical studies based on the mean-field approach have predicted[129] values of the exponent α = 1/2, 1, and 3/2 for, respectively, the "evaporation condensation", "terrace coarsening", and the "perimeter diffusion" mechanisms of the cluster movement. Experimentally determined values of the exponent alpha have been reported in the range $0 < \alpha < 2$.[126,127,130,131] To date, there is however no theoretical model predicting the scaling relationship for nano-sized droplets performing diffusive motion on a solid substrate. I will show that predictions of the SR model fit the experimental data well, and provide – for the first time – estimation of the exponent α.

The Smoluchowski rate equation can be transformed into an equation for the evolution of the average droplet density,[125] $n_{\mathrm{av}}(t)$,

$$\frac{d}{dt} n_{\mathrm{av}}(t) = -n_{\mathrm{av}}^{2}(t) D_{\mathrm{av}} , \tag{25}$$

where $n_{\mathrm{av}} = \sum_{m} n_{m}$, and $D_{\mathrm{av}} = \sum_{\mathrm{m}} D(m)\, n_{m}/n_{\mathrm{av}}$ are, respectively, the average density and the average diffusion coefficient of the droplets. Making use of the fact that mass is proportional to the volume of the droplet, and that the total mass of the AuNP deposit is conserved, *viz.*

$$n_{\mathrm{av}}^{0} V_{\mathrm{av}}^{0} = n_{\mathrm{av}} V_{\mathrm{av}} , \tag{26}$$

where n_{av}^0 is the average droplet density before the plasma treatment, under the assumption that $D_{av} \approx D(n_{av})$, the scaling relation (24) is transformed into the form

$$D_{av} = D^* \left(\frac{V_{av}}{V_{av}^0}\right)^{-\alpha} = D^* \left(\frac{n_{av}^0}{n_{av}}\right)^{-\alpha}. \quad (27)$$

By combining eq. (26) and (27) one gets

$$\frac{d}{dt} n_{av} = -n_{av}^2 \left(\frac{n_{av}}{n_{av}^0}\right)^{\alpha} D^*. \quad (28)$$

Integration of eq. (28) yields the following equation for the evolution of the surface droplet density:

$$n_{av}(t) = n_{av}^0 \left[1+(1+\alpha) D^* n_{av}^0 t\right]^{-\beta} \text{ with } \beta = \frac{1}{1+\alpha}. \quad (29)$$

To check whether the morphology of the AuNP deposit changes in accord with predictions of eq. (29), I determined experimentally the surface droplet density for five exposition times, t = 0, 15, 30, 120, and 360 s. The data are shown in Figure 36. Fitting of eq. (29) to the experimental data provided the exponent α = 2.59 ± 0.12. This value is slightly larger than the values of α reported[126,127,130,131] for flat clusters ($0 < \alpha < 2$) comprising 10^1 - 10^2 adatoms. This result is not surprising because the mechanism underlying movement of the nano-sized droplets composed of ~10^4 – 10^5 atoms is expected to be different. The fitting procedure also allowed estimation of the prefactor $D^* \sim 2 \cdot 10^{-12}$ cm^2/s. This value corresponds to the diffusivity of the AuNPs of the diameter ~5 nm.

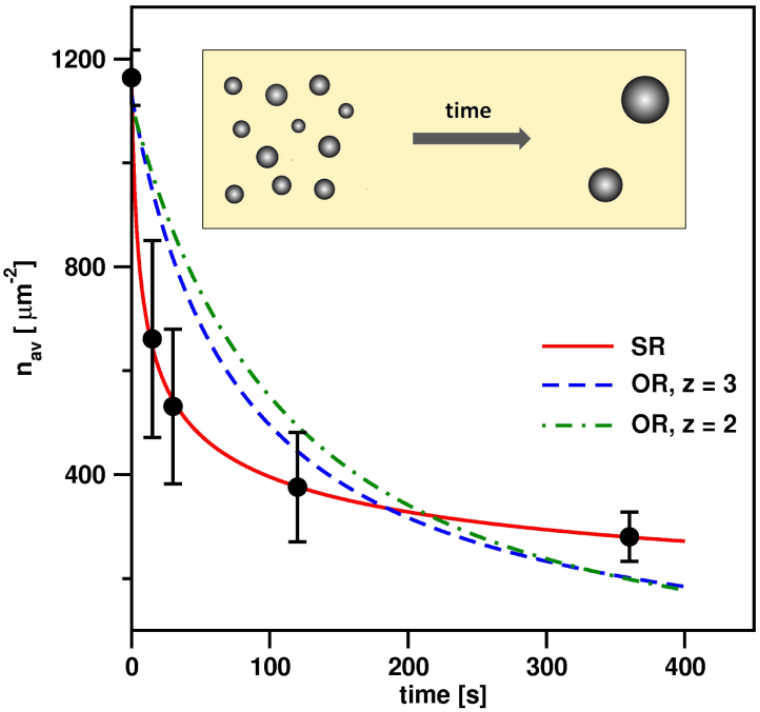

Figure 36 Number of AuNPs after plasma treatment as a function of the time of the process.

To discuss the AuNP diffusion mechanism, it is worth noting that the temperature of the silicon plate during the plasma treatment was close to room temperature. The plate's temperature was determined immediately after its removal from the plasma cleaner chamber. The obtained value of the diffusion coefficient is of the same order of magnitude as that of Pt/Al_2O_3 clusters of the size ~3.5 nm in 600°C,[124] and that of Au atoms on mica in temperature range 300˚C – 500˚C.[120] It is also several orders of magnitude larger than those measured[127,130] for small adatom clusters at room temperature (10^{-18} – 10^{-15} cm^2/s). From the above comparison it follows that the obtained diffusion coefficient of AuNPs is too large to result from a thermal Brownian motion. Thus, it is likely that the diffusion of the AuNPs during the plasma treatment is not a thermal-induced process occurring in thermodynamic equilibrium, but another mechanism is operative. During the plasma treatment, the AuNPs are bombarded with both high-energy ions and uncharged molecules. These objects immediately remove the organic coating from the AuNPs core. Then, upon collisions, transfer part of their kinetic energy to the surface atoms of the AuNPs. This can lead to the liquefaction of the AuNP (or of its surface layer in the case of a large NP). Most probably, also diffusion of the AuNPs on the surface is enhanced by collisions with high energy particles of plasma through the mechanism similar to that in ion- and electron-irradiation[132] induced growth of metal nanoclusters.

Ostwald Ripening

When OR is the dominant growth mechanism the average radius of the droplet, $<R_{pt}>$, follows the relation[118]

$$<R_{pt}>^{z} - <R_0>^{z} = ct, \tag{30}$$

where $<R_0>$ denotes the average radius of the NPs in the bulk solution, c is a constant, and z is an exponent. The value of z depends on the specific mechanism of the mass transport. For three-dimensional growth of clusters on a solid substrate one expects[118,120] $2 < z < 3$. Making use of the total mass conservation condition given by relation (26), and assuming that the droplet volume is proportional to the third power of its radius, one gets

$$n_{av}(t) = n_{av}^{0}\left[1+cR_0^{-\square}t\right]^{-3/z}. \tag{31}$$

Interestingly, note that the SR and OR model predict essentially similar functional dependence of the surface droplet density on time. Formulas (29) and (31) become identical for $\alpha = z/3 - 1$. Fits of eq. (31) to the experimental data obtained for $z = 2$ and $z = 3$ are shown in Figure 36.

4.3.5 Smoluchowski Ripening as the dominating mechanism

Results presented in Figure 36 lead to the conclusion that the coarsening of the AuNPs is dominated by the diffusion-coalescence mechanism. The formula for $n_{av}(t)$ derived from the SR model fits the experimental data significantly better than that predicted by OR. What is important, the fit of eq. (29) gives a reasonable value of the diffusivity of the droplets similar to that reported in literature.[124] Also, the obtained value of the exponent α indicates that the diffusion coefficient is decreasing rapidly with the size of the particle, which is in line with experimental observations.[124] These facts show that the SR model provides a reliable description of the coarsening process.

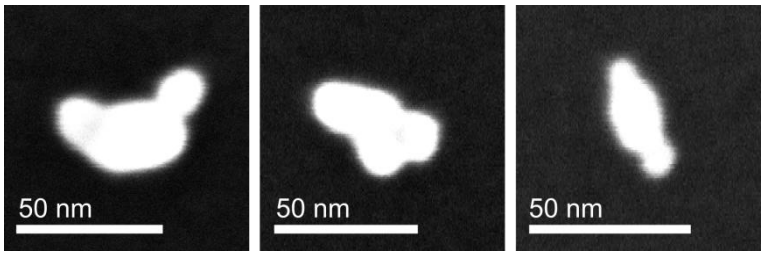

Figure 37 SEM images of the partially fused AuNPs present on the low-coated surface.

The second argument in favour of the SR mechanism follows from the analysis of the droplet morphology. Namely, the observed significant increase of the contact angle, from 54 to 123 degrees, suggests that during the plasma treatment outer portions of the AuNPs are melting, and their final shapes result to a great extent from minimization of the surface energy. Such transition into a liquid state can enable the AuNPs to move on the surface and coalesce upon collision. As can be seen in the SEM image of the high-density coating (Figure 33b), after the plasma treatment the majority of the droplets possess complex, irregular shapes. Most probably, such morphology results from partial fusion of the neighbouring AuNPs, accompanied by breakage of the initial network-like structure. Note that similar structures composed of partially fused droplets, displaying sharp cusps, were observed also in the low-density coating (see Figure 37). It is rather unlikely that the OR process, which eliminates highly curved surfaces, could produce the structures observed after the plasma treatment.

It has recently been argued[119,121] that the mechanism governing the cluster growth cannot be determined solely from the particle size distribution. Nevertheless, its form can be a source of information about possible processes involved in the coarsening. When OR is the dominant growth mechanism, then asymmetric size distributions with negative skewness are observed.[117,118,133] On the other hand, coalescence-induced growth results in an asymmetric size distribution with positive skewness. The LN distribution of the final particle sizes can then be observed.[133] Thus, the LN distribution of the projected radii I found, combined with the results on the growth kinetics shown in Figure 36, provides an additional argument that the coarsening is dominated by the SR mechanism.

4.3.6 Conclusions

In this section the changes in the morphology of the AuNPs caused by oxygen plasma treatment were investigated. I found that plasma treatment affects the

morphology of the AuNPs in two ways. First, it makes them coarsen. Second, it also changes the shapes of individual particles. Specifically, I found that their initially flattened shapes become more spherical, resembling droplets of a non-wetting liquid, and their contact angles increase from 54 degrees to about 123 degrees. I provided arguments that the growth of the AuNPs during the plasma treatment is dominated by the diffusion-collision mechanism. These results indicate that during the plasma treatment the particles exhibit a liquid-like behavior, with the ability to move on the substrate surface and coalesce. To model the time evolution of the surface density of the droplets, I employed the mean-field Smoluchowski coagulation rate equation, and assumed the diffusivity of the droplet scales with its mass as $D(m) \sim m^{-\alpha}$. I found that the experimental data are in accord with the predictions of the Smoluchowski model. Analysis of the droplet density evolution data provided, to my best knowledge, for the first time, an estimate of the scaling exponent of $\alpha = 2.6$.

4.4 Growth of AuNPs deposited on solid substrates

4.4.1 Introduction

The growth of immobilized NPs is a way of fabricating surfaces of more dense (or thicker) gold coverage, frequently built of non-spherical objects. In this section I characterize the autocatalytic properties of AuNPs formed during the plasma treatment by applying them as seeds for the further growth of gold particles. The seed-mediated growth of AuNPs can be carried out using a variety of growth solutions that are based on different reducing agents. Sample reducing agents are amines,[83,134,135] polymers,[136] or hydroquinone.[137] Most of the reducing agents, in addition to the autocatalytic growth, also give rise to bulk nucleation. In my studies I investigated compounds that are supposed to reduce gold ions on the surface of the seeds without causing bulk nucleation. Based on the literature reports I referred to above and in the following sub-sections, I selected three reducing agents: hydroxylamine hydrochloride ($NH_2OH{\cdot}HCl$), ascorbic acid (AA), and 2-mercaptosuccinid acid (MSA). For each reducing agent, the autocatalytic properties of the AuNPs formed during the plasma treatment were characterized in terms of the morphology of the grown nano-structures.

4.4.2 Preparation and analysis of samples

Three-step AuNP growth protocol

The procedure I followed to grow AuNPs on a silicon substrate is outlined in Figure 38. In the first step (i), AuNPs (~5 nm in diameter) coated with a positively charged ligand (TMA) were adsorbed on a silicon plate with the ionic strength-controlled deposition method.[84] The use of this method facilitated obtaining coatings of prescribed density. In the experiments presented here I investigated two types of AuNP coatings: low-and high-density ones. In the second step (ii), to remove the thiol protecting layer from the AuNPs deposited, the plate was purified by cleaning in oxygen plasma. The plasma treatment resulted also in a coarsening of the AuNPs on the surface of the plate. These AuNPs served as seeds for the subsequent growth of gold nanostructures conducted in the third step (iii). The plate was immersed in a growth solution containing chloroauric acid and reducing and capping agents.

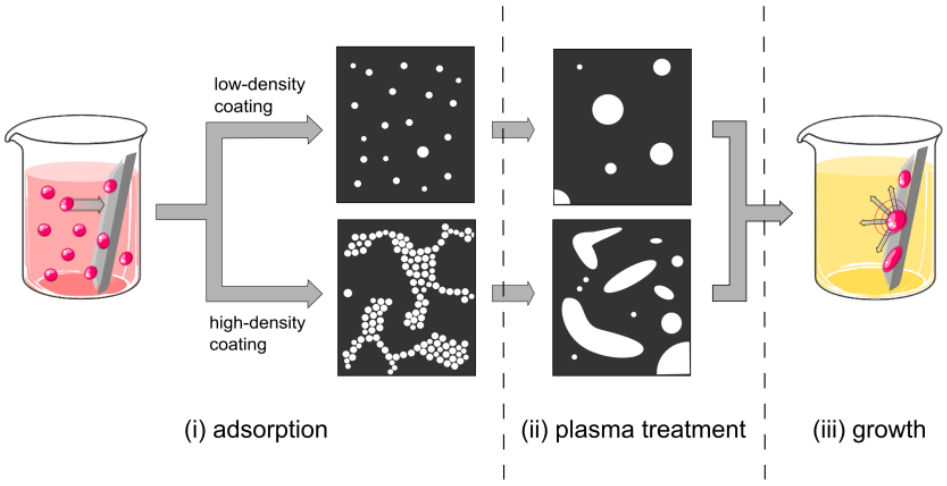

Figure 38 Schematic representation of the three-step procedure: a) A silicon plate is coated with AuNPs by the ionic strength-controlled deposition method.[84] Two types of coatings: low- and high-density are obtained. b) The plate is subjected to plasma cleaning. All organic compounds are removed and the AuNPs coalesce. c) The plate is immersed in a growth solution containing chloroauric acid, a reducing agent, and additional reagents.

Materials

Besides the materials mentioned in the Experimental section, three types of poly(vinylpyrrolidone): PVP-k10 ($M_w \approx 10{,}000$), PVP-k25 ($M_w \approx 29{,}000$), and PVP-k30 ($M_w \approx 55{,}000$), purchased from Sigma-Aldrich were used.

Preparation of AuNPs

AuNPs were synthesized according to the procedure of Jana and Peng.[83] The obtained AuNPs had an average radius of (2.5 ± 0.43) nm, as determined from the SAXS spectrum of the AuNP solution. To provide a positive charge on the NPs, their hydrophobic amine ligands were replaced with TMA. The purified and dried AuNPs were finally dispersed in deionized water, yielding a 0.6 mg/mL gold solution.

Deposition of AuNPs onto a silicon substrate: low- and high-density coatings

AuNPs were deposited onto the silicon according to the procedure described previously.[84] The exact procedure is described in the Experimental section.

Growth of the AuNPs on a silicon substrate

Prior to the growth process, the plate was cleaned using oxygen plasma (29.6 W, 6 min. treatment). Under these conditions, all organic compounds and products of their oxidation were completely removed from the AuNP surface. Next, the purified plate was immersed in a growth solution. All growth reactions were carried out at room temperature. After the growth process was finished, the plate was carefully washed, consecutively, with water and ethanol, and dried. In my experiments the following growth solutions, based on three different reducing agents, were employed:

$NH_2OH{\cdot}HCl$: To an aqueous solution of hydroxylamine hydrochloride, an aqueous solution of $HAuCl_4{\cdot}3H_2O$ was added dropwise while stirring. Growth time: 72 h.

AA: Aqueous solutions of PVP k-30, cetyltrimethylammonium bromide (CTAB), and AA were mixed. Then a solution of $HAuCl_4{\cdot}3H_2O$ was added dropwise while stirring. Growth time: 10 min.

MSA: A solution of $HAuCl_4{\cdot}3H_2O$ was added dropwise to an aqueous solution of MSA while stirring. Growth time: 24 h.

Morphological characterization of the coating

Morphological analysis was based on the SEM images. Shapes of individual particles in the image were identified, and their projected areas and radii were determined and collected. The distributions of sizes/shapes were calculated for about 100 objects. The percentage surface coverage, θ, was the ratio of the sum of the projected areas of all objects to the area of the image analyzed. The polydispersity, p, was calculated as the ratio of the standard deviation of the sizes to the mean size, and was expressed as percentage. The aspect ratio, r, was calculated as the ratio of the major to minor axis of the particle. In the case of elongated particles, having an ellipsoidal projection, the radius was calculated as the geometric mean of their two semi-axes.

Instrumentation

The plates covered with AuNPs were purified in oxygen plasma with Harrick Plasma Cleaner PDC-002.

4.4.3 Seed-mediated growth of the AuNPs on a silicon substrate

The AuNPs formed during the plasma cleaning are further investigated by examining their properties as seeds for growth of the AuNPs. I carried out these studies using the growth protocol shown in Figure 38 for three commonly used reducing agents: hydroxylamine hydrochloride, AA, and MSA. Different mechanisms of the Au(III) reduction, combined with the effects of the capping agents, led to the growth of AuNPs of various morphologies. The observed shapes of these particles were grouped into five classes that are shown in Figure 39: (1) ellipsoid-like particles, (2) rods, (3) triangular plates (including equilateral triangles, truncated triangles, and triangles with rounded vertices), (4) hexagonal plates, and (5) spherical-like particles (including polyhedral shapes: vertex-truncated icosahedra and octahedra). For the sake of simplicity, I refer to the ellipsoidal- and spherical-like AuNPs as 3D structures, and to the rods and plates as 1D and 2D structures, respectively. All histograms of the sizes/shapes were determined

only for the low-density coatings because for the high-density ones identification of individual AuNPs was often problematic. In the following, results of the morphological analysis performed for the three reducing agents are presented.

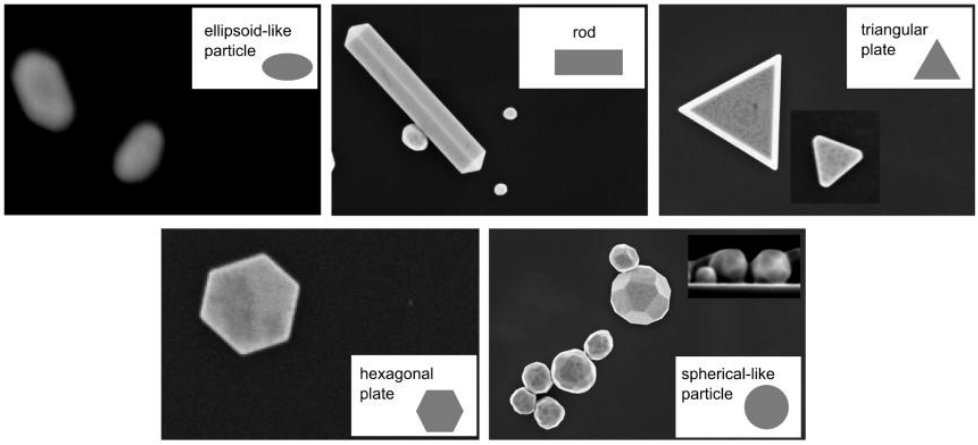

Figure 39 SEM images showing five types of the particle shapes observed after the growth process.

4.4.3.1 Hydroxylamine

Typical growth mixtures based on this reducing agent are aqueous solutions of $NH_2OH{\cdot}HCl$ and $HAuCl_4$, and can be used to grow both AuNPs suspended in the bulk solutions[138,139] as well as AuNPs attached to a substrate[138,140,141,142]. According to the literature cited, hydroxylamine promotes the growth of spherical particles of small polydispersity, and does not give rise to a nucleation. It is noted that my studies are the first to show systematically the growth of AuNPs for different hydroxylamine concentrations and the $[NH_2OH]$:$[HAuCl_4]$ molar ratios, for a long reaction time (3 days instead of the 3-30 min. reported in literature).

Typically, a growth solution based on $NH_2OH{\cdot}HCl$ and $HAuCl_4$ contains the reactants in concentrations of $\sim 10^{-4}$ M.[138,139,140,141,142] To be comparable with the previous works, I investigated the growth process for solutions containing $NH_2OH{\cdot}HCl$ in four concentrations: 0.05, 0.2, 0.35, and 0.5 mM. For each concentration of hydroxylamine used, four $[NH_2OH]$:$[HAuCl_4]$ molar ratios: 8:3, 8:4, 8:5, 8:6, and 8:7 were prepared, totaling 20 different growth solutions. Results obtained for four extreme reagent concentrations are shown in Figure 40. As seen in this figure, all types of AuNPs were obtained, but the 3D structures dominated for each growth solution used. The majority of the spherical-like particles displayed well-formed crystallographic facets, and possessed shapes of truncated icosahedra. The rod-like particles had pentagonal

and octagonal cross-sections. I observed a strong dependence of the distribution of AuNP shapes on the reaction mixture composition. The most remarkable feature of the data presented in Figure 40 is the decrease of the fraction of the spherical-like AuNPs with increasing concentrations of the reagents, and decreasing of the reagent ratio. Evidently, higher concentrations of reagents and lower $[NH_2OH]$:$[HAuCl_4]$ reagent ratios promoted formation of the 1D and 2D objects. As seen in Figure 40, for the reagent ratio 8:3, formation of the nano-plates did not take place at all. The 1D and 2D structures were formed only for $[NH_2OH]$:$[HAuCl_4]$ ratios less than 8:5. For 0.5 mM NH_2OH and the reagent ratio 8:7, the anisotropic AuNPs accounted for 30.5% of all particles, of which 57.5% were nano-rods. However, for sufficiently high reagent concentrations the growth of the 1D and 2D particles was almost completely suppressed, even for the 8:7 $[NH_2OH]$:$[HAuCl_4]$ ratio.

For each of the 20 solutions examined, a noticeable reduction of the initial size polydispersity (p > 80%) was observed. For some compositions of the growth solution the values of p dropped even below 35%, as seen in Figure 40.

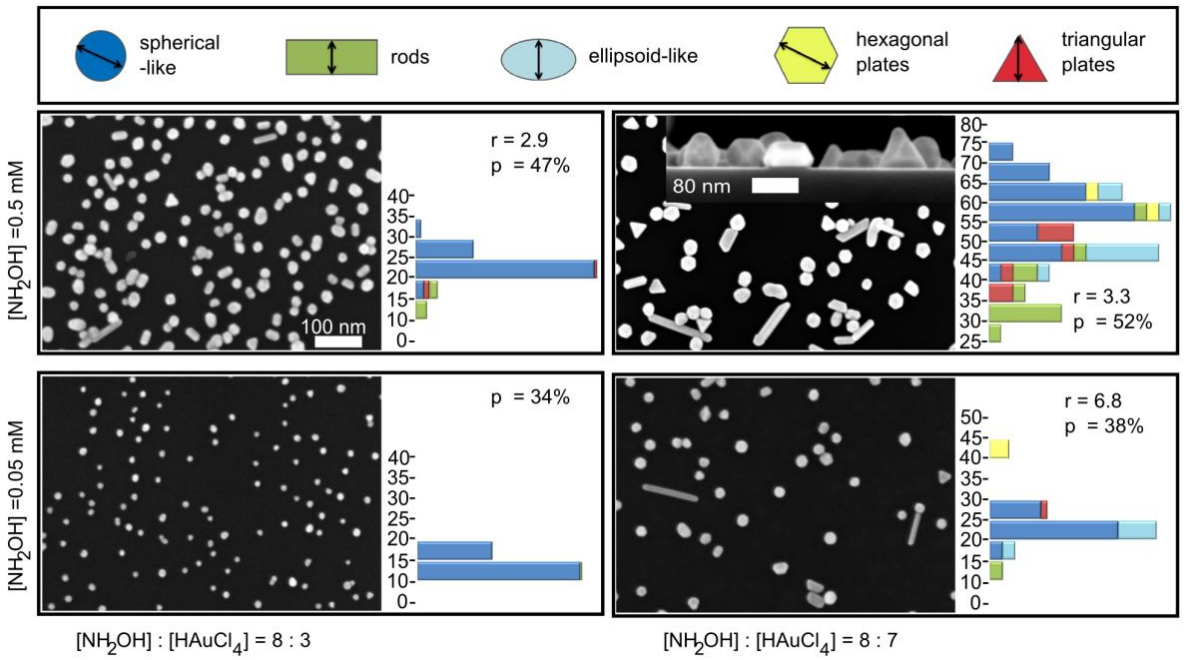

Figure 40 SEM images of the grown AuNPs, particle size distributions, values of the polydispersity, *p*, and the aspect ratio, *r*, obtained for the hydroxylamine-based growth solutions (low-density coating). The aspect ratios characterize the rod-like objects only. Results for four extreme reagent concentrations are shown. Definitions of the sizes for the AuNP shapes considered in the distributions are given at the top. The values on the histograms are expressed in nanometers. Magnification for the four main SEM images is the same. The inset SEM image shows a representative side-view of the grown AuNPs; scale bar is 80 nm.

For the low- and high-density coatings I obtained quite similar dependencies of the distributions of the AuNP shapes on the composition of the growth solution. The only difference observed was, that for high-density coatings the particles had generally more rounded edges and vertices.

4.4.3.2 Ascorbic acid

This reducing agent is frequently used in the seed-mediated growth processes of AuNPs. It is utilized mainly in the synthesis of nanorods, typically in the presence of a rod-like micellar template – cetyltrimethylammonium bromide (CTAB). This reduction is a two-step process that begins with the formation of a complex of Au(III) ions and surfactant molecule. The method requires at least a 3:2 [AA]:[$HAuCl_4$] molar ratio, and the first equivalent of ascorbic acid is consumed for Au(III) to Au(I) reduction.[143] The addition of AuNPs causes a further reduction of gold and the growth of anisotropic clusters. In order to accelerate the process, one can raise the pH value of the reaction mixture to 8-10. Under these conditions the production of ascorbate ions, which possess greater reducing ability than AA,[144] occurs. The CTAB-Au(III) complex is used in the seed-mediated formation of nanorods and nanowires, both in solutions[145] and on solid substrates[146,147,148]. The addition of poly(vinylpyrrolidone) (PVP) may lead, however, to the formation of 2D structures.[149] PVP can act both as a reducing and protecting agent, but in the presence of AA its capping function is enhanced. AA promotes 2D crystal growth, resulting in the formation of thin nanoplates (mainly triangles), and, in the presence of CTAB, does not lead to nucleation.[149]

To investigate AA as a reducing agent, aqueous solutions of AA and $HAuCl_4$ were used. To suppress bulk nucleation, CTAB and PVP were added to the growth solutions. I found that among PVP-k10, PVP-k25, and PVP-k30, the best stability against nucleation was provided by PVP-k30. For the mixtures used in my experiments, the nucleation did not occur for at least 1 h after preparation. The effect of the composition of the AA-based mixtures was examined for fixed concentrations of $HAuCl_4$ (0.24 mM) and AA (0.48 mM). I investigated the growth processes for CTAB and PVP concentrations similar to those studied by Umar *et al.*[149] I examined 16 different growth mixtures that were obtained by combining four CTAB (15, 25, 35, and 45 mM) and four PVP (0.3, 0.5, 0.7, and 0.9 mM) concentrations. It was found that the final distribution of the AuNP shapes was established after ~10 min of the growing process. For longer growth times (45 and 60 min.) only an overall small increase in the size of the AuNPs was observed. SEM images

of the coatings (growth time 10 min) obtained for four extreme concentrations of the reagents, along with the NP size distributions are shown in Figure 41. For all AA-based growth solutions used, formation of 1D, 2D, and 3D objects was observed, but spherical-like particles occurred most frequently. It was found that the morphology of the AuNPs hardly depended on the CTAB and PVP concentration in the mixture. Moreover, the average aspect ratio (r) of the rod-like AuNPs varied with the CTAB and PVP content in the solution. For the lowest and the highest concentrations of these reagents, rods with, respectively, r = 3.0 and r = 2.6 were formed. For all growth solutions, the polydispersity of the coatings was reduced. For a fixed concentration of CTAB, values of p slightly increased with the increase of the PVP content. Interestingly, note that there was a difference in the morphology of the grown AuNPs between the low- and high-density coatings. In the latter case, for every growth solution used, mainly spherical and ellipsoidal shapes (with $1.1 < r < 1.8$) were formed, and the 1D and 2D structures occurred occasionally.

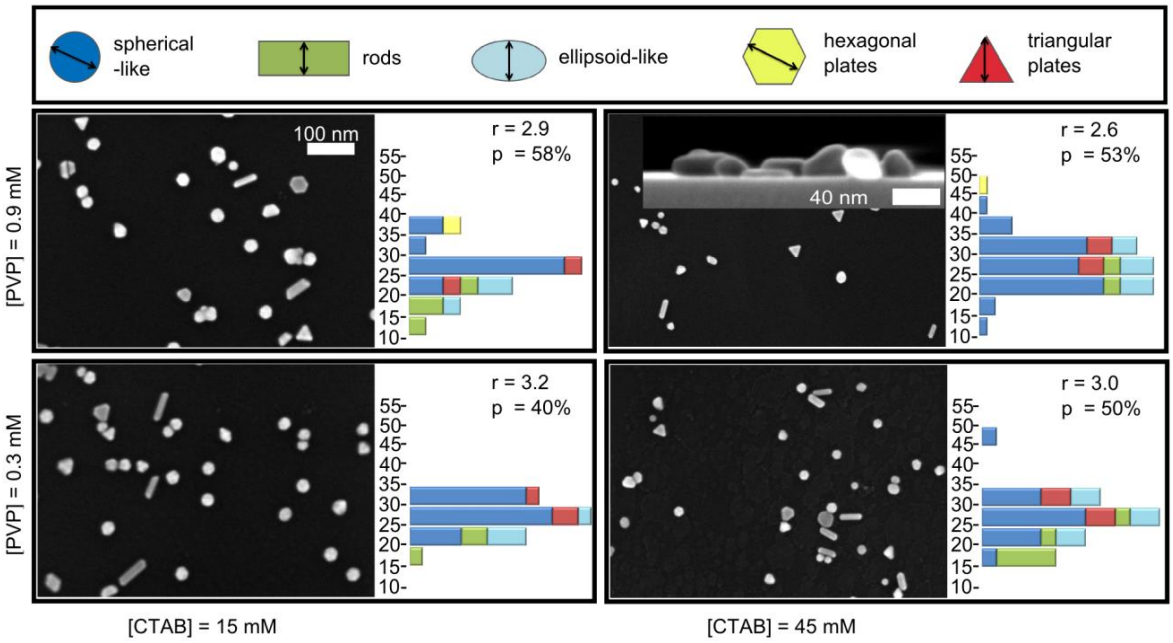

Figure 41 The same as in Figure 40, but for AA-based growth solutions.

Umar *et al.*[149] applied similar AA-based growth solutions, containing CTAB and PVP, to grow nanoseeds deposited on indium tin oxide (ITO), and cleaned by heating at 250°C for at least 60 min. The most important difference between the present results and those reported by the authors cited concerns about the proportion of the spherical-like and 2D objects formed. In Ref. 149, a big fraction (50% – 70%) of the nanoplates was obtained, whereas in all my experiments 2D objects occurred rarely (less than

13%). It is known[150] that the morphology of the grown AuNPs is, to a great extent, determined by the type and number of crystallographic defects present in the seeds. In particular, planar defects such as stacking faults are believed[150] to promote the growth of hexagonal and triangular plates. Thus, the experimental data suggests that the plasma cleaning – in contrary to the heat treatment – results in the formation of AuNPs that are substantially free from the stacking defects.

4.4.3.3 2-Mercaptosuccinid acid

This reducing agent is still a relatively new reagent used in AuNP synthesis. Its primary function is stabilization of the AuNPs during the synthesis.[151] Due to a mercapto functional group and its ability to form an Au-S bond with the AuNP surface, MSA is also an excellent capping agent (stronger than citrate[152]). Because of dissociable carboxylic moieties, it provides electrostatic repulsions in gold colloids, preventing aggregation of the AuNPs. Also, as a dicarboxylic compound, MSA can be employed as a reducer. Niu *et al*.[153] applied MSA for the first time both as a capping and reducing agent. In an aqueous solution MSA promotes isotropic growth of AuNPs and leads to the formation of nearly spherical NPs. My work is – to my best knowledge – the first one demonstrating the use of MSA as a capping and reducing agent in the seed-mediated growth of the AuNPs deposited on a substrate.

The growth reactions for four [MSA]:[$HAuCl_4$] molar ratios, 0.75:10, 1.5:10, 3:10, and 6:10, were carried out. Each of the four reaction solutions was applied for four different concentrations of $HAuCl_4$ (7.25, 14.5, 21.75, and 29 μM), both for low- and high-density coatings. It was found that the morphology of the grown AuNPs did not depend on the initial density of the seeds. Figure 42 shows representative results obtained for the low-density coating for four extreme growth mixture compositions. As seen, for each growth mixture employed, mostly spherical-like objects were formed. The most regular shapes – spherical AuNPs – were obtained for [MSA]:[$HAuCl_4$] = 6:10 and the highest reagent concentration. A high excess of $HAuCl_4$ ([MSA]:[$HAuCl_4$] = 0.75:10) resulted in the formation of ~10% of non-spherical particles: equilateral triangles and ellipsoids ($1.5 < r < 2.3$). Most probably, formation of these objects was due to the small amount of MSA, which acts as a capping and protecting agent.[153] At a low MSA concentration, selective adsorption of Au(III) on different facets occurs, and the seeds can be transformed into non-spherical shapes. Remarkably, for [MSA]:[$HAuCl_4$] = 0.75:10 and high $HAuCl_4$ content (21.75 and 29 μM), a significant fraction of small (<10

nm) AuNPs were present after the growth reaction. It is not clear yet whether in these conditions the growth of the smallest seeds was retarded or the nucleation process took place. Based on the UV-Vis spectroscopy measurements, I found however that bulk nucleation did not occur for any of the MSA-based growth solutions used. Formation of the nuclei was observed only for sufficiently high $HAuCl_4$ concentrations (>145 μM), exceeding ~10 times those employed in my experiments.

For all MSA-based growth solutions, a substantial reduction of the AuNPs size polydispersity was observed. The values of *p* decreased from ~80% to ~40% (Figure 42). This means that MSA, as a reducing agent, can be used to improve the uniformity of the sizes of the AuNPs deposited on a silicon substrate.

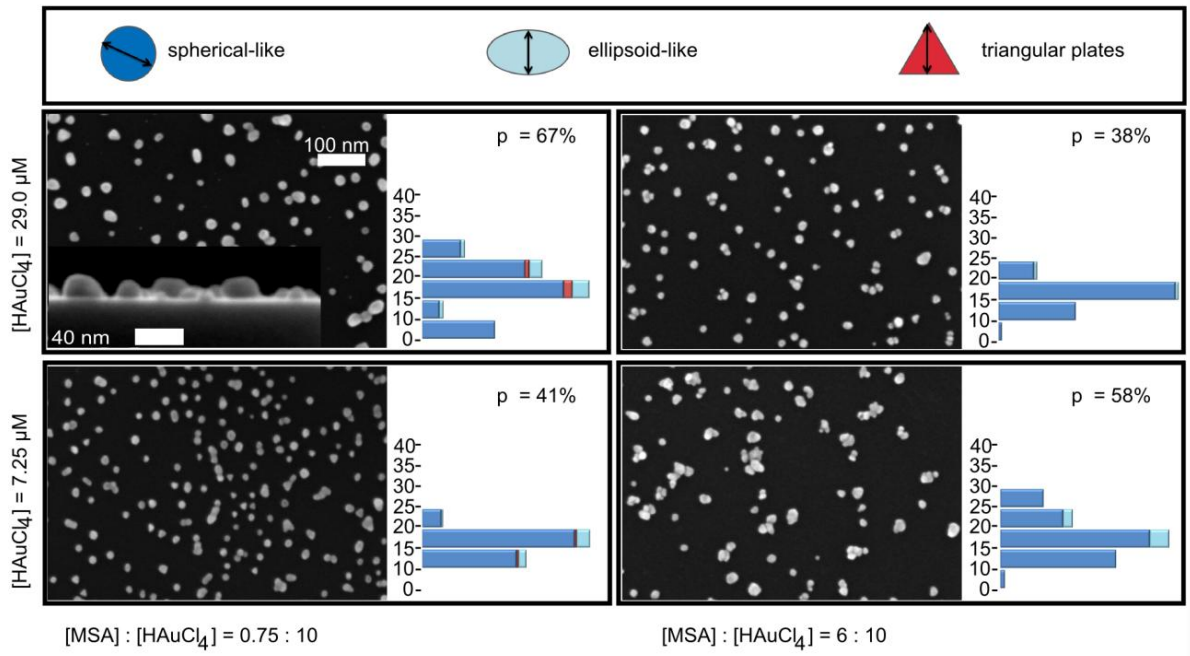

Figure 42 The same as in Figure 40, but for MSA-based growth solutions.

4.4.4 Conclusions

In the present section the autocatalytic properties of AuNP coatings formed during the plasma treatment were examined in detail by employing them as seeds for the further growth of gold particles. Systematic experiments were carried out for growth solutions based on three reducing agents: $NH_2OH{\cdot}HCl$, AA, and MSA. I found that the final morphology of the grown AuNP coating hardly depends on the initial density of the seeds. Depending on the composition of the growth mixture used, various proportions of the polyhedral, spherical-, plate-, and rod-like particles can be obtained in the resulting coating. It was found that, out of the three studied reducing agents, hydroxylamine offers

the greatest variety and the best control over the final shapes of the AuNPs. It was found, however, that – for each reducing agent used – the formation of spherical-like and polyhedral structures was favored. For each growing mixture a significant reduction of the size polydispersity was also observed. This study is the first to investigate systematically the growth of AuNPs for different hydroxylamine concentrations and $[NH_2OH{\cdot}HCl]$:$[HAuCl_4]$ molar ratios. To my best knowledge, the present description is also the first to demonstrate the seed-mediated growth of AuNPs on a surface in the presence of MSA. The results presented can help in the choice of the proper composition of the growth mixture, which allows obtaining AuNP coatings of desired morphology. Moreover, the experiments described here led to the interesting finding that plasma cleaning results in the formation of AuNPs that are substantially free of stacking defects.

4.5 Gold microflowers

4.5.1 Introduction

Noble metal nano- and microstructures of non-spherical shapes have received much attention in recent years.[154,155,156,157,158] Their morphological forms – including flower-, rod-, wire-, and plate-like structures – exhibit unusual optical,[159] electronic,[160] and catalytic[161,162] properties. One very promising area of applications of gold nano- and micro-flowers is SERS. Surfaces modified with such flower-like structures have proved[163,164,165,166,167] to provide large SERS enhancement factors. Known methods[154,159,161-168,169-175] for synthesizing gold micro-flowers (AuMFs) require fairly elaborate techniques. In these methods, AuMFs are typically synthesized in reaction solutions containing gold salts, reducing agents, buffers, and additional reagents that strongly affect both the size and the morphology of the resulting structures. For instance, reagents like polianiline,[154] chitosan,[170,171] surfactants[172,173] or DNA[174] have been utilized to obtain gold particles of ragged, flower-like shapes. Similar structures have also recently been fabricated mechanically by a centrifuging process.[175] Against the background of the abovementioned methods, the procedure for fabricating AuMFs described below is distinguished by its simplicity. Using only water solutions of auric acid ($HAuCl_4$) and hydroxylamine hydrochloride ($NH_2OH{\cdot}HCl$), one can obtain AuMFs whose number, size, and shape strongly depend on the concentration and molar ratio of the solutions used. AuMFs deposited on a solid substrate form a mechanically stable gold layer of expanded nano-structured surface. Such nano-structured metallic layers are employed as efficient platforms for chemical and biological sensing based on SERS.

4.5.2 Preparation and analysis of samples

Preparation of the reaction mixture and nomenclature used in this section

To prepare the reaction mixture, a solution of auric acid was added dropwise while shaking to an aqueous solution of hydroxylamine hydrochloride. The resulting reaction mixture was fully characterized by the $HAuCl_4$:$NH_2OH{\cdot}HCl$ molar ratio and the concentration of hydroxylamine chloride. In this work, the mixture concentration is given relative to the reference solution, *c*1, containing 0.5 mM of $NH_2OH{\cdot}HCl$. For example, to obtain the *c*1 (3:8) reaction mixture containing 3:8 $HAuCl_4$:$NH_2OH{\cdot}HCl$ molar ratio, one volume of 0.8 mM $NH_2OH{\cdot}HCl$ with 0.6 volume of 0.5 mM $HAuCl_4$ were mixed. Mixtures diluted ten times are marked – irrespectively of their $HAuCl_4$:

$NH_2OH{\cdot}HCl$ molar ratio – as *c*0.1. Similarly, mixtures with ten times higher concentrations of hydroxylamine are marked as *c*10, *etc*.

Analysis of samples

The absorption spectra of reaction mixtures were recorded on Ocean Optics USB 2000+ spectrophotometer in the spectral range 300-800 nm in quartz micro cuvette (10 mm of path length). The sample was illuminated with UV-VIS-NIR LIGHTSOURCE DH-2000, Ocean Optics. The absorption spectra were recorded starting from the 35th s of the reaction (35 s is the time for complete addition of $HAuCl_4$ to the $NH_2OH{\cdot}HCl$ solution and for transfer of the reaction mixture to the cuvette).

Shapes, sizes and number of AuMFs were analyzed using field emission scanning electron microscopy (FE-SEM). Usually, I analyzed AuMFs adsorbed to silicon strips. The reaction mixture was prepared according to the procedure described previously in this section. As soon as the reagents were stirred, the dried slide was placed in a vial containing this mixture for the desired time. Then, the plate was carefully washed subsequently with water and with methanol, dried, and analyzed.

4.5.3 Effect of the composition and concentration of the reaction mixture on the morphology of AuMFs

In the presented method, flower-like structures were produced by reducing the gold Au^{3+} ions with hydroxylamine hydrochloride. So far, mixtures of $HAuCl_4$ and $NH_2OH{\cdot}HCl$ have been used only in the seed-mediated growth of NPs and never in the synthesis of gold objects. Moreover, nucleation in this mixture was considered as theoretically possible but, in practice, not obtainable without the catalytic presence of the gold surface.[138,139] In section 4.5, however, such a synthesis is described.

The reaction mixture can be fully characterized by the concentration of hydroxylamine and the $HAuCl_4$:$NH_2OH{\cdot}HCl$ molar ratio. To investigate the effect of the molar ratio of reagents on the AuMF morphology, nine *c*1 reaction mixtures of a fixed concentration of hydroxylamine (0.5 mM) and different molar ratios were employed. The $HAuCl_4$:$NH_2OH{\cdot}HCl$ molar ratios ranged from 1:8 to 9:8. In each case a silicon plate was immersed for 24 h in the reaction mixture. The morphology of the AuMFs deposited on the plate was analysed using SEM. I found that, for each molar ratio used, only flower-shaped micro-structures were present. The AuMFs formed had sizes (diameters) in the range of 0.8 - 2.5 μm, and were randomly distributed on the substrate. Analysis of the SEM images revealed that for lower contents of auric acid, for ratios from 1:8 to 5:8, the

AuMFs had a hedgehog-like structure consisting of a number of small "petals" (Figure 43a and Figure 43b). AuMFs obtained for higher contents of gold ions, from 7:8 to 9:8, exhibited a less expanded morphology, with a fewer number of petals (Figure 43c and Figure 43d). In other words, a larger excess of the amine promotes more branched structures. This phenomenon may result, for example, from selective blocking by NH_2OH of certain crystallographic planes on the growing gold nucleus and, consequently, from increased growth of its other available areas. In most of the experiments described in this chapter the 3:8 molar ratio, which leads to formation of the most folded AuMFs (Figure 43), is used.

To check the effect of the concentration of reagents on the morphology of the AuMFs, I investigated mixture concentrations in the range from *c*0.05 to *c*50 for each of the molar ratios used. I found that the reagent concentration does not have any noticeable effect on AuMF morphology in a wide range of concentrations. However, for concentrations lower than *c*0.4, amorphous gold particles were formed, and the flower-like structures were not observed.

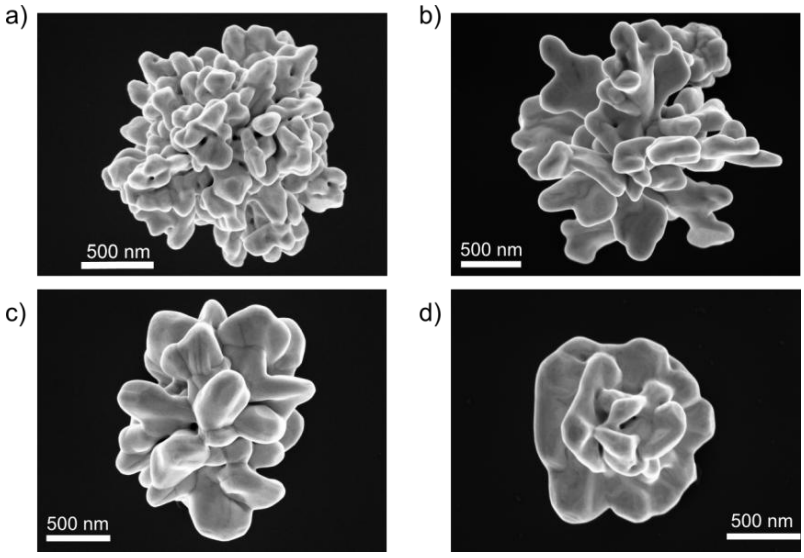

Figure 43 Effect of the $HAuCl_4$:NH_2OH·HCl molar ratio on AuMF morphology: Pictures a, b, c, and d show SEM images of typical AuMFs deposited on a silicon substrate, obtained for a *c*1 mixture with 3:8, 5:8, 7:8, and 9:8 molar ratio, respectively.

The experimental results suggest that the flower-like particles are not observed for concentrations lower than *c*0.4 because of an insufficient amount of gold ions in the reaction mixture. As I found from the analysis of the SEM images, the average number of particles created during the reaction was similar for concentrations ranging from *c*0.05-*c*1. However, the average size of the particles observed for the low concentrations was significantly smaller than that observed for $c > c0.4$. This observation indicates that in

low concentration mixtures there is not enough matter for the nuclei to grow and develop properly shaped “petals”.

4.5.4 The process of formation of the AuMFs

As it was mentioned above, the formation of metallic gold in the reaction of $HAuCl_4$ and $NH_2OH{\cdot}HCl$, without additives, has not been observed to date. On the basis of the typical oxidation of hydroxylamine and on the electron and atomic balance I propose the following reaction equation:

$$3\ NH_2OH{\cdot}HCl + 4\ HAuCl_4 + 3\ H_2O \rightarrow 3\ HNO_2 + 4\ Au^0 + 19\ HCl. \qquad (32)$$

One can notice that in the above equation a molar preponderance of the gold ions over the hydroxylamine occurs. In my procedure, however, I applied a great excess of the amine to achieve highly folded structures. In this sub-section I present a possible explanation of the observed effect of such amine excess on the morphology of the AuMFs.

The typical process of forming AuMFs consists in the mixing of two solutions – aqueous solutions of auric acid and hydroxylamine hydrochloride – at room temperature. After 24 h of the reaction, gold microparticles with a highly-folded surface (see Figure 44) are well formed. For concentrations of reagents higher than $c10$, one can see them as a rubiginous precipitate on the bottom of the reaction vessel. To analyze the product with field emission SEM, the AuMFs could be either collected after reaction and placed on a silicon plate or deposited on a solid substrate during the reaction, as was described in the “Analysis of samples” sub-section. SEM analysis showed that the presence of the silicon plate in the reaction mixture has no effect on the morphology of the product.

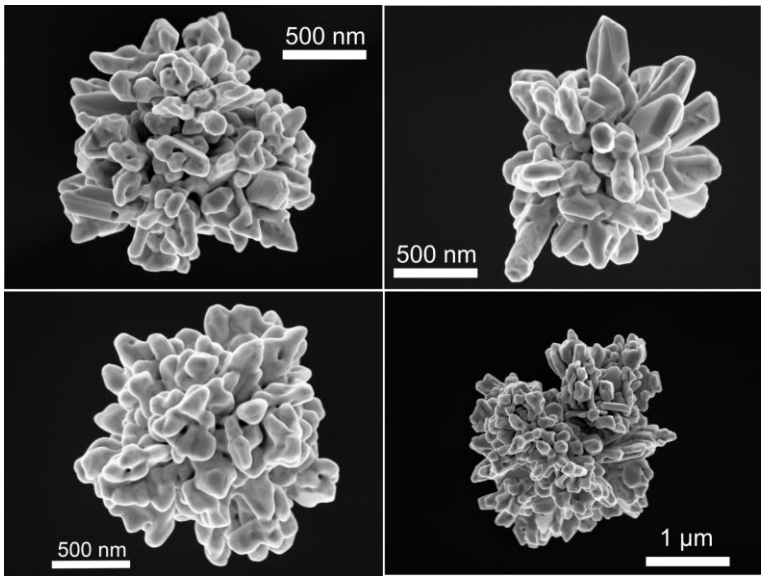

Figure 44 SEM images of typical AuMFs obtained using method described in section 4.5. These particular AuMFs were fabricated in a reaction mixture of 3:8 $HAuCl_4$:NH_2OH·HCl molar ratio and 0.5 mM concentration of NH_2OH·HCl.

In order to establish the subsequent stages of the formation of the metal product, the reactions *c*1(3:8) for various times were conducted. After mixing of the substrates (which took about 15 s), a silicon plate was immersed in the reaction mixture for a desired time (reaction times between 20 s and 72 h, including the time of mixing, were examined). Then, plates were washed, dried, and analyzed using SEM.

Analysis of the SEM images allowed me to identify five main stages of the AuMFs formation. Typical morphologies present in each stage are shown in Figure 45. Figure 46, in turn, presents the size distribution of the objects observed at the 1st, 4th, 10th, and 60th min of the reaction.

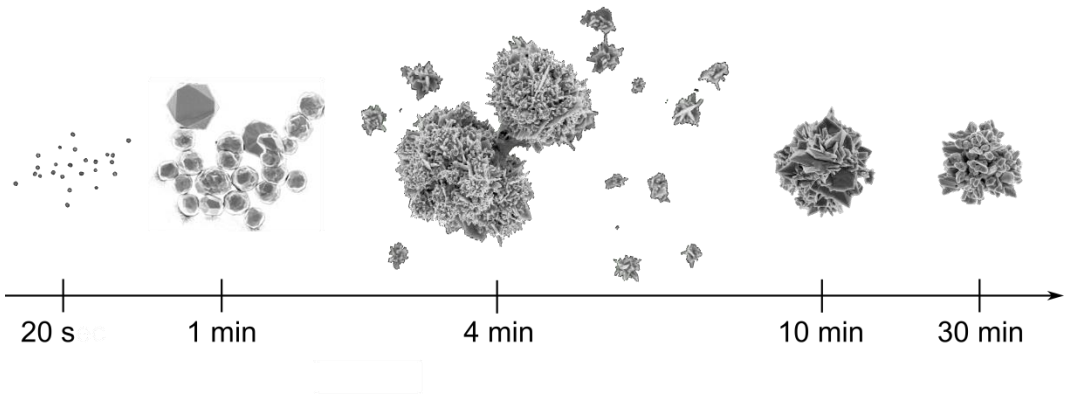

Figure 45 Morphological forms dominating in the five consecutive stages of the formation of the AuMFs. For the reaction times marked on the axis, consecutively 20 nm NPs, 100 nm – 1 µm NPs, 2.0 – 3.5 µm MFs and small colds, sharp-edged MFs, and round-edged MFs were observed.

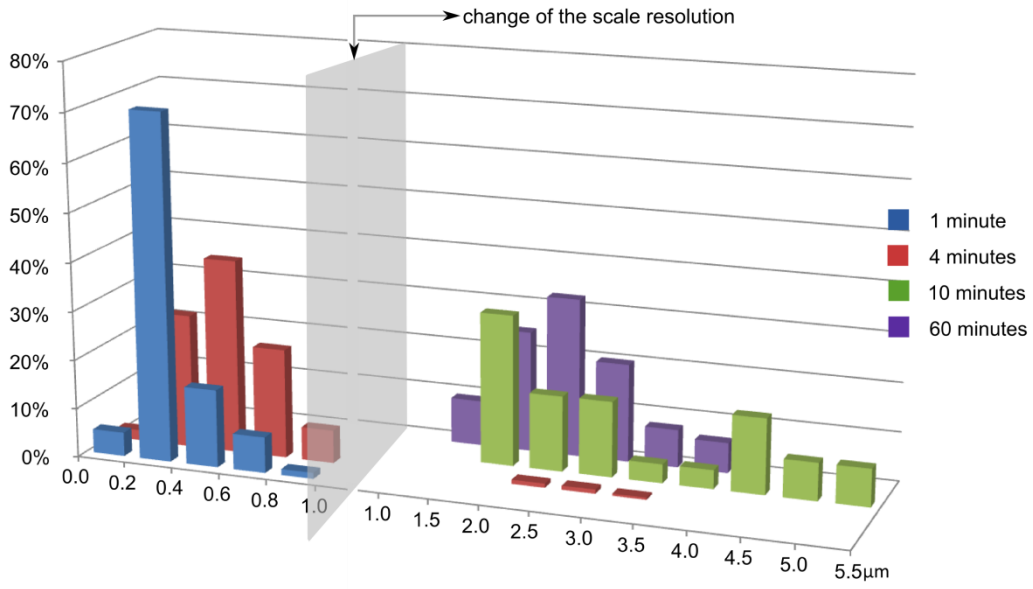

Figure 46 Histogram presenting the size (length of the diameter of the top view projection) distribution of the gold objects present after 1, 4, 10, and 60 min of the reaction.

Stage 1: In the first stage (20th s of the reaction) AuNPs with a diameter of about 20 nm were the main observed morphological form. **Stage 2:** After 1 min. of the reaction, the particles were significantly bigger (100 nm - 1 µm) and their surface was slightly, but visibly folded. Beside the spherical objects (about 85% of all observed structures), also rods (5%) and triangular and hexagonal plates (8%) were found in large number. Among 2% of the remaining particles also the first flower-like structures can be found. **Stage 3:** At about the 4th minute of the reaction, the flower-like structure of gold particles began to be the dominating one. One could distinguish at least three main types of these structures, different in size and shape. Visibly abundant are small clods (100 – 400 nm in diameter) having less than twenty finger-like tips. The second type of morphology are structures of 2.0 – 3.5 µm in diameters. They are apparently much bigger and more complex than the first type, and seem to be composed of thin plates and spikes. The third type are AuMFs looking like clusters of NPs, and their size ranks between the sizes of the two forms mentioned earlier. **Stage 4:** In the next six minutes, both the shapes and sizes of AuMFs become uniform. The AuMFs appear to be built of plates and spikes of sharp edges, but these building blocks are more bulky and less numerous than the "petals" of the big AuMFs in Stage 3. Most AuMFs have diameters from the range 1.5 – 4.5 µm. **Stage 5:** After the following 20 min, this range became narrower (1.5 – 3.0 µm) and the edges of the AuMFs visibly smoother. Petals of the AuMFs looked more like fingers or clods than plates or spikes. In the 60th minute of the

reaction the AuMFs formed in Stage 5 were the only morphological form present in the reaction and did not undergo further morphological changes during, at least, the next 71 h.

By analyzing successively appearing gold shapes one can see that for the first 4 min their size increases and morphology becomes more complex. They are also at each stage roughly spherical and appear to grow equally fast in many directions. This observation suggests that the AuMFs are not random aggregates of gold plates, rods, and clods, but structures with a solid core from which petal-like forms grow radially. This model of the formation of the AuMFs has been confirmed in two ways. The first method was to cut the AuMFs and examine their inside using Focused Ion Beam (FIB) ablation. In this method gold atoms were sputtered from the AuMFs when high-energy gallium ions strike their surface. Four consecutive stages of the cutting process are shown in Figure 47 (upper images). The removal of subsequent layers of gold revealed the solid insides of the AuMFs. In the SEM images, radial lines (highlighted artificially in the fourth SEM image), suggesting the way the AuMFs form and grow, were also visible. It is noteworthy that FIB ablation is destructive for the specimen. For example, the visible vertical grooves on the cutting plane were probably made during the milling process, not during AuMF growth. A second way to verify the AuMF formation model was analysis of the AuMFs that formed on the water/air interface. Most of the AuMF sediment remains on the bottom of the reaction vessel during the reaction, but if the reaction mixture is not stirred, several particles, trapped on the interface, grow and undergo morphological changes. As can be seen in Figure 47 (bottom panel), they look like halves of the typical AuMFs. Their “petals” grow only in the solution and the radial patterns on their flat top portion reveal the direction of this growth. It is impossible to obtain these structures by combining randomly smaller particles in the complex AuMFs. Such shapes can be achieved only by the progressive build-up of gold on the steadily growing AuMFs.

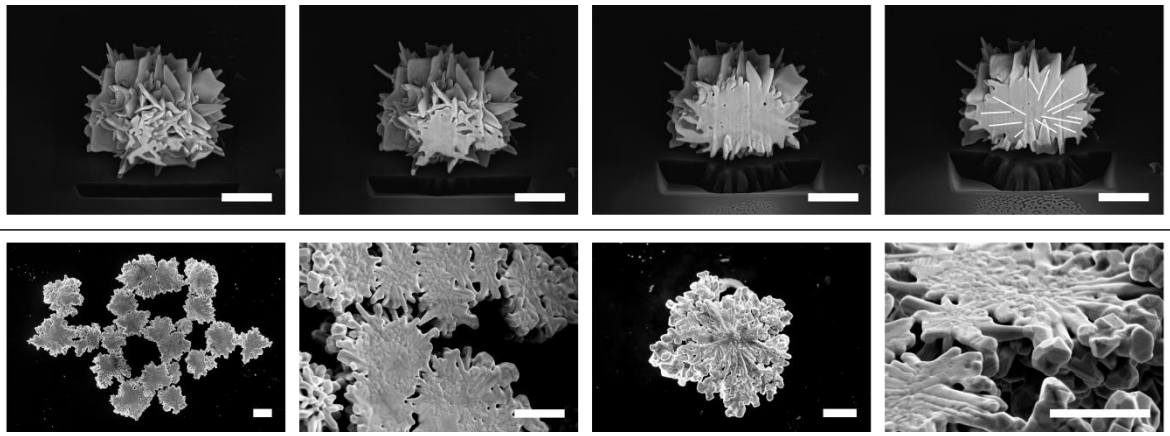

Figure 47 SEM images of the AuMFs. Upper panel: sharp-edged AuMF exposed to FIB ablation. Four images show consecutive stages of the process. In the fourth image artificial lines, highlighting the radial pattern on the cutting plane, were added. Bottom panel: AuMFs grown on the water/air interface during 24 hours of the reaction. All scale bars correspond to 1 μm.

4.5.5 Effect of the reaction time on the morphology of the AuMFs. The phenomenon of smoothing

The evolution of the shapes described in the previous section suggests interesting processes occurring in the solid state. Especially, the transformation of the AuMFs from Stage 4 into the form from Stage 5 seems to be curious because there is no growth of the gold particle, but rather a slight reduction of the size and rounding (smoothing) of the shape. To investigate this effect, silicon plates were dipped into the reaction solution *c*1 (3:8) for short (2-10 min.) and long times (from 30 min. up to 7 days). Analysis of the SEM images revealed that the AuMFs obtained for the short immersion times – independently of the composition of the reaction mixture – consisted of very thin, plate-like petals of polygonal shapes. For the immersion time of 30 min. the AuMFs were much smoother, and their surface was composed of rounded petals. A similar round-edged morphology of the AuMFs was also observed for longer immersion times. The shapes of the petals observed for the longest immersion time (7 days) did not differ much from those observed for the immersion time of 30 min. Examples of sharp- and round-edged AuMFs are shown in Figure 48a and Figure 48b, respectively. This process of rounding is all the more interesting when taking into account that it continues after complete consumption of auric acid, $HAuCl_4$ (section "Kinetics of the formation of the AuMFs").

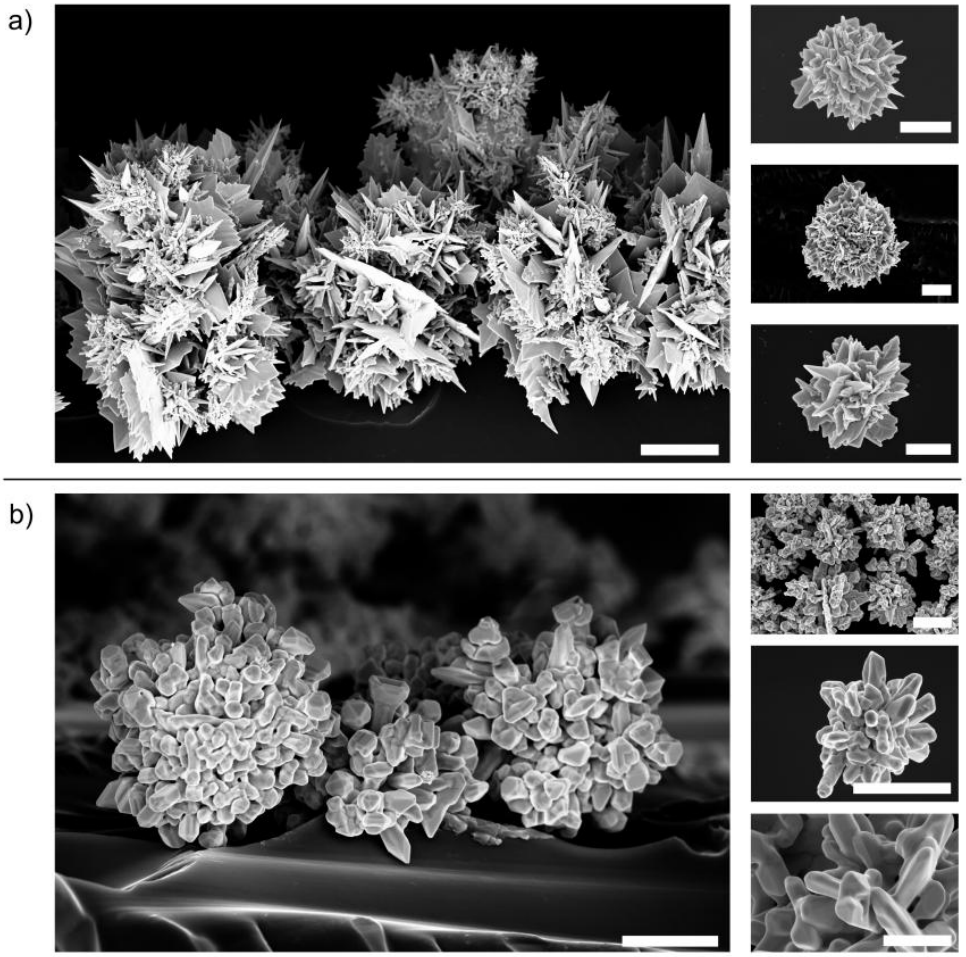

Figure 48 Control over AuMF morphology by reaction time: SEM images (side and top views) of the AuMFs deposited on silica for a) short (10 min.) and b) long (24 h) reaction times. In both cases identical compositions, *c*1 (3:8), of the reaction solution were used. Scale bar is 1 µm.

The first plausible explanation (Mechanism 1) for the edge smoothing is a thermodynamically driven redistribution of Au atoms within the AuMF. In this process, the Au atoms migrate away from energetically unfavorable places, like the sharp edges or tips, to decrease the average curvature of the surface. This atom redistribution process is slow compared to the autocatalytic growth of the AuMFs. Edge smoothing is expected to take place during the whole immersion time but its effects are most pronounced in the late stages of the AuMFs' growth process, when the reagents have been consumed and the growth of the AuMFs is terminated. Graphic presentation of Mechanism 1 is shown in the left image in Figure 49.

The second possible mechanism of the smoothing (Mechanism 2) is associated with the chemical composition of the post-reaction mixture. As one can figure out from the reaction equation and conditions, after the formation of AuMFs there is also HCl,

excess NH_2OH, and nitrous acid (HNO_2) in the reaction vessel. HNO_2 rapidly decomposes into nitric dioxide NO_2, gaseous nitric oxide, NO, and water. In the aqueous environment NO_2 disproportionates into nitric acid and nitrous acid.[176] Consequently, there are sharp-edged AuMFs exposed to the mixture of diluted *aqua regia* and hydroxylamine hydrochloride. According to Mechanism 2, the AuMFs are continuously dissolved by the mixture of acids present in the post-reaction mixture. As a result, there are gold cations close to the surface of the AuMF. However, the AuMFs do not become significantly smaller during this process because the gold cations are immediately reduced by hydroxylamine hydrochloride (still present in the reaction vessel) and, as gold atoms, built back into the AuMFs. The process, which is much slower than the formation of sharp-edged AuMFs, leads to the reduction of sharp tips or edges and the formation of more compact structures. The smoothing process due to Mechanism 2 is shown in the right image in Figure 49.

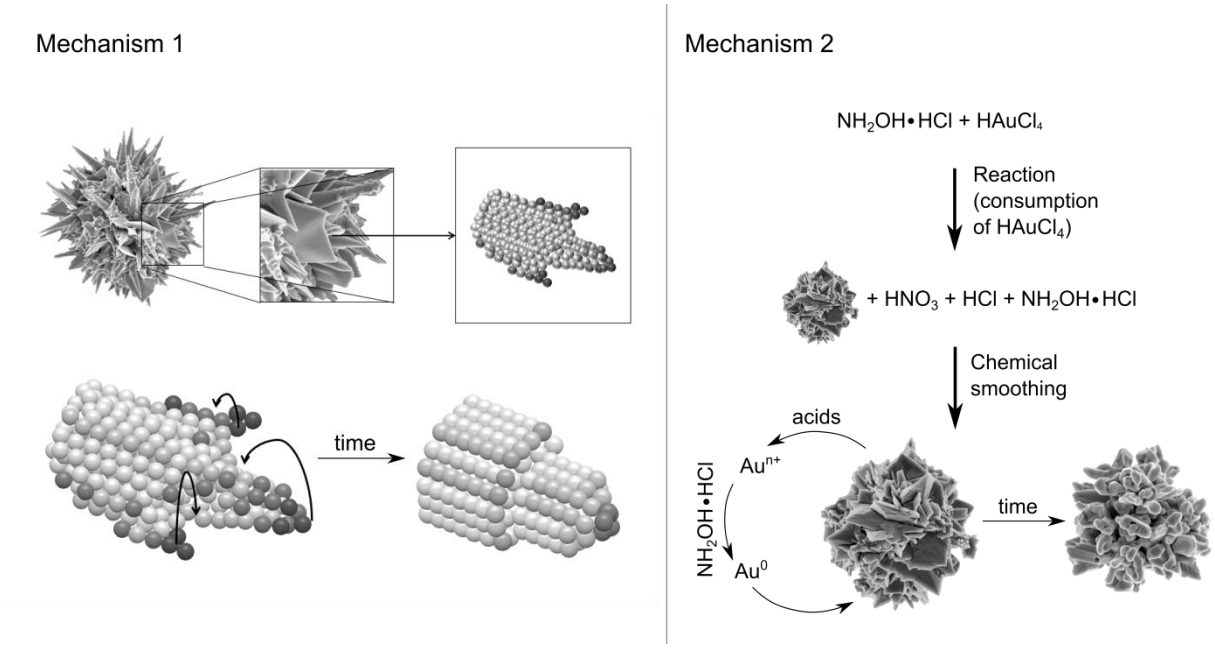

Figure 49 Graphic presentation of two considered mechanisms of the smoothing process. Left image: Mechanism 1. "Petals" of the AuMFs become smoother because of the thermodynamically driven redistribution of Au atoms from energetically unfavorable places into positions providing higher coordination numbers. Darker color of atom represents a higher energy. Right image: Mechanism 2. At the beginning of the reaction, only two reagents are present in the reaction mixture. After formation of the sharp-edged AuMFs there is a mixture of acids and the remaining $NH_2OH{\cdot}HCl$ in the reaction vessel. Under these conditions, oxidation of metallic gold and the subsequent reduction of gold cations occurs, leading to the smoothing of the AuMFs.

To check which mechanism – Mechanism 1 or Mechanism 2 – is correct, I conducted a series of experiments. As substrates I prepared silicon plates covered with AuMFs with sharp edges (removed from the reaction mixture after 20 min of the reaction, washed in the water, and dried). So prepared, the plates were placed in 4 mL of

the post-reaction mixture, namely solution *c*50 (introduced in the 3.3.1.2) from which gold particles were centrifuged after 20 min of the reaction (it is a colorless solution of pH ~1.5). Four types of experiments were conducted:

a) substrates placed in the post-reaction mixture for 24 h,

b) substrates placed in the post-reaction mixture for 30 days,

c) substrates placed in the post-reaction mixture for 30 days, but the solution was exchanged for a fresh one every 2-3 days,

d) substrates placed in water (blanc sample) for 24 h or 30 days.

Analysis of SEM images of AuMFs after reactions a)-d) confirmed that the post-reaction mixture is able to smooth the sharp edges of the AuMFs and change significantly their morphology (see Figure 50). In experiments a) and b) one could see the rounded edges of "petals". Interestingly, the degree of smoothing is very similar for 24 h and 30 days of reaction, suggesting rather fast consumption of the reagents (oxidizing acids or reducing hydroxylamine). In reaction c), where reagents were added every 48-72 h, the cycle of oxidation and reduction of gold could occur more times than in a) and b), leading to the formation of well-formed crystals. For the control probe (reaction d)) no changes in the AuMFs' morphology were observed, regardless of the reaction time. This indicates that it is not only a liquid environment, but also its proper chemical composition is required for the smoothing process to occur. This finding rules out the validity of Mechanism 1.

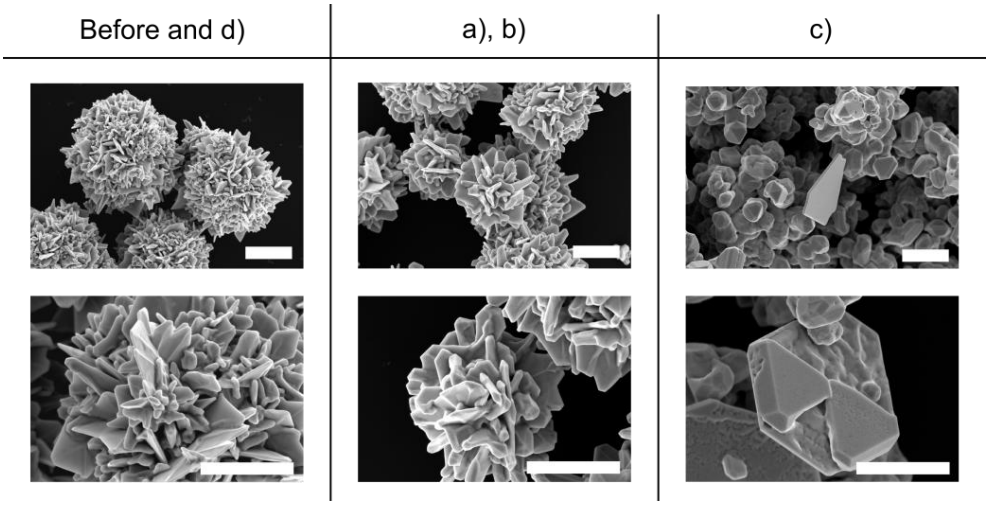

Figure 50 SEM images showing typical metal structures observed on the substrates before reaction and after the experiments a), b), c) and d). The length of the scale bar corresponds to 1 µm.

Next, I conducted experiments to verify Mechanism 2. According to this hypothesis, the sharp edges of the AuMFs are smoothed by the acids. To examine the

effect of hydrochloric and nitric acid on AuMF morphology, I prepared the following solutions:

e) diluted HCl_{aq} (pH = 1.5),

f) diluted $HNO_{3,aq}$ (pH = 1.5),

and placed AuMF-covered substrates (prepared in the same way as in experiments a) - d)) in 100 mL of the solutions for 24 h. SEM analysis of probe e) showed smaller (diameter 0.5 – 2.0 μm) and rounder AuMFs than before the experiment. Interestingly, new geometric metal forms also appeared, especially triangular and hexagonal plates with the diagonal about 2.5 μm. In probe f) only smoothed and diminished (1.0 – 3.0 μm) AuMFs were observed. Typical metal forms observed for each reaction are presented in Figure 51. Reduction of the size of the AuMFs and the dissolution of sharp edges by the acids is the argument supporting the validity of Mechanism 2.

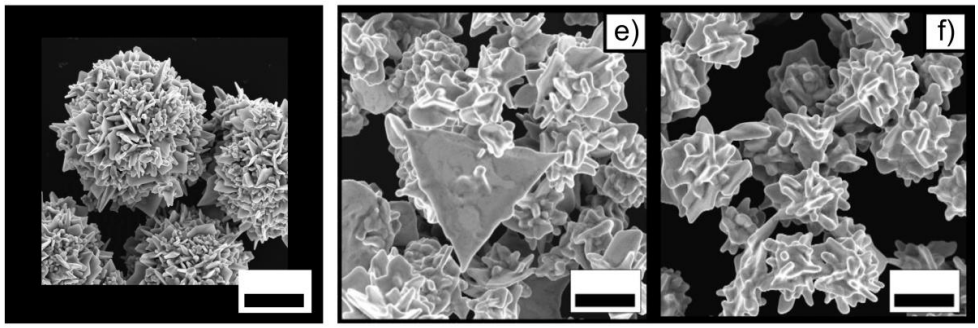

Figure 51 SEM images of the AuMFs after 20 min of the AuMFs synthesis (left image) and the same AuMFs after 24 h in diluted solutions of HCl (e) and HNO_3 (f).

It is worth commenting here on reaction e). Dissolution of the AuMFs in the diluted HCl is a very interesting and noteworthy fact because it is generally accepted that noble metals do not react with hydrochloric acid. Gold is supposed to dissolve only in *aqua regia* and selenic acid.[177] On the other hand, there are reports in the literature on the dissolution of AuNPs in HCl.[178] In contrast to bulk gold, small AuNPs, especially smaller than 10 nm, are chemically active: they displace hydrogen from acids and catalyze chemical reactions (for example CO oxidation and propylene epoxidation).[179] The results of my experiments show that the AuMFs reactivity is close to the reactivity of AuNPs, despite a size bigger than 1 μm.

4.5.6 Kinetics of the formation of the AuMFs

To investigate the kinetics of the reaction of AuMF formation, I monitored changes of the absorbance of the unconsumed Au^{3+} ions in the solution *c*1 using UV-Vis

spectroscopy. The absorbance spectrum of the $HAuCl_4$ ions displayed a maximum at λ ~220 nm and a shoulder at λ ~290 nm. According to the literature,[180] both of these are due to the ligand-to-metal charge transfer (LMCT) bands of $[AuCl_4]^-$ ions between gold and chloro ligands. In my analysis I assumed that – for the concentrations of the auric acid used – Beer's law holds and the absorbance is proportional to the concentration of the $[AuCl_4]^-$ ions. Also, for the sake of simplicity, in the fitting procedure (*vide infra*) I set the proportionality constant equal to unity and treated the absorbance at λ_{290} as the Au^{3+} concentration. The time dependence of the value of the absorbance at λ_{290} is plotted in Figure 52a. Because of the high excess of $NH_2OH{\cdot}HCl$ used in the reaction of formation of AuMFs, I used a pseudo-first order approximation.

I employed a minimalistic reaction model that accounts for the kinetic data obtained. According to this model, the reaction proceeds in two stages, which are the nucleation and autocatalytic growth of the metallic clusters. From the plot it follows that the first step of the reaction occurs in the first five minutes. The second stage takes place roughly between the fifth and twelfth minute of the reaction. In general, the reaction time of the chemical reduction of gold ions observed in my method is similar to that reported by other researchers for seedless methods.[161,167,170,171,172,173]

This two-step model follows from the fact that hydroxylamine is thermodynamically capable of reducing Au^{3+} ions directly to metallic gold,[181] but this reaction is dramatically accelerated by the presence of gold surfaces.[138,182] For this reason the production of new nuclei is suppressed in a solution that contains colloidal gold nanoclusters.[138] One therefore expects that formation of the AuMFs occurs in the following two stages. (i) Initially, the Au^{3+} ions are reduced in the bulk solution to form nuclei. Although the created nuclei grow autocatalytically, at this stage the consumption of the gold ions is due mainly to the nucleation processes. (ii) As the concentration of the nuclei (seeds) increases, the nucleation process is gradually suppressed and replaced by the autocatalytic (surface catalyzed) reduction of Au^{3+}. The stages are described below.

Nucleation: Reduction of the Au^{3+} ions directly to metallic gold is described by the following one-step mechanism:

$$A \xrightarrow{k_1} B, \tag{33}$$

where A stands for Au^{3+}, B is metallic gold, and k_1 is the effective rate of the reduction of Au^{3+} ions (*i.e.*, the nucleation process). The reaction described by eq. (33) yields exponential decay of the concentration of Au^{3+} ions, $[A](t)$,

$$[A](t) = A_0 \exp(-k_1 t), \tag{34}$$

where $[A]_0$ is the initial concentration of Au^{3+} ions in the reaction solution.

Autocatalytic growth: I assume that the surface catalyzed reduction of Au^{3+} occurs according to the scheme:

$$A + B \xrightarrow{k_2} 2B, \tag{35}$$

where k_2 is the rate of the reduction of Au^{3+} ions on gold surfaces. Reaction (35) gives the following time dependence of the concentration of unconsumed Au^{3+} ions:

$$[A](t) = \frac{\alpha}{1 + \beta \exp(\alpha k_2 t)}, \tag{36}$$

$$\text{with } \alpha = [A]_1 + [B]_1, \beta = [B]_1 / [A]_1.$$

Here $[A]_1$ and $[B]_1$ denote, respectively, the concentration of Au^{3+} ions and surface atoms of the growing clusters (seeds) present at the beginning of the autocatalytic growth stage. The quantities $[A]_0$ and $[A]_1$ are linked by the relation $[A]_1 = [A]_0 \exp(-k_1 t_n)$, where t_n is the duration of the nucleation stage.

I fitted the functions given by eq. (34) and (36) to the absorbance data using t_n, $[A]_0$, k_1, α, β, and k_2 as the fitting parameters. The fitting procedure yielded t_n = 5.0 ± 0.5 min, $[A]_0$ = 1.040 ± 0.002 and k_1 = (0.0550 ± 0.0006) 1/min for the nucleation reaction, and α = 0.853 ± 0.008, β = 0.0024 ± 0.0004, and k_2 = (0.85 ± 0.02) 1/min for the autocatalytic reaction. The resulting kinetic curve is plotted in Figure 52. In my attempts to model the formation of the AuMFs I considered also the two-step growth reaction that comprises both nucleation and the autocatalytic growth (eq. (33) and (35)) that is referred to as the Finke-Watzky (FW) kinetic model.[183,184] The FW model predicts however an S-shaped sigmoidal kinetic curve of the concentration of the unconsumed metal ions that did not fit our experimental data.

For reaction times shorter than ~12 min., corresponding to the late stages of the nucleation regime and the autocatalytic growth stage, I observed the sharp-edged morphology of the AuMFs. When the reagents were consumed, in the late phases of the autocatalytic growth stage, the round-edge morphology was observed. The three stages of AuMF formation – nucleation followed by autocatalytic growth, and the edge smoothing - are illustrated schematically in Figure 52.

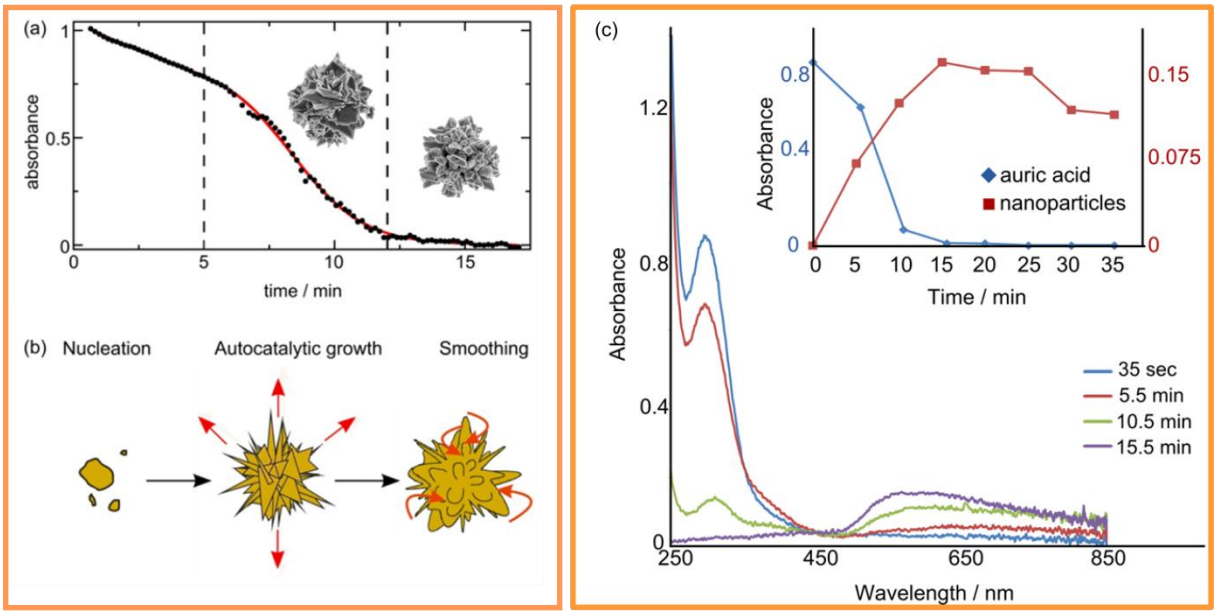

Figure 52 (a) Changes of the absorbance due to the unconsumed Au^{3+} ions during the formation of AuMFs in the *c*1 (3:8) reaction mixture. The red line is the fit of the two-step model (see the text) to the experimental data. Two SEM images show examples of the sharp-edged AuMF created in the autocatalytic growth stage (5-12 min.), and the round-edged AuMF observed for longer immersion times. (b) Cartoon representation of the three stages of the AuMF formation process: nucleation, autocatalytic growth, and the edge smoothing. (c) Detailed presentation of the volatility of the UV-Vis spectrum of the reaction mixture. The main diagram and the inset show a decrease in the intensity of the substrate signal and increase of the metal product peak. Over time, also the signal of the metal becomes weakened (see inset) because of the significant growth and sedimentation of gold particles.

4.5.7 Modifications of the reaction mixture and their effect on the morphology of the product

4.5.7.1 Introduction

In the previous sections of section 4.5, various concentrations and molar ratios of the two reagents, namely $NH_2OH{\cdot}HCl$ and $HAuCl_4$, were described. Here, I would like to present the products of reactions to which other compounds were added or from which some ions were removed. As was explained in section 1.2.2, generally, it is rather impossible to predict how the change of the reaction mixture will affect the morphology of the gold particles. However, there are many reports in the literature proving that even the small addition of some reagents could change the distribution of shapes and sizes/aspect ratios within the NPs synthesized. Apart from the addition of various organic compounds, those factors affecting the growth direction of gold are typically: halides, silver ions, and pH changes. In this section I present the impact of the mentioned components on the growth and final morphology of the AuMFs.

4.5.7.2 Preparation and analysis of samples

Preparation of reaction mixtures modified by halides

All structures were produced based on the general procedure described in section 3.3.1.2. Here, I replaced $NH_2OH{\cdot}HCl$ by its molar equivalent of NH_2OH and a desired halide salt. To the water solution of hydroxylamine, a solution of an appropriate halogen salt was added. Then, a solution of auric acid was added dropwise while shaking. A cleaned silicon plate was placed at the bottom of the reaction vessel for 2 h, then removed, dried, and analyzed.

Various concentrations (from the *c*1 – *c*50 range) and $HAuCl_4$:NH_2OH molar ratios (3:8 – 7:8) were studied, but for presentation I have chosen *c*50(3:8) mixtures. Details are presented in Table 3:

Table 3 Composition of the examined reaction mixtures.

	25 mM $HAuCl_4$	**40 mM $NH_2OH{\cdot}HCl$**	**80 mM NH_2OH**	**80 mM Halide salt**	**comment**
1	1,2 mL	2,0 mL	-	-	General procedure
2	1,2 mL	-	1,0 mL + 1,0 mL of H_2O	-	Product shown in Figure 53b
3	1,2 mL	-	1,0 mL	1,0 mL	Used salts: NaCl, KBr, KI, NaBr, CsBr and LiBr. Products shown in Figure 53 and Figure 54.

Preparation of the reaction mixtures modified by silver salt

In the reaction an addition of ammonia was used to prevent the formation of silver chloride. In a preparation of 50%-50% Au-Ag samples, aqueous ammonia (NH_4OH, 25%, 60 µL) was added to the solution of silver nitrate ($AgNO_3$, 25 mM, 0.6 mL). Then a water solution of auric acid (25 mM, 0.6 mL) was added. The prepared mixture was then added dropwise to a solution of hydroxylamine hydrochloride (40 mM, 2 mL). A cleaned silicon plated was placed on the bottom of the reaction vessel for 2 h, then removed, washed, dried and analyzed. For different contents of silver, proportionate amounts of ammonia were used, but never less than 60 µL for 3.2 ml of the reaction mixture.

4.5.7.3 Influence of halides

Typically, in my experiments I used an aqueous solution of $NH_2OH{\cdot}HCl$ mixed with $HAuCl_4$ solution as the reaction mixture. However, during the experimental research, I also examined the suitability of pure hydroxylamine, instead of its hydrochloride, and I found the product of the reaction completely different from the

typical AuMFs. Instead of the MFs (Figure 53a), I obtained much smaller (200 – 400 µm) spherical objects of slightly folded surface, connected to each other (Figure 53b). This finding drew my attention to the importance of the role of HCl in the reaction mixture.

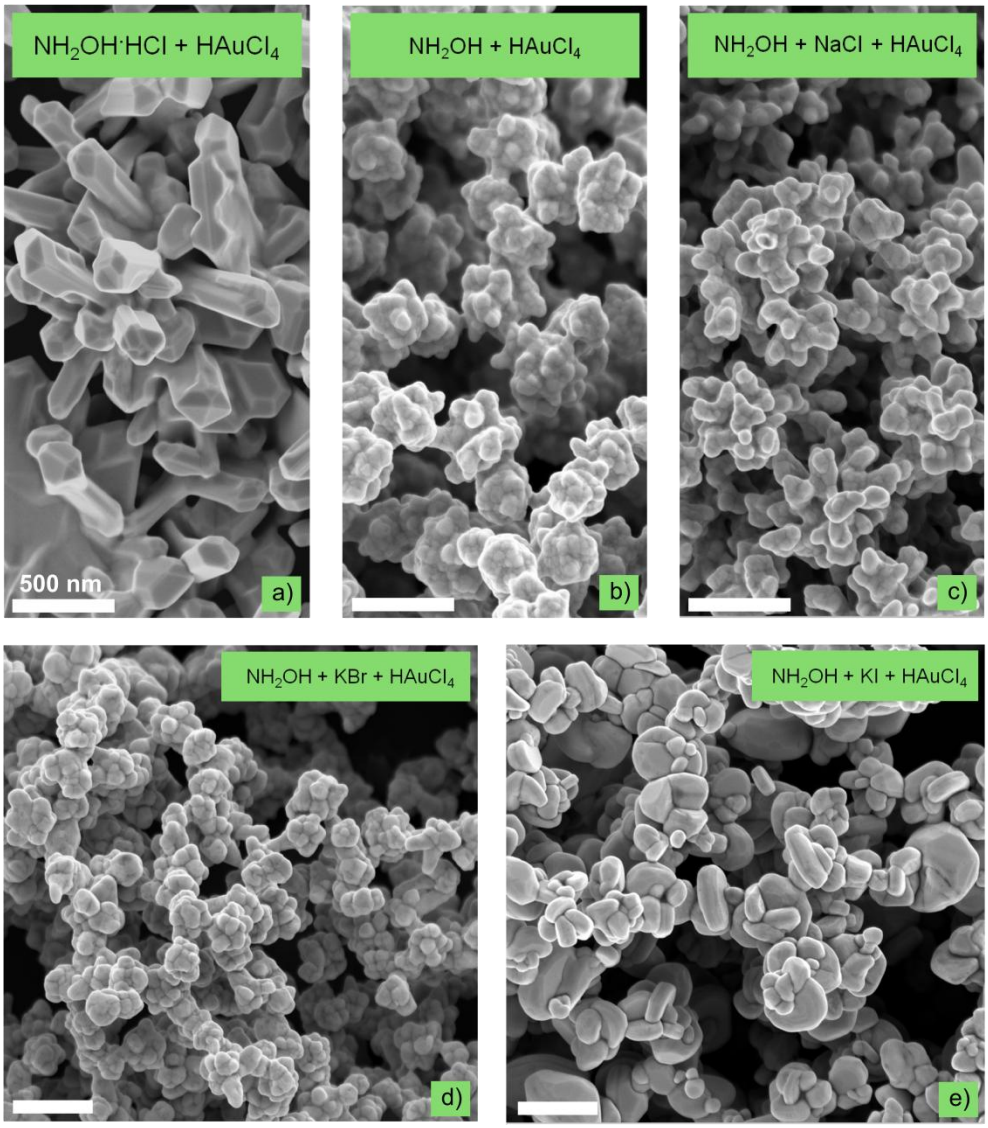

Figure 53 SEM images of gold structures obtained for the (a) original reaction and its modification: b) NH_2OH instead of NH_2OH·HCl, c) HCl replaced with NaCl, d) with KBr, e) with KI. Scale bar is 500 nm.

To examine the impact of the hydrochloride in the NH_2OH·HCl reagent I decided to replace HCl with sodium chloride (NaCl) and other basic halide salts (KBr and KI). Therefore, the new reaction mixture consisted of water solutions of $HauCl_4$, NH_2OH and selected halide salts. In the experiments I used salt concentrations corresponding to the concentration of HCl in the original reaction mixture (increasing the concentration two and five times did not affect the morphology of the product). The results of the new type of reaction are presented in Figure 53. Figure 53c shows that compensation of the chloride ions to the original level by addition of NaCl in place of HCl leads to the

fabrication of properly branched structures. However, they were still much smaller than AuMFs, and their nubs are more rounded. This indicates the important role of the hydrogen cation in the formation of flower-like structures. My preliminary studies of this issue showed that it is not the absolute concentration of the H_3O^+ (pH), but rather the $[H_3O^+]$:$[NH_2OH]$ ratio determines the morphology of the product. This issue must be, however, subjected to more detailed examination.

When KBr was used instead of HCl (Figure 53d), the synthesized gold forms were similar to those shown in Figure 53b. The metal product consisted of small folded clods whose size and shape differed significantly from typical AuMFs. A more interesting, though not a flower-like structure, was obtained in the reaction mixture to which KI was added. This inorganic salt promoted the formation of regular, disk-shaped forms. The obtained particles were slightly bigger (up to 600 nm) than those observed for KBr, but similarly spatially arranged (Figure 53e).

Besides determining the effect of halide ions on the morphology of the metal product I also investigated the impact of counterions. To my knowledge there are no reports in the literature showing the effect of small inorganic cations on the growth of gold crystals. In order to examine the impact of various counterions on the morphology of the formed product, I conducted a series of reactions of $HauCl_4$ with NH_2OH and inorganic salts of various cations and bromide anion (KBr, NaBr, CsBr and LiBr). The concentration and molar ratio of the reagents were the same as in the previous experiment.

Results of the screening of the cations are shown in Figure 54. As was expected, for various bromide salts used, I obtained the same type of morphology of the product – slightly folded spheres connected to each other, and arranged in a porous 3D structure. Beside slightly larger diameters of the spheres obtained in the reaction with KBr (Figure 54a) I observed no differences between the products of the reactions. This result shows that the influence of cations of the halide salts on the shape of the gold products described in 4.5.7.3 sub-section may be omitted.

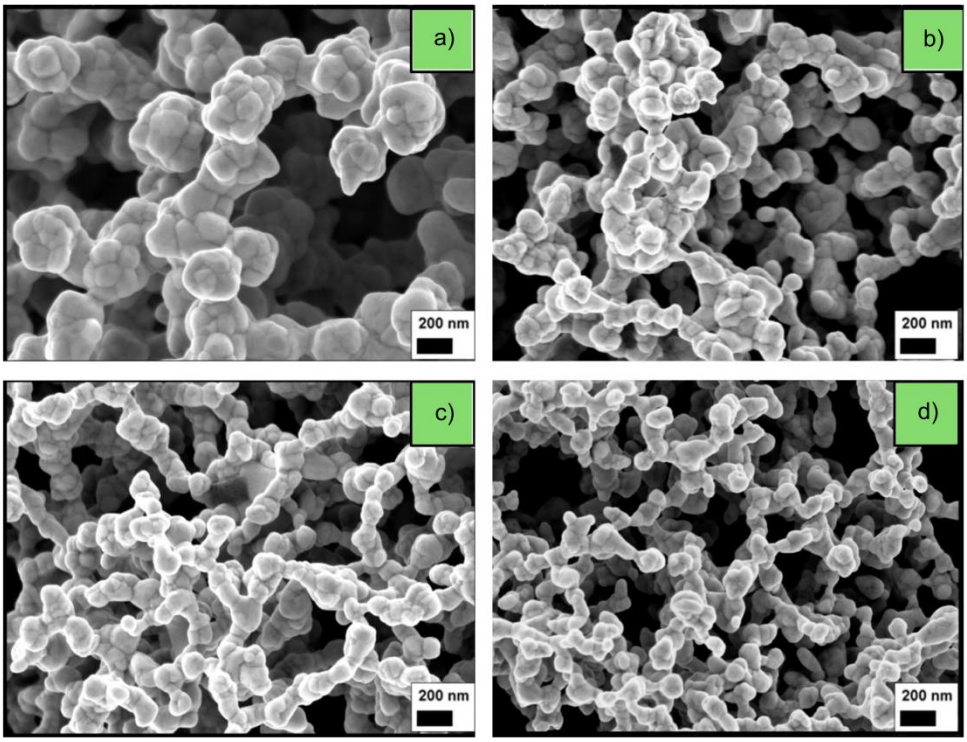

Figure 54 SEM images of the products of the reaction modified by the addition of a) KBr, b) NaBr, c) CsBr, and d) LiBr.

4.5.7.4 AuMFs in the presence of silver ions

In this section modifications of the reaction of $HAuCl_4$ with $NH_2OH{\cdot}HCl$, resulting in Au-Ag metallic structures, are presented. Then, in section 4.6.4.3, the possible application of these structures in SERS is discussed.

Synthesis of bimetallic MFs is based on the addition of silver salt to a reaction mixture containing a source of gold cations ($HAuCl_4$) and a reducing agent ($NH_2OH{\cdot}HCl$). Unfortunately, the addition of silver salt to this mixture is connected with one experimental difficulty, namely the formation of an insoluble silver chloride, AgCl. To avoid formation of this precipitate, I added ammonia to the reaction mixture, which eventually consisted of $HAuCl_4$, $NH_2OH{\cdot}HCl$, silver nitrate $AgNO_3$, and ammonia NH_3, all of them as aqueous solutions. The addition of ammonia to AgCl leads to formation of the $[Ag(NH_3)_2]^+Cl^-$ complex which is soluble in water:

$$Ag^+ + Cl^- \rightarrow AgCl \quad (37)$$

$$AgCl + 2NH_3 \rightarrow [Ag(NH_3)_2]^+ + Cl^-. \quad (38)$$

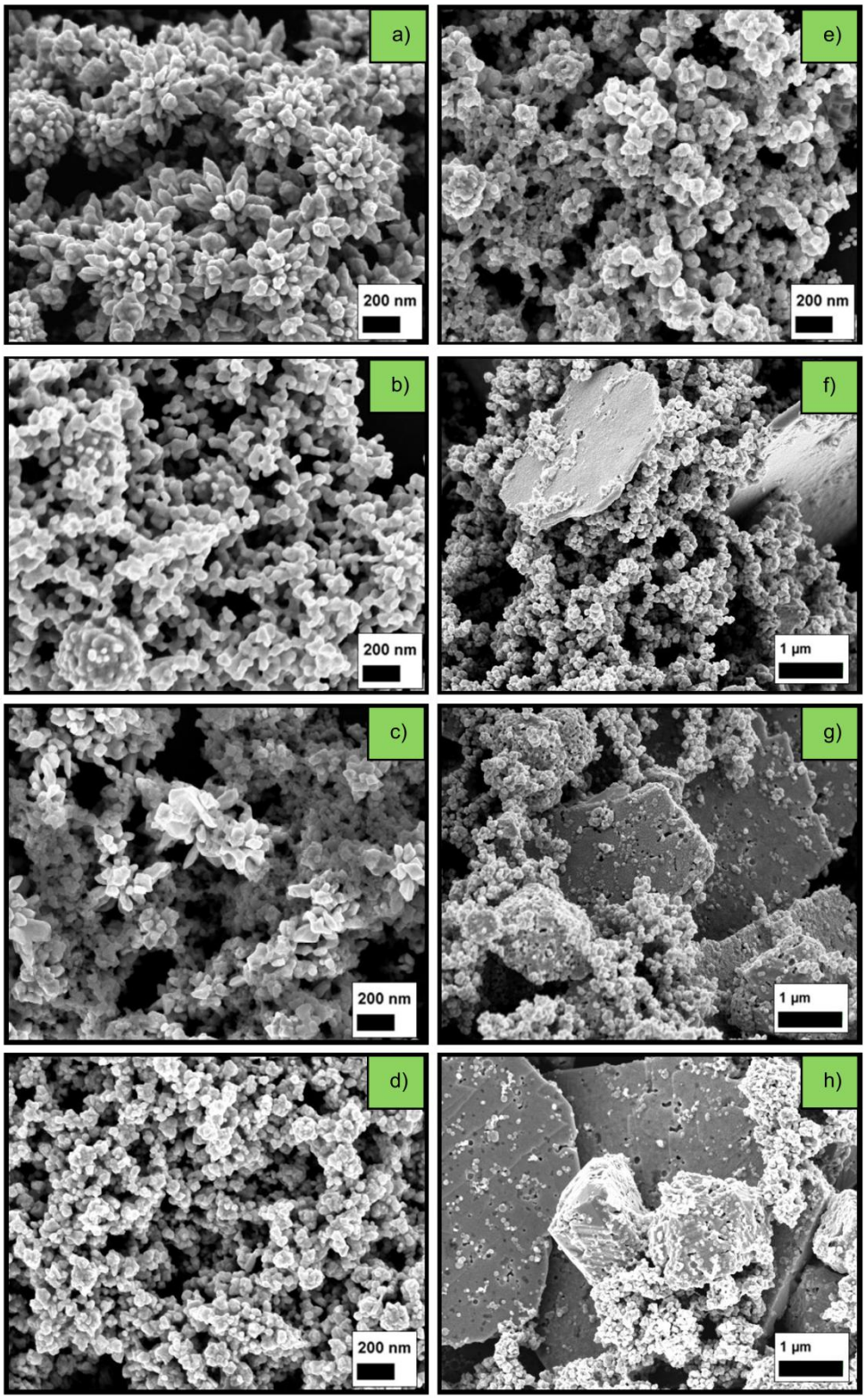

Figure 55 Bimetallic structures obtained when a) 1%, b) 3%, c) 5%, d) 10%, e) 20%, f) 30%, g) 50% and h) 70% of all metallic ions present in the reaction mixture were silver ones.

In my experiments silver ions accounted for 1 to 70% of all the metal ions used in the reaction. I applied *c*50 concentration of the reagents and the total amount of metallic ions in the reaction mixture was equivalent to the amount of gold ions in the *c*50

reactions described in sub-section 4.5.2. In Figure 55a-h I present the typical structures obtained when, respectively, 1, 3, 5, 10, 20, 30, 50, and 70% of all metallic ions were silver. As is shown, only with small amounts of silver (≤ 20%) was I able to achieve a uniform product, and only with 1% of silver content could the formed structure be described as "flowerlike". In the latter case, I observed MFs of diameter ~500 nm and spindle-like petals. EDX analysis confirmed a uniform distribution of silver and gold in the structure. For higher contents of silver (3% - 20%) these flowerlike types of structures were not observed. Instead, I obtained a porous 3D structure built of small folded spheres connected to each other (Figure 55b-e). Further increasing of the amount of silver led to the formation of three dominating types of structures in each sample. As can be seen in Figure 55f-h, the 3D porous structure, polyhedra, and large (several micrometers in diameter) plates were present. Using EDX spectroscopy I found that the new forms are made mainly of silver, while the porous film is predominantly gold (see Figure 56). This indicates that for higher concentrations of silver separation of metals occurs and bimetallic structures are not formed.

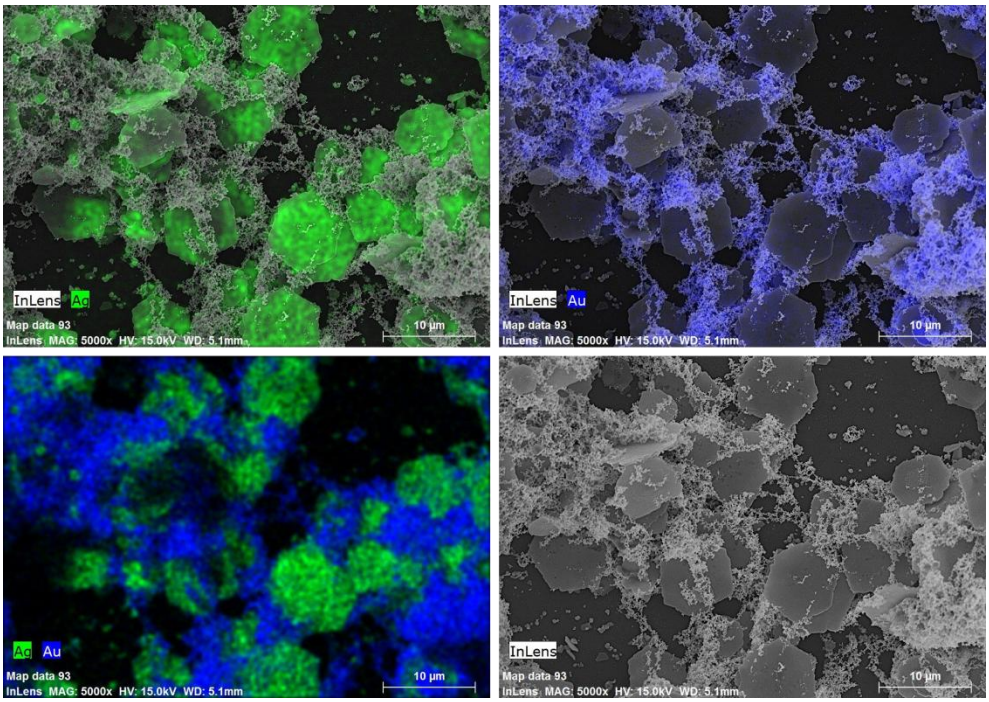

Figure 56 EDX analysis of the Au-Ag structure containing 70% silver. In the SEM image (InLens, grey scale), gold (Au, blue) and silver (Ag, green) domains are marked.

4.5.8 Conclusions

In this section a novel facile one-pot method for synthesis of micrometer-sized AuMFs was described. By changing the composition of the reaction mixture and/or the reaction time, one can easily control the morphology of the AuMFs; that is, the average number and shape of petals of which the AuMFs are composed. Also, the kinetics of the reaction was investigated, and the process of formation and smoothing of the AuMFs was analyzed as well. It was found that the AuMFs originate in an autocatalytic process in which initially spherical particles are formed. Next, their rapid growth and symmetrical branching can be observed. So-called "petals" of the AuMFs are originally sharp-edged and resemble thin plates, but after 15-20 min they become rounded. It was found that, surprisingly, these morphological changes result from the reactivity of the AuMFs towards acids that are present in the post-reaction mixture. The acids oxidize metallic gold to gold cations that are, in turn, immediately reduced by the remaining part of $NH_2OH{\cdot}HCl$ and return as gold atoms into thermodynamically favored places on the AuMF.

In sub-section 4.5.7 I presented the products of the modified reaction of synthesis of AuMFs. Due to the addition of halide or silver salts, I was able to fabricate new types of gold and gold-silver structures of various morphologies. These studies showed the strong influence of even small amounts of additives on the characteristics of the formed structures. In most cases, porous structures made of different types of folded nubs connected to each other were obtained. Only the original reaction mixture ($NH_2OH{\cdot}HCl$ and $HAuCl_4$ solution), however, allowed for the synthesis of well-formed, micrometer-sized AuMFs.

4.6 Application of the AuMFs for one-step fabrication of a highly reproducible SERS platform

4.6.1 Introduction

Based on current knowledge about SERS (sections 1.2 and 1.4), one could expect that the tips of the "petals" of the AuMFs are sharp enough to allow excitation of the localized plasmons. Additionally, points in which the adjacent AuMFs are in contact should work as hot-spots, improving the enhancement of the analyzed signal. My idea was to immobilize the AuMFs on a solid substrate and use them in SERS. Ideally, a solid substrate should be completely covered with a dense layer of the AuMFs, providing a gold, rough surface for the deposition and analysis of the analyte.

Here, I present a novel and facile method enabling the simultaneous synthesis and deposition of AuMFs on hydrophilic solid substrates. The method is a one-pot process using only two simple reagents ($NH_2OH{\cdot}HCl$ and $HAuCl_4$) in an aqueous reaction mixture. The AuMFs are synthesized and immediately self-assemble onto a solid substrate, forming a porous multi-layered film. I demonstrate that substrates covered with a layer of the AuMFs using the presented technique can be employed as efficient, highly reproducible SERS platforms, providing an enhancement factor of the order of 10^6.

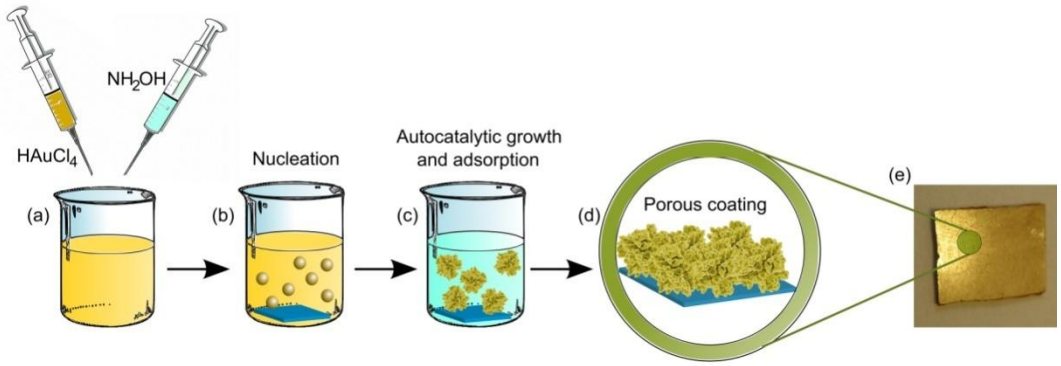

Figure 57 Covering a substrate with AuMFs. (a) Aqueous solutions of $HAuCl_4$ and $NH_2OH{\cdot}HCl$ are mixed. (b) Substrate plate is placed horizontally in a vial containing the reaction mixture. Metallic gold is formed in the bulk solution. (c) MFs are formed and adsorbed on the plate. (d) After the reaction is completed, the plate is taken out, washed, and dried. The resulting porous gold coating is mechanically stable and can be further processed without additional cleaning. (e) Substrate covered with as-prepared gold layer. Photo image of a silicon plate covered with AuMFs (applied as the SERS platform). The width of the plate is 10 mm.

Synthesis of rough flower-like complexes directly on surfaces is usually carried out electrochemically via electrodeposition[163] or a seed-mediated growth approach[168]. I present a process in which clusters of metallic gold (AuMFs) are formed in the bulk solution and simultaneously adsorbed onto a substrate plate to form a thick, permanent layer of sediment. My experimental procedure is outlined schematically in Figure 57.

4.6.2 Preparation and analysis of samples

Fabrication of the SERS platform

To obtain the SERS platform, I followed the general covering procedure outlined in Figure 57. Silicon plates were applied as substrates. Before use, the plate was roughened by scratching it with sandpaper (grit size 500). The roughened plate, cleaned as described above, was placed horizontally at the bottom of a vial containing a *c*50 (3:8) fresh reaction mixture [the *c*50 (3:8) mixture consists of one volume of 40 mM NH_2OH with 0.6 volume of 25 mM $HAuCl_4$]. The depth of the solution column above the plate was about 10 mm. After 24 h the plate with the deposited AuMFs porous film was carefully washed subsequently with deionized water and with methanol and then dried in the air. Finally, the plate was – without additional cleaning – immersed in the analyte solution for 6-48 h, and dried in air before the SERS measurements.

Instrumentation

SERS measurements were performed using the Renishaw InVia Raman system equipped with a He-Ne laser emitting a 632.5 nm line used as the excitation source. The light from the laser was passed through a line filter, and focused on a sample mounted on an X-Y-Z translation stage with a 50 × microscope objective. The Raman scattered light was collected by the same objective through a holographic notch filter to block out Rayleigh scattering. An 1800-groove/mm grating was used to provide spectral resolution of 1 1/cm. The Raman scattering signal was detected by a 1024 × 256-pixel RenCam CCD detector. The SERS signal was collected for a dried sample on the SERS substrate. SERS spectra were acquired using 150 s integration time, and processed with Renishaw software WiRE 3.2. All SERS measurements presented in this thesis were made and interpreted by Dr. Agnieszka Kamińska from the Institute of Physical Chemistry of the Polish Academy of Sciences.

4.6.3 Gold film built of the AuMFs as a platform for SERS

To produce a dense layer made of the AuMFs, multiplication of a number of the MFs synthesized in the reaction was needed. I achieved this effect by increasing the concentration of the reagents used, namely using a *c*50(3:8) reaction mixture for 24 h. As already explained in section 4.5.3, a higher concentration does not influence the morphology (like the size of the AuMF or the quantity of "petals") of a single MF. The only changes I observed were (i) a significant increase in the number of AuMFs and (ii) unification of their sizes and shapes. The product of this modified reaction was visible as a dense, rubiginous layer of sediment on the bottom of a vial. As one can see in Figure 58a, the same thick layer also covers a solid substrate (in the figure: silicon or frosted glass) placed in a vial. This orange-brown film is made entirely of gold and shines metallically when illuminated by a flash lamp (plate C2, Figure 58a).The thickness and mechanical durability of the resulting self-assembled layer is illustrated in Figure 58b. In this image, a gold film lifted by gas bubbles, resembling a tent, is shown.

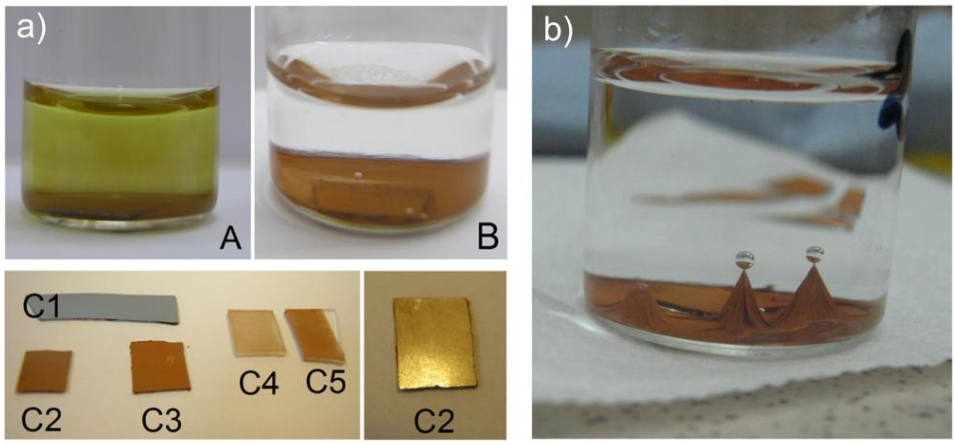

Figure 58 Presentation of the coating process. a) In the first minutes of the reaction the yellow color of the solution and rubiginous color of the precipitating product are visible (A). After 24 h the bottom of the vial and the solid substrate are covered with the AuMFs (B). Lower panel shows silicon substrate before (C1) and after (C2, C3) the process. Plates C4 and C5 are pieces of frosted glass covered with AuMF-films of various thickness. The last picture of this panel presents plate C2 illuminated by a flash lamp. b) Tent-like forms made of gold film raised by gas bubbles.

To ensure good coverage of a SERS platform by gold, the surface of the substrate plate was roughened prior to immersion in the reaction mixture. The roughening of the substrate's surface provided a "scaffolding" for the adsorbing AuMFs and facilitated fabrication of a thick, mechanically durable porous layer. The spatial structure of such a nano-roughened layer composed of AuMFs deposited on a silica plate is shown in Figure

59. Before the SERS measurements, the prepared substrate was dipped in a solution containing analyte.

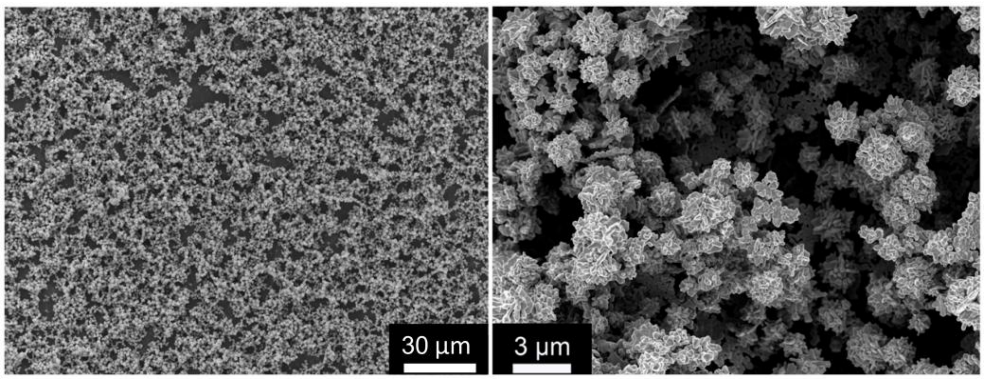

Figure 59 SEM images of a silicon plate covered with gold porous film composed of AuMFs. Left and right images show different magnifications of the same sample.

For application purposes SERS substrates are required to have good stability and reproducibility, both within single substrates and between different substrates. Figure 60a shows representative SERS spectra of *p*-mercaptobenzoic acid (*p*-MBA) adsorbed on the AuMF deposit, recorded for three different spots of the sample, marked as B, C, and D. As seen, the position and intensity of all modes corresponding to *p*-MBA (646, 835, 1080, 1177, 1280, and 1587 1/cm) exhibit remarkably small intra-sample variability. The standard deviation of the relative intensity of the 1080 1/cm *p*-MBA mode obtained for 100 random locations distributed within a single sample surface was less than 15%. Figure 60b shows Raman spectra of *p*-MBA recorded from four different, independently prepared SERS substrates (marked as A, B, C, and D). As can be seen, the SERS signals taken from the four samples are well consistent both in intensity and shape. For example, the intensity of ν_{8a} aromatic ring vibrations mode observed at 1080 1/cm varied by less than 20% between the different surfaces. The values of the relative standard deviation calculated for our platforms are comparable to those achieved for other methods of fabricating SERS platforms. In the available literature, typical deviation of the SERS intensity across a single substrate is reported to be 3.5% – 15%. The deviation of the SERS intensity across surfaces prepared in different batches ranges from 10% to 30%.[185,186,187,188]

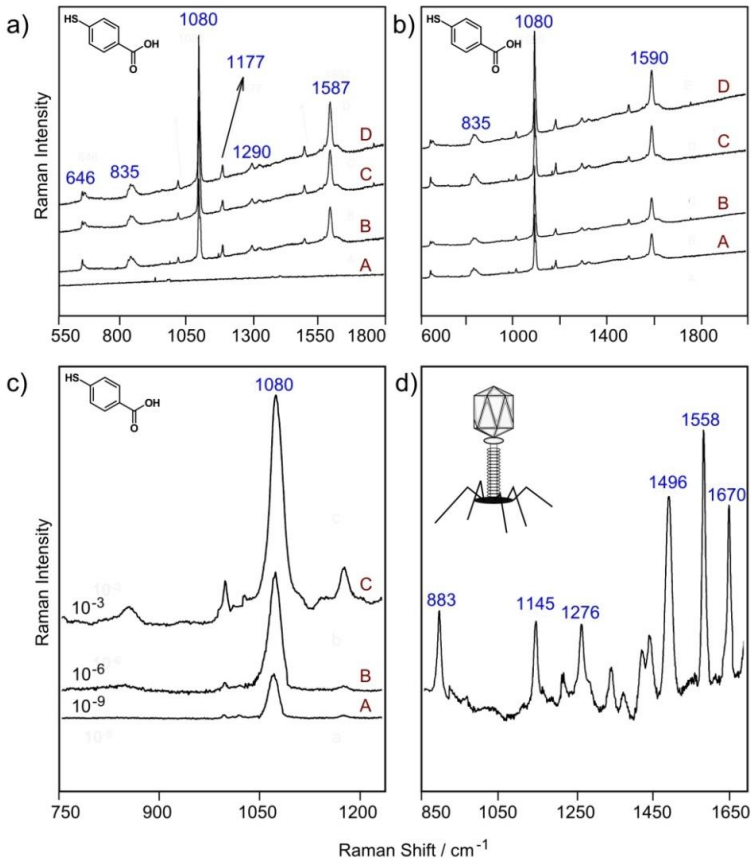

Figure 60 a) SERS spectra of (A) AuMF deposit on glass, and (B), (C), (D) *p*-MBA recorded from three different spots on the AuMF deposit. b) SERS spectra of *p*-mercaptobenzoic acid recorded from different, independently prepared AuMFs arrays, marked as A, B, C, and D. c) SERS spectra recorded for three different concentrations of *p*-mercaptobenzoic acid molecules in the analyte solution, 10^{-3}, 10^{-6}, and 10^{-9} M. d) SERS spectrum of bacteriophage λ displaying the Raman bands of O-P-O backbone (883 1/cm), cytosine (1276 1/cm), guanine (1496 1/cm), adenosine (1558 1/cm), and thymine (1670 1/cm) vibrational modes of DNA.

In order to estimate the detection limit for *p*-MBA molecules, the SERS measurements were performed for substrates that were immersed in solutions containing different concentrations of *p*-MBA. The substrates were immersed in each solution for the same period of time (2 h). Three analyte concentrations were applied: 10^{-3}, 10^{-9}, and 10^{-9} M. The SERS spectra recorded for these concentrations are shown in Figure 60c. As the amount of the analyte in the solution was reduced, the SERS intensity decreased, but the Raman band at 1080 1/cm could be observed even for the lowest *p*-MBA concentration used (marked as A in Figure 60c).

To demonstrate the applicability of the platforms for biomolecule sensing, I carried out SERS-based detection of the bacteriophage λ. This phage contains double-stranded linear DNA as its genetic material, and infects *Escherichia coli*. To prepare the SERS platform, 10 μM probe of bacteriophage λ in a phosphate buffered saline (PBS) (1 M, pH = 6.7) was immobilized on the surface of the AuMF-functionalized plate. The plate was kept in the solution at room temperature for 6 h. Then, excessive bacteriophage was

washed with a sodium dodecyl sulphate (SDS) solution in PBS (0.1%, v/v) for 5 min. Figure 60d shows the SERS spectrum of the DNA of bacteriophage λ, which clearly displays Raman bands at 883, 1276, 1496, 1558, and 1670 1/cm assigned to, respectively, O-P-O backbone, cytosine, guanine, adenosine, and thymine vibrational modes of DNA.[189] This result suggests that SERS platforms fabricated with my method can be successfully applied for identification of biomolecules.

4.6.4 Modifications of the basic platform for SERS

4.6.4.1 Introduction

The excellent results of the platform described in sub-section 4.6.3 became an inspiration for further research on its improvement. At the beginning, MFs with morphology changed by the addition of halides or Ag were examined.

The second path of optimization leads to the production of a mechanically stable platform. The goal was to immobilize more strongly the AuMFs on the solid substrate. The roughening of silicon, used so far, stabilized the AuMFs well enough to put a plate covered with them into a solution of an analyte, and then (without damage to the gold coating) remove it from the solution, dry it, then analyze it. All these activities have to be done, however, very gently; also, potential further transport of the sample could result in removal of the gold layer. The improvements described on the following pages allow not only an increase of the mechanical stability of the platform, but also its SERS-regarding parameters.

4.6.4.2 Preparation and analysis of samples

Preparation of platforms modified with silver or halides

All the platforms were prepared according to the procedure described in section 4.6.2. I examined reaction mixtures of the *c*50 concentration and 3:8 metal ions to the reducing agent molar ratio. The height of the liquid column above the solid substrate during the reaction was 1 cm (for higher columns the observed SERS-related properties were as good as for 1 cm while the mechanical stability was lower). Reaction was carried out for 24 h.

Preparation of platforms with new solid substrates

The new solid substrates were used without additional roughening with sandpaper. The change of the solid substrate did not entail, however, changes in the method of preparation, which always involves placing the plate horizontally in the

reaction mixture for 24 h, then washing with deionized water and with methanol then drying it in the air. Finally, the plate was – without additional cleaning – immersed in an analyte solution for 24 h, and dried in air before the SERS measurements.

Instrumentation

Surfaces shown in Figure 61 were analyzed using field emission scanning electron microscopy (FE-SEM) with Neon 40 - Auriga Carl Zeiss apparatus applying 5 kV beam voltage. Other SEM images presented in this sub-section were captured using Zeiss LEO 1530 applying 2-5 kV beam voltage. SERS measurements were performed using the Renishaw InVia Raman system equipped with a 300 mW diode laser emitting a 785 nm line used as the excitation source. The SERS signal was collected for a dried sample on the SERS substrate. The SERS spectra were processed with Renishaw software WiRE 3.2

4.6.4.3 SERS application of microflowers modified by halides or silver

All metallic structures described and shown in the figures in section 4.5.7 were screened for viability in SERS. According to the findings presented in section 4.6.3, metallic structures were synthesized from the solutions of *c*50 concentration and deposited on roughened silicon plates. In the case of structures modified by halides, however, the new gold films exhibited very weak SERS enhancement and unsatisfactory adhesion to the silicon substrate.

Au/Ag films seemed to be more promising – their strong adhesion to a solid substrate, even to polished silicon, allowed for convenient manipulation and analysis. However, SERS suitability, expressed by enhancement factor EF = 10^4 – 10^5 for 4-aminothiophenol, was lower than expected. The most interesting results were observed for Au/Ag films containing 1% of Ag in their metallic composition. This type of coating is composed of MFs of diameter ~500nm and spindle-like petals (Figure 55a). Using these SERS platforms, I was able to analyze a diluted solution (10^{-4} M) of acetylcholine; the calculated enhancement factor was 10^2. Despite EF lower than mentioned above, I consider this result interesting, because diluted acetylcholine is considered as a compound whose Raman spectrum is difficult to obtain.

In conclusion, the new metallic films presented did not exhibit the enhancement of the Raman signal desired for SERS platforms. The unsatisfactory performance was probably caused by the inappropriate morphology of the gold or gold/silver products obtained in the modified reactions. Thanks to the SERS analysis mentioned in this

section, it is clearly visible that – from all the structures I achieved – the flowerlike forms are the best platforms for SERS. This rule applies both for the Au and the Au/Ag structures. Unfortunately, in most cases, modification of the general reaction mixture by halides or silver salts leads to the formation of unbranched, poorly folded forms, which probably do not provide localized plasmons of proper frequency. Unlike in the case of the AuMFs, there are also no points of contact between the sharp tips of the "petals". Therefore, the new surfaces are devoid of hot-spots improving enhancement of the Raman signal.

4.6.4.4 Mechanical stability of SERS platform based on gold microflowers.

The idea to improve the mechanical properties of the SERS platform described in section 4.6.3 was to replace roughened silicon with a substrate providing better immobilization of the gold film. Trials with easily available, smooth surfaces like polished silicon, glass, polished GaN (gallium nitride), sandblasted glass, or ITO (indium tin oxide) were unsuccessful – the AuMFs, without a suitable scaffolding holding them to the surface, slid off from it. Therefore, I performed experiments with solid substrates covered with or made of metals. My idea was to simultaneously (1) roughen the surface of the substrate by its slight dissolution with an acidic reaction mixture ($HAuCl_4$ + $NH_2OH{\cdot}HCl$, pH ~1.5), and (2) to cover a modified substrate with sedimentating AuMFs. As metal-covered or metallic substrates I used: steel, aluminum, and phosphor bronze plates, ITO covered with AgNPs, silicon covered with AuNPs, and a layer of gold (100 nm thick) sputtered onto the silicon. (SEM images of these substrates after deposition of the AuMFs are shown in Figure 61.) This strategy proved to be, however, only partially effective. When gold additives on the surface were used (Figure 61a-b), epitaxial growth of the substrate consumed the greater part of the gold ions present in the reaction mixture. The amount of AuMFs formed was thus much smaller than observed for reactions with silicon as a solid substrate, and the morphology of the AuMFs differed from the expected. In addition, this approach did not enhance the adhesion of the AuMFs to the substrate at all. In the case of other metals (steel, phosphor bronze, aluminum, and silver), constituent ions reacted with the reaction mixture and changed the morphology of the MFs formed. The occurrence of a reaction with the new metals was observed, first, as the untypical color of the mixture during the reaction and, second, as a

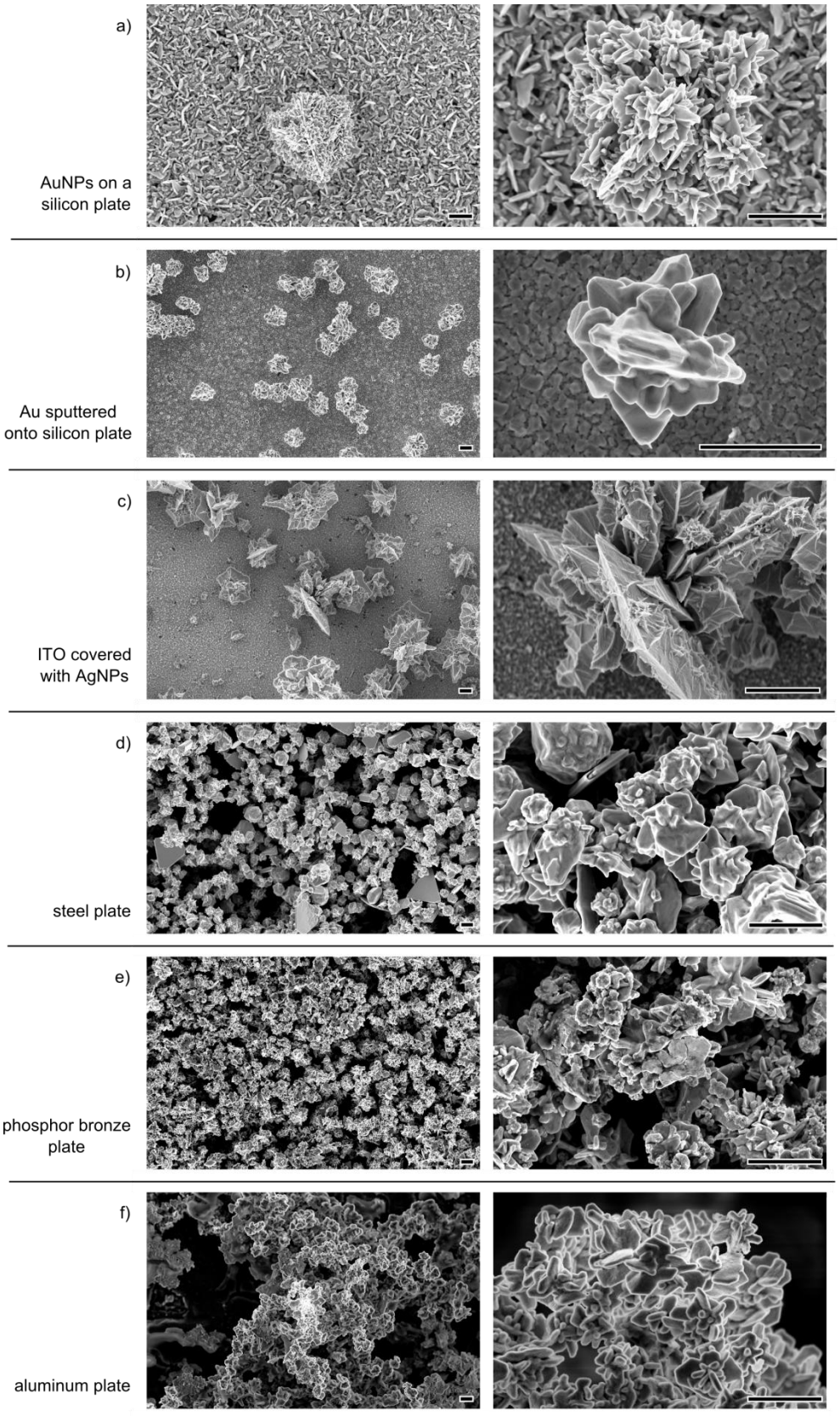

Figure 61 SEM images of metallic or metal-covered solid substrates after reaction in a *c*50 mixture of $HAuCl_4$ and $NH_2OH{\cdot}HCl$. In the images a-c the grown gold layer on the bottom of plates is visible. All MFs obtained (a-f) differ in morphology from typical AuMFs (*cf.* Figure 44). Scale bar is 1 µm.

new shape of MFs and the presence of many new, undesired metallic forms (Figure 61c-f). In each case mentioned, the suitability of the fabricated platforms for SERS was lower than that of the standard SERS platform, described in section 4.6.3. It follows that the morphology of typical AuMFs meets the requirements of SERS better than the new shapes presented in this section.

The successful method was to use surfaces covered with unpolished GaN (gallium nitride) as a solid substrate for immobilization of the AuMFs. I tested several types of GaN morphologies (all of them are presented in Figure 62), and found that those with a grass-like structure (Figure 62e-f) provide the best mechanical properties. Moreover, the type presented in Figure 62f, prepared by Witold Adamkiewicz and Jan Paczesny, covered with AuMFs, worked as an excellent SERS substrate, and allowed me to obtain better results than the platform described in sub-section 4.6.3. The obtained results are presented in the following section.

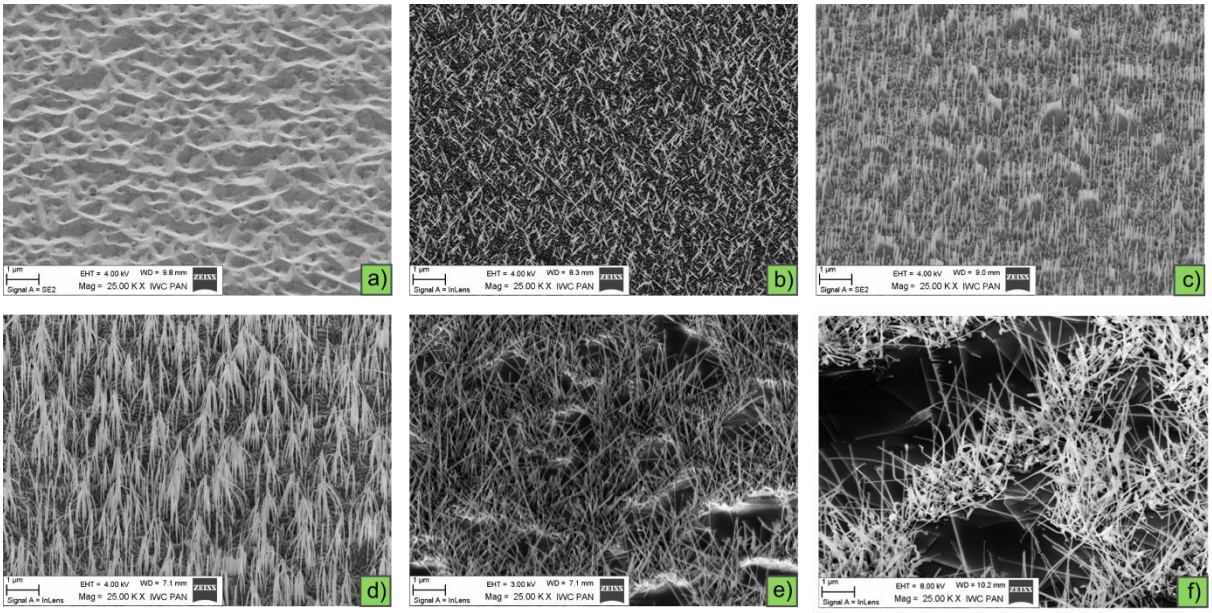

Figure 62 Solid substrates covered with GaN used for immobilizing the AuMFs: the GaN bone-marrow-like structures (a) and whiskers (b-f) of various length and distribution. All of them were examined as solid substrates for AuMF immobilization, but only types e) and f) provided desired mechanical durability of the prepared platform. GaN substrates were prepared by Igor Dzięcielewski (a, c, d),[190] Witold Adamkiewicz (b, e)[191] and by Witold Adamkiewicz in cooperation with Jan Paczesny (f).[87,192]

4.6.4.5 Bottom-up preparation of a stable and efficient SERS platform based on gold microflowers

Application of the solid substrate shown in Figure 62f allowed me to improve the mechanical and SERS-related properties of my SERS platform. The new approach requires, in comparison to the method described in section 4.6.3, a more complex

manner of fabricating a new solid substrate for the immobilization of AuMFs. The method of fabrication, developed by Jan Paczesny and Witold Adamkiewicz, relies on three consecutive self-assembly steps: (i) preparation of a netlike pattern of AuNPs on the water-air interface, (ii) transfer of the gold film onto a silicon substrate using the Langmuir-Blodgett technique, and (iii) using the prepared surface in the chemical vapor deposition (CVD) process of growing GaN nanowires. (Detailed description of these steps is given in references 87, 191, and 192.) A solid substrate prepared this way was then used in the AuMF immobilization process presented in Figure 57. SEM images of the platform in every stage of fabrication are shown in Figure 63.

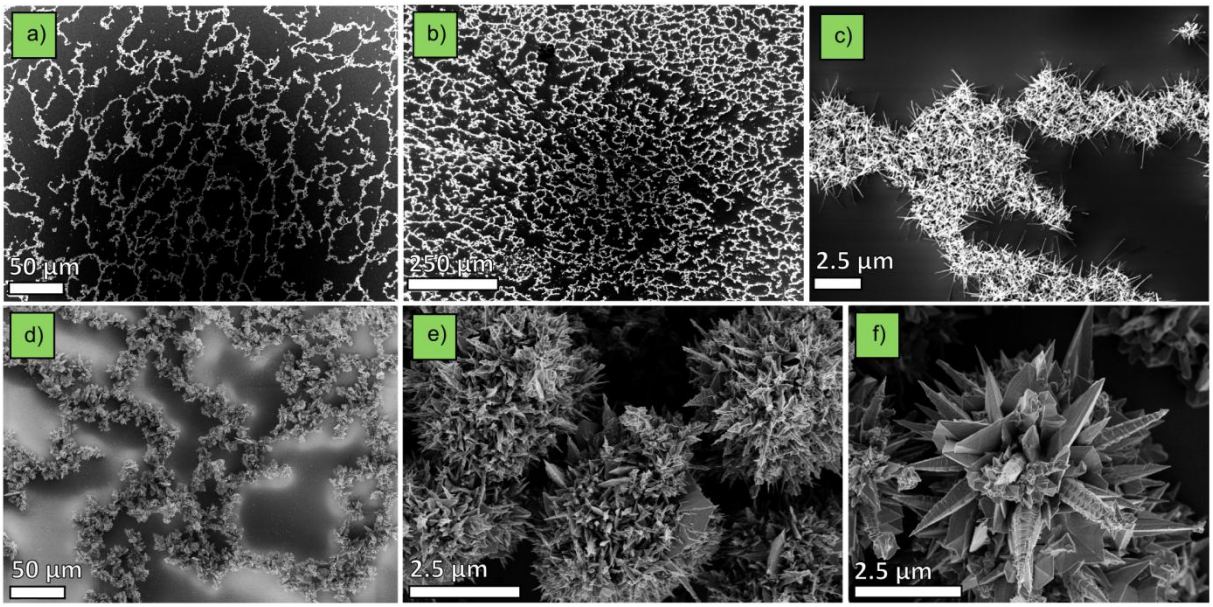

Figure 63 a) AuNP network deposited on a silicon plate. b, c) GaN nanowires obtained in the CVD process, utilizing AuNPs as a catalyst. GaN nanowires distribution repeats thus the pattern made of AuNPs. d) Platform after deposition of the AuMFs. Image with large distances between GaN chains was chosen to present preferential deposition of the AuMFs at the top of the GaN nanowires and not in the cavities in between. e, f) Morphology of the typical AuMFs achieved in the reaction with the presented solid substrate. Scale bars: a) 50 µm, b) 250 µm, c) 2.5 µm, d) 50 µm, e) 2.5 µm, f) 2.5 µm.

Analysis of the SEM images shown in Figure 63 allows the conclusion that the pattern formed at the beginning by the AuNPs is then repeated by GaN nanowires and the AuMFs. It is also clear that the new substrate affected the morphology of the AuMFs. The obtained AuMFs were built of sharper and more numerous gold structures than AuMFs presented in Figure 44. They were, however, uniform in size and shape and exhibited promising SERS-related properties, described in this section.

Studies of several types of AuNP distribution showed that full coverage of the silicon surface by GaN nanowires (like in Figure 62b-e) led to an almost inactive SERS platform. The decrease in coverage below 50% of the surface of the substrate made it

possible, however, to find a balance between SERS-sensitivity and mechanical stability. More detailed analysis for the low coverage, performed for the 1077 1/cm mode of the *p*-MBA, is presented in Figure 64. In Figure 64a stability as a percentage of EF on the 3rd day in comparison to initial EF is shown. Figure 64b presents EF observed for three different coverages and also for pure roughened silicon. As shown, coverage of the substrate at the level of 15% provides optimum mechanical stability and SERS-suitability (quantified by EF). Figure 64c shows a comparison of 1077 1/cm mode intensity between a typical SERS platform on roughened silicon ("old type") and a platform made of AuMFs immobilized on the 15% GaN netlike scaffold ("new type"). This experiment confirmed the superiority of the new platform over the old one. The AuMFs are immobilized better on the GaN scaffolding than on roughened silicon; the gold layer is thus mechanically stable in time and allows efficient SERS analysis for a long time.

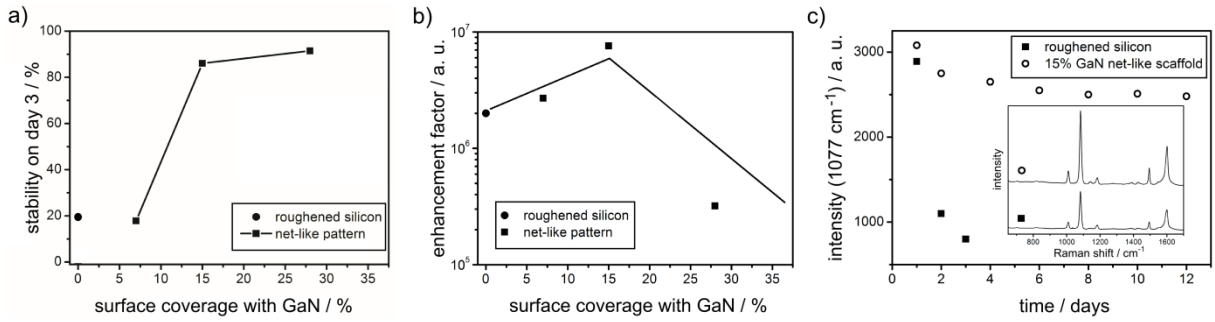

Figure 64 Comparison between SERS platforms on a GaN scaffolding and on roughened silicon; courtesy of Jan Paczesny.[87] Lines only show a trend. (a) Stability as a percentage of EF after 3 days of storage of plates in the solution of *p*-MBA, with respect to EF observed after 1 day. (b) EF calculated for three different coverages with GaN and for roughened silicon. (c) Intensity of the 1077 1/cm mode of samples stored in *p*-MBA solution, measured every 24 h. Inset: spectra collected after first 24 hours.

The enhancement factor of the new platform is also slightly better than for the old one and is 7.2×10^6. This may result from the new, more SERS-suitable morphology of the AuMFs. As was earlier mentioned, generally there are no simple algorithms in designing the best-enhancing SERS substrates. Probably, we still do not understand the mechanism of Raman signal enhancement well enough to design a platform perfectly fitting the requirements of this mechanism. The good result achieved for the new platform allowed however the conclusion that the spiky morphology of the AuMFs, probably obtained due to the presence of the gold alloy droplets on top of the GaN whiskers, promotes the formation of stronger electromagnetic fields and stronger plasmon resonances than typical, round-edged AuMFs. This could also answer the question why 15% of coverage with GaN gives the best EF. Beside the optimal

mechanical immobilization of the gold layer in this case, the morphology of the AuMFs obtained in the 15% content of GaN is probably better for SERS than the morphologies observed for other degrees of coverage.

After optimization of the design of the new platform, the reproducibility of SERS spectra was examined. The experiments were carried out for platforms having the following hierarchical structure:

1st layer – silicon plate,

2nd layer – GaN nanowires, coverage 15%,

3rd layer – AuMFs obtained from a *c*50(3:8) solution (with a height of the liquid column above the plate during the reaction of 1 cm).

A top view SEM image of the platform is shown in Figure 65a. As an analyte, a 10^{-6} M *p*-MBA solution was used. At the top of Figure 65b the spectra acquired at various positions on the same substrate and also on different substrates are presented. The spectra display high reproducibility of the modes, with only a slight variation in amplitude for some of the higher wavenumbers. Normalized second derivatives of the SERS spectra are shown in the lower part of Figure 65b. The almost complete overlap in features observed in the second derivative spectra indicated that differences in the SERS spectra were primarily caused by intensity and/or baseline variations. Parameter Γ was calculated as a cross-correlation between all the pairs of spectra; its average value was 0.87.

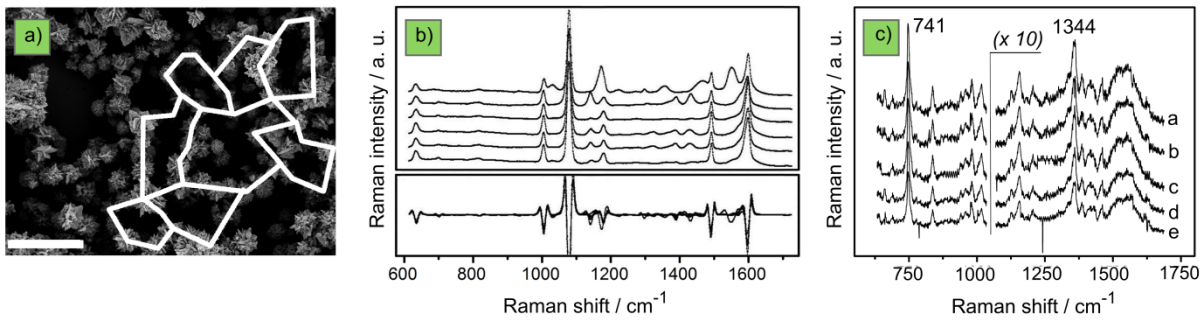

Figure 65 (a) SEM image of the AuMFs deposited on the substrate with 15% GaN coverage. The white lines indicate the net-like pattern repeated by the AuMFs. (b) SERS spectra collected from the six measurements (top) and the second derivative of SERS spectra (bottom). (c) SERS spectra of $ST_{20}N2$ sequence of DNA revealing the excellent reproducibility of the new platform. The 731 1/cm band is assigned to a breathing mode; the multicomponent band peak at 1330 1/cm is assigned to the mixed in-plane stretching motions of the skeleton vibration of a six-member ring. Spectra a, b, c, d, and e correspond to the analyte adsorbed for, respectively, 20 min, 1, 2 , 6 , and 36 h. All three graphs: courtesy of Jan Paczesny.[87]

The suitability of the new platform for biological analytes was also tested. In Figure 65c, SERS spectra recorded for a DNA oligomer $ST_{20}N2$ from a solution of a concentration 10^{-6} M are presented. The SERS measurements reaffirmed great sensivity

and repeatability of the new platform. The experiment also demonstrated the great time-related stability of the platform. The platform exhibited both mechanical stability and the ability to enhance the Raman signal for a long period from the start of the experiment (demonstrated earlier in Figure 64c), as well as having no impact on the quality of the spectra of the biological analyte. As presented in Figure 65c, the platform was immersed in the DNA solution for various times, up to 36 h, but the quality and intensity of the achieved Raman modes remained constant.

4.6.5 Conclusions

In this section I have presented various ways to obtain a new analytical platform for SERS. The simple self-assembly of the AuMFs on a scratched silicon plate led to the fabrication of the first useful platform for SERS-based chemical and biological sensing. The SERS spectra recorded for *p*-MBA and bacteriophage λ provided enhancement factors above 10^6, and exhibited excellent reproducibility both within single substrates and between different substrates. The fact that the platform allowed for detection of Raman bands of the bacteriophage's DNA is remarkable. It proves that the AuMF-functionalized substrates can be potentially employed for bioanalytical applications.

The modifications involving the change of the metallic coating (by halides or silver salt) did not bring satisfactory results – the fabricated platforms exhibited low enhancement of Raman modes and unsatisfactory mechanical stability. These experiments, however, provided information that, among all the types of metallic morphology described in section 4.5, the flowerlike ones are the most SERS-viable because they allow the achievement of enhanced and repeatable Raman spectra. I decided thus to use them on a modified solid substrate. Thanks to the cooperation with Jan Paczesny and Witold Adamkiewicz I succeeded in replacing a scratched silicon with a silicon plate partially covered with GaN nanowires. The completely new bottom-up procedure of preparation led to the fabrication of a functional surface of controllable morphology. This new technique, based on consecutive self-assembly steps, allowed the achievement of a sensitive, reproducible and extremely stable SERS platform.

5 Summary

The first thesis posed in this dissertation is that the addition of inorganic salt enables the arrangement of positively charged AuNPs into dense monolayers, thanks to the screening of the electrostatic repulsion. To confirm this statement, I investigated the deposition of these NPs onto negatively charged surfaces from solutions containing sodium chloride. The deposition process was studied for a wide range of salt concentrations, from 0 (no salt) up to 4.6 M. I found, that for the lowest content of salt, adsorption proceeds quickly, but gives low surface coverage resulting from the strong repulsion between adjacent AuNPs. For sufficiently high salt concentrations (about 0.6 M), the system becomes unstable and aggregation of the NPs occurs in bulk. This effect results from the screening of the electrostatic repulsion between the AuNPs. However, the NPs adsorb to form dense layers with surface coverage reaching about 50%. Unexpectedly, I found that the system regains its stability upon increasing the salt concentrations above 2.0 M. In this regime, adsorption takes place and the AuNPs form dense layers. Further increase in the ionic strength (above 4.0 M for NaCl) results in halting the adsorption process. These findings prove that the screening of electrostatic repulsions depends on the salt concentration, and thereby confirm the first thesis of this dissertation.

The second thesis postulates that the deposition of AuNPs on solid substrates leads to deformation of the AuNPs and that the level of distortion is related to the composition of the organic shell on the nanoparticle. In order to confirm this thesis, I studied the deposition of AuNPs coated with positively and negatively charged, as well as uncharged, ligands on the negatively charged substrate. I found that electrostatic forces between the ligand and substrate are strong enough to displace Au atoms within the core. In the process, the AuNPs underwent plastic deformations and took shapes that can be approximated as spherical caps. The strongest deformations (flattening) of the AuNP core were observed for positively charged ligands electrostatically attracted to the substrate. The smallest deformations occurred for the negatively charged coating repelled from the surface.

The third thesis also regards the morphological changes of AuNPs and postulates that during plasma treatment the AuNPs exhibit a liquid-like behavior and coalesce into larger objects according to the Smoluchowski Ripening mechanism. I conducted a series

of experiments in which AuNPs deposited on the silicon substrate were treated with oxygen plasma. Analysis of the SEM images of the AuNPs before and after this process led to the conclusion that plasma treatment affects the morphology of AuNPs in two ways. First, it makes them coarsen. Second, it changes also the shapes of individual particles. Specifically, I found that their shapes, flattened because of the deposition process, become more spherical, resembling droplets of a non-wetting liquid, and their contact angles increase from 54 degrees to about 123 degrees. These results indicate that during plasma treatment the particles exhibit a liquid-like behavior, with the ability to move on the substrate surface and coalesce. I also provided arguments that the growth of the AuNPs during the plasma treatment is dominated by the diffusion-collision mechanism, not by Oswald Ripening. To model the time evolution of the surface density of the droplets, I employed the mean-field Smoluchowski coagulation rate equation, and assumed the diffusivity of the droplet scales with its mass as $D(m) \sim m^{-\alpha}$. I found that the experimental data are in accord with the predictions of the Smoluchowski model, thus confirming the third thesis.

The last three theses regard the possibilities for the synthesis, modification, and immobilization of AuMFs and claim that it is possible to use deposited AuMFs as an analytical platform for SERS. The confirmation of these theses is the successful synthesis of the highly folded, branched microstructures of the flower-like morphology in the reaction of auric acid and hydroxylamine hydrochloride. The subsequent stages of the AuMFs' formation are studied and a mechanism for smoothing the "petals" is proposed. It is shown that the rounding of the AuMFs is a consequence of their reactivity toward acids and the presence of a reducing agent in the post-reaction mixture. In the dissertation I have also shown that it is possible to tailor the shape of AuMFs by changing the molar ratio of the reagents or thanks to various additives (like halides or silver salts) in the reaction mixture. I developed a method for immobilizing AuMFs on solid substrates by simple self-assembly and showed that AuMFs deposited on silicon, metal, or gallium nitride nanowires exhibit different morphologies. I also demonstrated that AuMFs so deposited can be used as efficient SERS platforms, providing an enhancement factor of the level of 10^6.

6 Sources of images

I. Top-down and bottom-up approach (page 27): Schmitz-Antoniak, C. X-ray absorption spectroscopy on magnetic nanoscale systems for modern applications. *Rep. Prog. Phys.* **2015**, *78*, 062501.

II. Optical properties of QDs (page 29). Source of the whole panel: Chou, K. F.; Dennis, A. M. Förster Resonance Energy Transfer between Quantum Dot Donors and Quantum Dot Acceptors. *Sensors* **2015**, *15* (6), 13288-13325.
Sources of the single images: (a) Han, M.; Gao, X.; Su, J. Z.; Nie, S. Quantum-dot-tagged microbeads for multiplexed optical coding of biomolecules. *Nat. Biotechnol.* **2001**, *19*, 631–635. (b) Cox, J. A quantum paintbox. *Chem. Brit.* **2003**, *39*, 21–25. (c) Ref. 23.

III. Brust-Schiffrin synthesis (page 36): Calandra, P.; Calogero, G.; Sinopoli, A.; Gucciardi, P. G. Metal nanoparticles and carbon-based nanostructures as advanced materials for cathode application in dye-sensitized solar cells. *Int. J. Photoenergy* **2010**, *2010*, 1–15.

IV. Hydrophobic and hydrophilic ligands drawn in scale on the 5 nm AuNP (page 43): Sperling, R. A.; Parak, W. J. Surface modification, functionalization and bioconjugation of colloidal inorganic nanoparticles. *Phil. Trans. R. Soc. A* **2010**, *368*, 1333–1383.

V. Schematic of SEM (page 56): the Encyclopedia Britannica website (http://www.britannica.com/technology/scanning-electron-microscope)

VI. Schematic of Zeta-potential (page 60): Wikipedia (https://en.wikipedia.org/wiki/ Zeta_potential)

7 References

[1] *Nanoscale Science and Technology*; Kelsall, R. W., Hamley, I. W., Geoghegan, M., Eds.; John Wiley: Chichester, England ; Hoboken, NJ, **2005**.

[2] Li, N.; Zhao, P.; Astruc, D. Anisotropic Gold Nanoparticles: Synthesis, Properties, Applications, and Toxicity. *Angew. Chem. Int. Ed.* **2014**, *53* (7), 1756–1789.

[3] (a) Pokropivny, V. V.; Skorokhod, V. V. Classification of nanostructures by dimensionality and concept of surface forms engineering in nanomaterial science. *Mat. Sci. Eng. C* **2007**, *27* (2007) 990–993. (b) Tiwari, J. N.; Tiwari, R. N.; Kim, K. S. Zero-dimensional, one-dimensional, two-dimensional and three-dimensional nanostructured materials for advanced electrochemical energy devices. *Prog. Mater. Sci.* **2012**, *57* (4), 724–803.

[4] Bangal, M.; Ashtaputre, S.; Marathe, S.; Ethiraj, A.; Hebalkar, N.; Gosavi, S. W.; Urban, J.; Kulkarni, S. K. Semiconductor nanoparticles. *Hyperfine Interact.* **2005**, *160*, 81–94.

[5] Mody, V. V.; Siwale, R.; Singh, A.; Mody, H. R. Introduction to Metallic Nanoparticles. *J. Pharm. Bioallied. Sci.* **2010**, *2* (4), 282–289.

[6] (a) Daniel, M.-C.; Astruc, D. Gold Nanoparticles: Assembly, Supramolecular Chemistry, Quantum-Size-Related Properties, and Applications toward Biology, Catalysis, and Nanotechnology. *Chem. Rev.* **2004**, *104* (1), 293–346. (b) Sardar, R.; Funston, A. M.; Mulvaney, P.; Murray, R. W. Gold Nanoparticles: Past, Present, and Future. *Langmuir* **2009**, *25* (24), 13840–13851. (c) Alexandridis, P. Gold Nanoparticle Synthesis, Morphology Control, and Stabilization Facilitated by Functional Polymers. *Chem. Eng. Technol.* **2011**, *34* (1), 15–28.

[7] Love, J. C.; Estroff, L. A.; Kriebel, J. K.; Nuzzo, R. G.; Whitesides, G. M. Self-assembled monolayers of thiolates on metals as a form of nanotechnology. *Chem. Rev.* **2005**, *105* (4), 1103–1170.

[8] Louis, C.; Pluchery, O. Gold Nanoparticles for Physics, Chemistry and Biology; World Scientific, **2012**.

[9] Salata, O. V. Applications of nanoparticles in biology and medicine. *J Nanobiotechnology* **2004**, *2*, 3.

[10] Jones, M.-C.; Leroux, J.-C. Polymeric micelles – a new generation of colloidal drug carriers. *Eur. J. Pharm. Biopharm.* **1999**, *48* (2), 101–111.

[11] Kamińska, A.; Witkowska, E.; Winkler, K.; Dzięcielewski, I.; Weyher, J. L.; Waluk, J. Detection of Hepatitis B virus antigen from human blood: SERS immunoassay in a microfluidic system. *Biosensors and Bioelectronics* **2015**, *66*, 461–467.

[12] (a) Bruchez, M.; Moronne, M.; Gin, P.; Weiss, S.; Alivisatos, A. P. Semiconductor nanocrystals as fluorescent biological labels. *Science* **1998**, *281*, 2013–2016. (b) Chan, W. C.W.; Nie, S. M. Quantum dot bioconjugates for ultrasensitive nonisotopic detection. *Science* **1998**, *281,* 2016–2018. (c) Wang, S.; Mamedova, N.; Kotov, N. A.; Chen, W.; Studer, J. Antigen/antibody immunocomplex from CdTe nanoparticle bioconjugates. *Nano Lett.* **2002**, *2*, 817–822.

[13] (a) Mah, C.; Zolotukhin, I.; Fraites, T. J.; Dobson, J.; Batich, C.; Byrne, B. J. Microsphere-mediated delivery of recombinant AAV vectors *in vitro* and *in vivo*. *Mol. Therapy* **2000**, *1*, 239. (b) Panatarotto, D.; Prtidos, C. D.; Hoebeke, J.; Brown, F.; Kramer, E.; Briand, J. P.; Muller, S.; Prato, M.; Bianco, A. Immunization with peptide-functionalized carbon nanotubes enhances virus-specific neutralizing antibody responses. *Chem. Biol.* **2003**, *10*, 961–966.

[14] Edelstein, R. L.; Tamanaha, C. R.; Sheehan, P. E.; Miller, M. M.; Baselt, D. R.; Whitman, L. J.; Colton, R. J. The BARC biosensor applied to the detection of biological warfare agents. *Biosens. Bioelectron* **2000**, *14*, 805–813.

[15] Nam, J. M.; Thaxton C. C.; Mirkin C. A. Nanoparticles-based bio-bar codes for the ultrasensitive detection of proteins. *Science* **2003**, *301*, 1884–1886.

[16] Mahtab, R.; Rogers, J. P.; Murphy, C. J. Protein-sized quantum dot luminescence can distinguish between "straight", "bent", and "kinked" oligonucleotides. *J. Am. Chem. Soc.* **1995**, *117*, 9099–9100.

[17] (a) Ma, J.; Wong, H.; Kong, L. B.; Peng, K. W.; Biomimetic processing of nanocrystallite bioactive apatite coating on titanium. *Nanotechnology* **2003**, *14*, 619–623. (b) de la Isla, A.; Brostow, W.; Bujard, B.; Estevez, M.; Rodriguez, J. R.; Vargas, S.; Castano, V. M. Nanohybrid scratch resistant coating for teeth and bone viscoelasticity manifested in tribology. *Mat. Resr. Innovat.* **2003**, *7* 110–114.

[18] Yoshida, J.; Kobayashi, T. Intracellular hyperthermia for cancer using magnetite cationic liposomes. *J. Magn. Magn. Mater.* **1999**, *194*, 176–184.

[19] Molday, R. S.; MacKenzie, D. Immunospecific ferromagnetic iron dextran reagents for the labeling and magnetic separation of cells. *J. Immunol. Methods* **1982**, *52*, 353–367.

[20] Weissleder, R.; Elizondo, G.; Wittenburg, J.; Rabito, C. A.; Bengele, H. H.; Josephson, L. Ultrasmall superparamagnetic iron oxide: characterization of a new class of contrast agents for MR imaging. *Radiology* **1990**, *175*, 489–493.

[21] Parak, W. J.; Boudreau, R.; Gros, M. L.; Gerion, D.; Zanchet, D.; Micheel, C. M.; Williams, S. C.; Alivisatos, A. P.; Larabell, C. A. Cell motility and metastatic potential studies based on quantum dot imaging of phagokinetic tracks. *Adv. Mater.* **2002**, *14*, 882–885.

[22] *Nanoscale Materials in Chemistry*, 2nd ed.; Klabunde, K. J., Richards, R., Eds.; Wiley: Hoboken, N.J, **2009**.

[23] Smith, A. M.; Nie, S. Semiconductor nanocrystals: structure, properties, and band gap engineering. *Acc. Chem. Res.* **2010**, *43* (2), 190–200.

[24] Alivisatos, A. P. Semiconductor clusters, nanocrystals and quantum dots. *Science* **1996**, New Series, *271* (5251), 933–937.

[25] Kosyachenko. L. A. *Solar Cells - New Approaches and Reviews*; Chapter 11, InTech, **2015**.

[26] Lin C.; Tao K.; Hua, D.; Ma, Z.; Zhou, S. Size Effect of Gold Nanoparticles in Catalytic Reduction of *p*-Nitrophenol with $NaBH_4$. *Molecules* **2013**, *18*, 12609–12620.

[27] Zhou, X.; Xu, W.; Liu, G.; Panda, D.; Cheng, P. Size-Dependent Catalytic Activity and Dynamics of Gold Nanoparticles at the Single-Molecule Level. *J. Am. Chem. Soc.* **2010**, *132*, 138–146.

[28] Carbert, J. Gold-Based Enamel Colours. *Gold Bull* **1980**, *13* (4), 144–150.

[29] Lopez, N.; Janssens, T. V. W.; Clausen, B. S.; Xu, Y.; Mavrikakis, M.; Bligaard, T.; Nørskov, J. K. On the origin of the catalytic activity of gold nanoparticles for low-temperature CO oxidation. *Journal of Catalysis* **2004**, *223*, 232–235.

[30] Schubert, M. M.; Hackenberg, S.; van Veen, A. C.; Muhler, M.; Plzak, V.; Behm, R. J. CO Oxidation over Supported Gold Catalysts – Inert and Active Support Materials and Their Role for the Oxygen Supply during Reaction. *J. Catal*. **2001**, *197*, 113–122.

[31] Turkevich, J.; Stevenson, P. C.; Hillier, J. A Study of the Nucleation and Growth Processes in the Synthesis of Colloidal Gold. *Discuss. Faraday Soc.* **1951**, *11* (0), 55–75.

[32] Frens, G. Controlled Nucleation for the Regulation of the Particle Size in Monodisperse Gold Suspensions. *Nature* **1973**, *241* (105), 20–22.

[33] (a) Navarro, J. R. G.; Lerouge, F.; Cepraga, C.; Micouin, G.; Favier, A.; Chateau, D.; Charreyre, M.-T.; Lanoë, P.-H.; Monnereau, C.; Chaput, F.; Marotte, S.; Leverrier, Y.; Marvel, J.; Kamada, K.; Andraud, C.; Baldeck, P. L.; Parola, S. Nanocarriers with Ultrahigh Chromophore Loading for Fluorescence Bio-Imaging and Photodynamic Therapy. *Biomaterials* **2013**, *34* (33), 8344–8351; (b) Kimling, J.; Maier, M.; Okenve, B.; Kotaidis, V.; Ballot, H.; Plech, A. Turkevich Method for Gold Nanoparticle Synthesis Revisited. *J. Phys. Chem. B* **2006**, *110* (32), 15700–15707; (c) Sivaraman, S. K.; Kumar, S.; Santhanam, V. Monodisperse Sub-10 Nm Gold Nanoparticles by Reversing the Order of Addition in Turkevich Method – The Role of Chloroauric Acid. *Journal of Colloid and Interface Science* **2011**, *361* (2), 543–547; (d) Zabetakis, K.; Ghann, W. E.; Kumar, S.; Daniel, M.-C. Effect of High Gold Salt Concentrations on the Size and Polydispersity of Gold Nanoparticles Prepared by an Extended Turkevich–Frens Method. *Gold Bull* **2012**, *45* (4), 203–211; (e) Schulz, F.; Homolka, T.; Bastús, N. G.; Puntes, V.; Weller, H.; Vossmeyer, T.

Little Adjustments Significantly Improve the Turkevich Synthesis of Gold Nanoparticles. *Langmuir* **2014**, *30* (35), 10779–10784.

[34] Brust, M.; Walker, M.; Bethell, D.; Schiffrin, D. J.; Whyman, R. Synthesis of Thiol-Derivatised Gold Nanoparticles in a Two-Phase Liquid–Liquid System. *J. Chem. Soc., Chem. Commun.* **1994**, No. 7, 801–802.

[35] Grzelczak, M.; Pérez-Juste, J.; Mulvaney, P.; Liz-Marzán, L. M. Shape Control in Gold Nanoparticle Synthesis. *Chem. Soc. Rev.* **2008**, *37* (9), 1783–1791.

[36] Liu, M.; Guyot-Sionnest, P. Mechanism of silver(I)-Assisted Growth of Gold Nanorods and Bipyramids. *J Phys Chem B* **2005**, *109* (47), 22192–22200.

[37] Ha, T. H.; Koo, H.-J.; Chung, B. H. Shape-Controlled Syntheses of Gold Nanoprisms and Nanorods Influenced by Specific Adsorption of Halide Ions. *J. Phys. Chem. C* **2007**, *111*, 1123–1130.

[38] Barnard, A. S.; Curtiss, L. A. Predicting the Shape and Structure of Face-Centered Cubic Gold Nanocrystals Smaller than 3 Nm. *Chemphyschem* **2006**, *7* (7), 1544–1553.

[39] Barnard, A. S.; Young, N. P.; Kirkland, A. I.; van Huis, M. A.; Xu, H. Nanogold: A Quantitative Phase Map. *ACS Nano* **2009**, *3* (6), 1431–1436.

[40] Barnard, A. S. Direct Comparison of Kinetic and Thermodynamic Influences on Gold Nanomorphology. *Acc. Chem. Res.* **2012**, *45* (10), 1688–1697.

[41] Ide, M. S.; Davis, R. J. The Important Role of Hydroxyl on Oxidation Catalysis by Gold Nanoparticles. *Acc. Chem. Res.* **2014**, *47* (3), 825–833.

[42] Wybrańska, K.; Paczesny, J.; Serejko, K.; Sura, K.; Włodyga, K.; Dzięcielewski, I.; Jones, S. T.; Śliwa, A.; Wybrańska, I.; Hołyst, R.; Scherman, O. A.; Fiałkowski, M. Gold–Oxoborate Nanocomposites and Their Biomedical Applications. *ACS Appl. Mater. Interfaces* **2015**, *7* (7), 3931–3939.

[43] (a) Whetten, R. L.; Price, R. C. Nano-Golden Order. *Science* **2007**, *318*, 407–408; (b) Bürgi, T. Properties of the gold-sulfur interface: from self-assembled monolayers to clusters. *Nanoscale* **2015**, *7*, 15553–15567. (c) Pensa, E.; Cortés, E.; Corthey, G.; Carro, P.; Vericat, C.; Fonticelli, M. H.; Benítez, G.; Rubert, A. A.; Salvarezza, R. C. The Chemistry of the Sulfur-Gold Interface: In Search of a Unified Model. *Acc. Chem. Res.* **2012**, *45* (8), 1183–1192; (d) Häkkinen, H. The gold-sulfur interface at the nanoscale. *Nat. Chem.* **2012**, *4*, 443–455. (e) Jadzinsky, P. D.; Calero, G.; Ackerson, C. J.; Bushnell, D. A.; Kornberg, R. D. Strucyure of a Thiol Monolayer-Protected Gold Nanoparticle at 1.1 Å Resolution. *Science*, **2007**, *318*, 430–433.

[44] *Comprehensive Handbook of Chemical Bond Energies*; Luo, Y. R.; CRC Press, Boca Raton, FL, **2007**.

[45] Imabayashi, S.; Hobara, D.; Kakiuchi, T. Voltammetric Detection of the Surface Diffusion of Adsorbed Thiolate Molecules in Artificially Phase-Separated Binary Self-Assembled Monolayers on a Au(111) Surface. *Langmuir* **2001**, *17*, 2560–2563.

[46] Zhao, Y.; Jiang, X. Multiple strategies to activate gold nanoparticles as antibiotics. *Nanoscale* **2013**, *5*, 8340–8350.

[47] Huo, S.; Jiang, Y.; Gupta, A.; Jiang, Z.; Landis, R. F.; Hou, S.; Liang, X.-J.; Rotello, V. M. Fully Zwitterionic Nanoparticle Antimicrobial Agents through Tuning of Core Size and Ligand Structure. *ACSNano* **2016**, *10*, 8732–8737.

[48] Pillai, P. P.; Kowalczyk, B.; Kandere-Grzybowska, K.; Borkowska, M.; Grzybowski, B. A. Engineering Gram Selectivity of Mixed-Charge Gold Nanoparticles by Tuning the Balance of Surface Charges. *Angew. Chem. Int. Ed.* **2016**, *55* (30), 8610–8614.

[49] Ibsen, S.; Sonnenberg, A.; Schutt, C.; Mukthavaram, R.; Yeh, Y.; Ortac, I.; Manouchehri, S.; Kesari, S.; Esener, S.; Heller, M. J. Nanoparticles: Recovery of Drug Delivery Nanoparticles from Human Plasma Using an Electrokinetic Platform Technology. *Small* **2015**, *11* (38), 5088–5096.

[50] (a) Kalsin, A. M.; Fialkowski, M.; Paszewski, M.; Smoukov, S. K.; Bishop, K. J. M.; Grzybowski, B. A. Electrostatic Self-Assembly of Binary Nanoparticle Crystals with a Diamond-Like Lattice. Science 2006, 312 (5772), 420–424; (b) Pillai, P. P.; Kowalczyk, B.; Grzybowski, B. A. Self-assembly of like-charged nanoparticles into microscopic crystals. *Nanoscale* **2016**, *8*, 157–161; (c) Bishop, K. J. M.; Grzybowski,

B. A. "Nanoions": Fundamental Properties and Analytical Applications of Charged Nanoparticles. *ChemPhysChem* **2007**, *8* (15), 2171–2176.

[51] (a) Singh, R.; Lillard, J. W. Nanoparticle-Based Targeted Drug Delivery. *Exp. Mol. Pathol.* **2009**, *86* (3), 215–223; (b) Jain, P. K.; El-Sayed, I. H.; El-Sayed, M. A. Au Nanoparticles Target Cancer. *Nano Today* **2007**, *2* (1), 18–29; (c) Murphy, C. J.; Gole, A. M.; Stone, J. W.; Sisco, P. N.; Alkilany, A. M.; Goldsmith, E. C.; Baxter, S. C. Gold Nanoparticles in Biology: Beyond Toxicity to Cellular Imaging. *Acc. Chem. Res.* **2008**, *41* (12), 1721–1730.

[52] Njoki, P. N.; Lim, I.-I. S.; Mott, D.; Park, H.-Y.; Khan, B.; Mishra, S.; Sujakumar, R.; Luo, J.; Zhong, C.-J. Size Correlation of Optical and Spectroscopic Properties for Gold Nanoparticles. *J. Phys. Chem. C* **2007**, *111* (40), 14664–14669.

[53] (a) Rodríguez-Lorenzo, L.; Alvarez-Puebla, R. A.; Garcia de Abajo, F. J.; Liz-Marzan, L. M. Surface Enhanced Raman Scattering Using Star-Shaped Gold Colloidal Nanoparticles. *J. Phys. Chem. C* **2010**, *114*, 7336–7340. (b) Zhu, S.; Cortie, M.; Blakey, I. Effect of Multimodal Plasmon Resonances on the Optical Properties of Five-pointed Nanostars. *Nanomaterials and Nanotechnology* **2015**, *5* (38), DOI: 10.5772/60726.

[54] (a) Alvarez-Puebla, R. A.; Liz-Marzan, L. M.; Garcia de Abajo, F. J. Light Concentration at the Nanometer Scale. *Phys. Chem. Lett* **2010**, *1*, 2428–2434. (b) Enoch, S.; Quidant, R.; Badenes, G. *Opt. Express* **2004**, *12*, 3422–3427. (c) Stoerzinger, K. A.; Lin, J. Y.; Obom, T. W. Nanoparticle SERS substrates with 3D Raman-active volumes. *Chem. Sci.***2011**, *2*, 1435–1439.

[55] Li, L.; Hutter, T.; Steiner, U.; Mahajan, S. Single molecule SERS and detection of biomolecules with a single gold nanoparticle on a mirror junction. *Analyst* **2013**,*138*, 4574-4578.

[56] Whitesides, G. M.; Grzybowski, B. Self-assembly at all scales. Science 2002, 295, 2418–2421.

[57] Bishop, K. J. M.; Wilmer, C. E.; Soh, S.; Grzybowski, B. A. Nanoscale Forces and Their Uses in Self-Assembly. *Small* **2009**, *5* (14), 1600–1630.

[58] Sashuk, V.; Winkler, K.; Żywociński, A.; Wojciechowski, T.; Górecka, E.; Fiałkowski, M. Nanoparticles In a Capillary Trap: Dynamic Self-Assembly at Fluid Interfaces. *ACS Nano* **2013**, *7* (10), 8833–8839.

[59] Fialkowski, M.; Bishop, K. J. M.; Klajn, R.; Smoukov, S. K.; Campbell, C. J.; Grzybowski, B. A. Principles and Implementations of Dissipative (Dynamic) Self-Assembly. *J. Phys. Chem. B* **2006**, *110*, 2482–2496.

[60] Wang, L.; Xu, L.; Kuang, K.; Xu, C.; Kotov, N. A. Dynamic Nanoparticle Assemblies. *Acc. Chem. Res.* **2012**, *45* (11), 1916–1926.

[61] Grzelczak, M.; Vermant, J.; Furst, E. M.; Liz-Marzan, L. M. Directed self-assembly of Nanoparticles. *ACS NANO* **2010**, *4* (7), 3591–3605.

[62] Pickering, S. U. Emulsions. *J. Chem. Soc.* **1907**, *91*, 2001–2021.

[63] Lin, Y.; Skaff, H.; Emrick, T.; Dinsmore, A. D.; Russel, T. P. Nanoparticle Assembly and Transport at Liquid-Liquid Interfaces. *Science* **2003**, *229* (5604), 226–229.

[64] Baker, J. L.; Widmer-Cooper, A.; Toney, M. F.; Geissler, P. L.; Alivisatos, A. P. Device-Scale Perpendicular Alignment of Colloidal Nanorods. *Nano Lett.* **2010**, *10* (1), 195–201.

[65] Mittal, M.; Furst, E. M. Electric Field-directed convective assembly of ellipsoidal colloidal particles to create optically and mechanically anisotropic thin films. *Adv. Funct. Mater.* **2009**, *19*, 3271–3278.

[66] Ding, T.; Song, K.; Clays, K.; Tung, C. Fabrication of 3D Photonic Crystals of Ellipsoids: Convective Self-Assembly in Magnetic Field. *Adv. Matter.* **2009**, *21*, 1936–1940.

[67] Smith, B. D.; Kirby, D. J.; Keating, C. D. Vertical Arrays of Anisotropic Particles by Gravity-Driven Self-Assembly. *Small* **2011**, *7* (6), 781–787.

[68] Kiely, C. J.; Fink, J.; Zheng, J. G.; Brust, M.; Bethell, D.; Schiffrin, D. J. Ordered Colloidal Nanoalloys. *Adv. Mater.* **2000**, *12* (9), 640–643.

[69] Lin, X. M.; Jaeger, H. M.; Sorensen, C. M.; Klabunde, K. J. Formation of Long-Range-Ordered Nanocrystal Superlattices on Silicon Nitride Substrates. *J. Phys. Chem. B* **2001**, *105* (17), 3353–3357.

[70] Coe-Sullivan, S.; Steckel, J. S.; Woo, W.-K.; Bawendi, M. G.; Bulović, V. Large-Area Ordered Quantum-Dot Monolayers via Phase Separation During Spin-Casting. *Adv. Funct. Mater.* **2005**, *15* (7), 1117–1124.

[71] Chen, J.; Chan, Y.-H.; Yang, T.; Wark, S. E.; Son, D. H.; Batteas, J. D. Spatially Selective Optical Tuning of Quantum Dot Thin Film Luminescence. *J. Am. Chem. Soc.* **2009**, *131* (51), 18204–18205.

[72] Talapin, D. V.; Lee, J.-S.; Kovalenko, M. V.; Shevchenko, E. V. Prospects of Colloidal Nanocrystals for Electronic and Optoelectronic Applications. *Chem. Rev.* **2010**, *110* (1), 389–458.

[73] Gur, I.; Fromer, N. A.; Geier, M. L.; Alivisatos, A. P. Air-Stable All-Inorganic Nanocrystal Solar Cells Processed from Solution. *Science* **2005**, *310* (5747), 462–465.

[74] Anker, J. N.; Hall, W. P.; Lyandres, O.; Shah, N. C.; Zhao, J.; Van Duyne, R. P. Biosensing with Plasmonic Nanosensors. *Nat Mater* **2008**, *7* (6), 442–453.

[75] Paul, S.; Pearson, C.; Molloy, A.; Cousins, M. A.; Green, M.; Kolliopoulou, S.; Dimitrakis, P.; Normand, P.; Tsoukalas, D.; Petty, M. C. Langmuir–Blodgett Film Deposition of Metallic Nanoparticles and Their Application to Electronic Memory Structures. *Nano Lett.* **2003**, *3* (4), 533–536.

[76] Kolasinski, K. W. Catalytic Growth of Nanowires: Vapor–liquid–solid, Vapor–solid–solid, Solution–liquid–solid and Solid–liquid–solid Growth. *Current Opinion in Solid State and Materials Science* **2006**, *10* (3–4), 182–191.

[77] Lesniewski, A.; Paszewski, M.; Opallo, M. Gold–carbon Three Dimensional Film Electrode Prepared from Oppositely Charged Conductive Nanoparticles by Layer-by-Layer Approach. *Electrochemistry Communications* **2010**, *12* (3), 435–437.

[78] Shen, G. X.; Chen, Y. C.; Lin, C. J. Corrosion Protection of 316 L Stainless Steel by a TiO2 Nanoparticle Coating Prepared by Sol–gel Method. *Thin Solid Films* **2005**, *489* (1–2), 130–136.

[79] Prevo, B. G.; Hwang, Y.; Velev, O. D. Convective Assembly of Antireflective Silica Coatings with Controlled Thickness and Refractive Index. *Chem. Mater.* **2005**, *17* (14), 3642–3651.

[80] Haynes, C. L.; Van Duyne, R. P. Nanosphere Lithography: A Versatile Nanofabrication Tool for Studies of Size-Dependent Nanoparticle Optics. *J. Phys. Chem. B* **2001**, *105* (24), 5599–5611.

[81] Lee, S.; Drwiega, J.; Wu, C.-Y.; Mazyck, D.; Sigmund, W. M. Anatase TiO2 Nanoparticle Coating on Barium Ferrite Using Titanium Bis-Ammonium Lactato Dihydroxide and Its Use as a Magnetic Photocatalyst. *Chem. Mater.* **2004**, *16* (6), 1160–1164.

[82] Thebault, P.; Taffin de Givenchy, E.; Levy, R.; Vandenberghe, Y.; Guittard, F.; Géribaldi, S. Preparation and Antimicrobial Behaviour of Quaternary Ammonium Thiol Derivatives Able to Be Grafted on Metal Surfaces. *Eur J Med Chem* **2009**, *44* (2), 717–724.

[83] Jana, N. R.; Peng, X. Single-Phase and Gram-Scale Routes toward Nearly Monodisperse Au and Other Noble Metal Nanocrystals. *J. Am. Chem. Soc.* **2003**, *125* (47), 14280–14281.

[84] Winkler, K.; Paszewski, M.; Kalwarczyk, T.; Kalwarczyk, E.; Wojciechowski, T.; Gorecka, E.; Pociecha, D.; Holyst, R.; Fialkowski, M. Ionic Strength-Controlled Deposition of Charged Nanoparticles on a Solid Substrate. *J. Phys. Chem. C* **2011**, *115* (39), 19096–19103.

[85] Winkler, K.; Wojciechowski, T.; Liszewska, M.; Górecka, E.; Fiałkowski, M. Morphological Changes of Gold Nanoparticles due to Adsorption onto Silicon Substrate and Oxygen Plasma Treatment. *RSC Adv.* **2014**, *4* (25), 12729–12736.

[86] Winkler, K.; Kaminska, A.; Wojciechowski, T.; Holyst, R.; Fialkowski, M. Gold Micro-Flowers: One-Step Fabrication of Efficient, Highly Reproducible Surface-Enhanced Raman Spectroscopy Platform. *Plasmonics* **2011**, *6* (4), 697–704.

[87] Paczesny, J.; Kamińska, A.; Adamkiewicz, W.; Winkler, K.; Sozanski, K.; Wadowska, M.; Dziecielewski, I.; Holyst, R. Three Steps of Hierarchical Self Assembly Toward a Stable and Efficient Surface Enhanced Raman Spectroscopy Platform. *Chem. Mater.* **2012**, *24* (19), 3667–3673.

[88] Quinn, B. M.; Dekker, C.; Lemay, S. G. Electrodeposition of Noble Metal Nanoparticles on Carbon Nanotubes. *J. Am. Chem. Soc.* **2005**, *127* (17), 6146–6147.

[89] Lidgi-Guigui, N.; Dablemont, C.; Veautier, D.; Viau, G.; Seneor, P.; Nguyen Van Dau, F.; Mangeney, C.; Vaurès, A.; Deranlot, C.; Friederich, A. Grafted 2D Assembly of Colloidal Metal Nanoparticles for Application as a Variable Capacitor. *Advanced Materials* **2007**, *19* (13), 1729–1733.

[90] Kim, L.; Anikeeva, P. O.; Coe-Sullivan, S. A.; Steckel, J. S.; Bawendi, M. G.; Bulović, V. Contact Printing of Quantum Dot Light-Emitting Devices. *Nano Lett.* **2008**, *8* (12), 4513–4517.

[91] Fan, H.; Wright, A.; Gabaldon, J.; Rodriguez, A.; Brinker, C. J.; Jiang, Y.-B. Three-Dimensionally Ordered Gold Nanocrystal/Silica Superlattice Thin Films Synthesized via Sol–Gel Self-Assembly. *Adv. Funct. Mater.* **2006**, *16* (7), 891–895.

[92] Smoukov, S. K.; Bishop, K. J. M.; Kowalczyk, B.; Kalsin, A. M.; Grzybowski, B. A. Electrostatically "Patchy" Coatings via Cooperative Adsorption of Charged Nanoparticles. *J. Am. Chem. Soc.* **2007**, *129* (50), 15623–15630.

[93] Brouwer, E. A. M.; Kooij, E. S.; Wormeester, H.; Poelsema, B. Ionic Strength Dependent Kinetics of Nanocolloidal Gold Deposition. *Langmuir* **2003**, *19* (19), 8102–8108.

[94] (a) Lvov, Y.; Ariga, K.; Onda, M.; Ichinose, I.; Kunitake, T. Alternate Assembly of Ordered Multilayers of SiO2 and Other Nanoparticles and Polyions. *Langmuir* **1997**, *13* (23), 6195–6203; (b) Sennerfors, T.; Bogdanovic, G.; Tiberg, F. Formation, Chemical Composition, and Structure of Polyelectrolyte–Nanoparticle Multilayer Films. *Langmuir* **2002**, *18* (16), 6410–6415; (c) Ghannoum, S.; Xin, Y.; Jaber, J.; Halaoui, L. I. Self-Assembly of Polyacrylate-Capped Platinum Nanoparticles on a Polyelectrolyte Surface: Kinetics of Adsorption and Effect of Ionic Strength and Deposition Protocol. *Langmuir* **2003**, *19* (11), 4804–4811.

[95] Jain, P. K.; El-Sayed, M. A. Universal Scaling of Plasmon Coupling in Metal Nanostructures: Extension from Particle Pairs to Nanoshells. *Nano Lett.* **2007**, *7* (9), 2854–2858.

[96] Kelly, K. L.; Coronado, E.; Zhao, L. L.; Schatz, G. C. The Optical Properties of Metal Nanoparticles: The Influence of Size, Shape, and Dielectric Environment. *J. Phys. Chem. B* **2003**, *107* (3), 668–677.

[97] Zhao, L.; Kelly, K. L.; Schatz, G. C. The Extinction Spectra of Silver Nanoparticle Arrays: Influence of Array Structure on Plasmon Resonance Wavelength and Width. *J. Phys. Chem. B* **2003**, *107* (30), 7343–7350.

[98] Haynes, C. L.; McFarland, A. D.; Zhao, L.; Van Duyne, R. P.; Schatz, G. C.; Gunnarsson, L.; Prikulis, J.; Kasemo, B.; Käll, M. Nanoparticle Optics: The Importance of Radiative Dipole Coupling in Two-Dimensional Nanoparticle Arrays. *J. Phys. Chem. B* **2003**, *107* (30), 7337–7342.

[99] Bouhelier, A.; Bachelot, R.; Im, J. S.; Wiederrecht, G. P.; Lerondel, G.; Kostcheev, S.; Royer, P. Electromagnetic Interactions in Plasmonic Nanoparticle Arrays. *J. Phys. Chem. B* **2005**, *109* (8), 3195–3198.

[100] Chen, C.-F.; Tzeng, S.-D.; Chen, H.-Y.; Lin, K.-J.; Gwo, S. Tunable Plasmonic Response from Alkanethiolate-Stabilized Gold Nanoparticle Superlattices: Evidence of Near-Field Coupling. *J. Am. Chem. Soc.* **2008**, *130* (3), 824–826.

[101] Adamczyk, Z. Particle Adsorption and Deposition: Role of Electrostatic Interactions. *Advances in Colloid and Interface Science* **2003**, *100–102*, 267–347.

[102] Brouwer, E. A. M.; Kooij, E. S.; Hakbijl, M.; Wormeester, H.; Poelsema, B. Deposition Kinetics of Nanocolloidal Gold Particles. *Colloids and Surfaces A: Physicochemical and Engineering Aspects* **2005**, *267* (1–3), 133–138.

[103] Adamczyk, Z.; Zembala, M.; Siwek, B.; Warszyński, P. Structure and Ordering in Localized Adsorption of Particles. *Journal of Colloid and Interface Science* **1990**, *140* (1), 123–137.

[104] Adamczyk, Z.; Senger, B.; Voegel, J.-C.; Schaaf, P. Irreversible Adsorption/deposition Kinetics: A Generalized Approach. *The Journal of Chemical Physics* **1999**, *110* (6), 3118–3128.

[105] Kim, K.; Ryoo, H.; Lee, Y. M.; Shin, K. S. Adsorption Characteristics of Au Nanoparticles onto poly(4-Vinylpyridine) Surface Revealed by QCM, AFM, UV/vis, and Raman Scattering Spectroscopy. *Journal of Colloid and Interface Science* **2010**, *342* (2), 479–484.

[106] Wang, P.; Anderko, A. Computation of Dielectric Constants of Solvent Mixtures and Electrolyte Solutions. *Fluid Phase Equilibria* **2001**, *186* (1–2), 103–122.

[107] Israelachvili, J. N.; McGuiggan, P. M. Forces Between Surfaces in Liquids. *Science* **1988**, *241* (4867), 795–800.

[108] (a) Bolt, G. H. Determination of the Charge Density of Silica Sols. *J. Phys. Chem.* **1957**, *61* (9), 1166–1169; (b) Tadros, T. F.; Lyklema, J. Adsorption of Potential-Determining Ions at the Silica-Aqueous Electrolyte Interface and the Role of Some Cations. *J Electroanal Chem Interfacial Electrochem* **1968**, *17* (3–4), 267–275.

[109] Smoluchowski, M. Z. Veruch Einer Mathemtischen Theorie Der Koagulations Kinetic Kolloider Lousungen. *Zeitschrift fuer physikalische Chemie* **1917**, *92*, 129–136.

[110] Shipway, A. N.; Katz, E.; Willner, I. Nanoparticle Arrays on Surfaces for Electronic, Optical, and Sensor Applications. *ChemPhysChem* **2000**, *1* (1), 18–52.

[111] Koo, J.-M.; Lee, J.-B.; Moon, Y.; Moon, W.-C.; Jung, S.-B. Atmospheric Pressure Plasma Cleaning of Gold Flip Chip Bump for Ultrasonic Flip Chip Bonding. *J. Phys.: Conf. Ser.* **2008**, *100* (1), 012034; Gun, J.; Gutkin, V.; Lev, O.; Boyen, H.-G.; Saitner, M.; Wagner, P.; D'Olieslaeger, M.; Abouzar, M. H.; Poghossian, A.; Schöning, M. J. Tracing Gold Nanoparticle Charge by Electrolyte–Insulator–Semiconductor Devices. *J. Phys. Chem. C* **2011**, *115* (11), 4439–4445; Raiber, K.; Terfort, A.; Benndorf, C.; Krings, N.; Strehblow, H.-H. Removal of Self-Assembled Monolayers of Alkanethiolates on Gold by Plasma Cleaning. *Surface Science* **2005**, *595* (1–3), 56–63.

[112] Gun, J.; Rizkov, D.; Lev, O.; Abouzar, M. H.; Poghossian, A.; Schöning, M. J. Oxygen Plasma-Treated Gold Nanoparticle-Based Field-Effect Devices as Transducer Structures for Bio-Chemical Sensing. *Microchim Acta* **2008**, *164* (3-4), 395–404.

[113] Llorca, J.; Casanovas, A.; Domínguez, M.; Casanova, I.; Angurell, I.; Seco, M.; Rossell, O. Plasma-Activated Core-Shell Gold Nanoparticle Films with Enhanced Catalytic Properties. *J Nanopart Res* **2007**, *10* (3), 537–542.

[114] Fahmi, A.; D'Aléo, A.; Williams, R. M.; De Cola, L.; Gindy, N.; Vögtle, F. Converting Self-Assembled Gold Nanoparticle/Dendrimer Nanodroplets into Horseshoe-like Nanostructures by Thermal Annealing. *Langmuir* **2007**, *23* (14), 7831–7835; Y. Maeda, T. A. Nanoparticle Arrangement by DNA-Programmed Self-Assembly for Catalyst Applications. *Journal of Applied Physics* **2010**, *108* (9), 094326–094326 – 4.

[115] Ojima, K.; Takagi, A.; Yamada, F.; Matsumoto, T.; Kawai, T. Immobilizing Metal Nanoparticles. 20100233384, September 16, 2010.

[116] Jaramillo, T. F.; Baeck, S.-H.; Cuenya, B. R.; McFarland, E. W. Catalytic Activity of Supported Au Nanoparticles Deposited from Block Copolymer Micelles. *J. Am. Chem. Soc.* **2003**, *125* (24), 7148–7149; Onoue, S.; He, J.; Kunitake, T. Fabrication of Gold Nanosheet and Nanowire by Oxygen Plasma Induced Fusion of Densely Arrayed Nanoparticles. *Chemistry Letters* **2006**, *35* (2), 214–215.

[117] Voorhees, P. W. The Theory of Ostwald Ripening. *J Stat Phys* **1985**, *38* (1-2), 231–252; Lifshitz, I. M.; Slyozov, V. V. The Kinetics of Precipitation from Supersaturated Solid Solutions. *Journal of Physics and Chemistry of Solids* **1961**, *19* (1), 35–50; Wagner, C. Theorie Der Alterung von Niederschlägen Durch Umlösen (Ostwald-Reifung). *Zeitschrift für Elektrochemie, Berichte der Bunsengesellschaft für physikalische Chemie* **1961**, *65* (7-8), 581–591.

[118] Zinke-Allmang, M.; Feldman, L. C.; Grabow, M. H. Clustering on Surfaces. *Surface Science Reports* **1992**, *16* (8), 377–463.

[119] Datye, A. K.; Xu, Q.; Kharas, K. C.; McCarty, J. M. Particle Size Distributions in Heterogeneous Catalysts: What Do They Tell Us about the Sintering Mechanism? *Catalysis Today* **2006**, *111* (1–2), 59–67.

[120] Ruffino, F.; Torrisi, V.; Marletta, G.; Grimaldi, M. G. Atomic Force Microscopy Investigation of the Kinetic Growth Mechanisms of Sputtered Nanostructured Au Film on Mica: Towards a Nanoscale Morphology Control. *Nanoscale Res Lett* **2011**, *6* (1), 112.

[121] Hansen, T. W.; DeLaRiva, A. T.; Challa, S. R.; Datye, A. K. Sintering of Catalytic Nanoparticles: Particle Migration or Ostwald Ripening? *Acc. Chem. Res.* **2013**, *46* (8), 1720–1730.

[122] Morgenstern, K.; Rosenfeld, G.; Comsa, G. Decay of Two-Dimensional Ag Islands on Ag(111). *Phys. Rev. Lett.* **1996**, *76* (12), 2113–2116; Schulze Icking-Konert, G.; Giesen, M.; Ibach, H. Decay of Cu Adatom Islands on Cu(111). *Surface Science* **1998**, *398* (1–2), 37–48.

[123] Richardson, J. T.; Crump, J. G. Crystallite Size Distributions of Sintered Nickel Catalysts. *Journal of Catalysis* **1979**, *57* (3), 417–425; Jak, M. J. J.; Konstapel, C.; van Kreuningen, A.; Verhoeven, J.; Frenken, J. W. M. Scanning Tunnelling Microscopy Study of the Growth of Small Palladium Particles on TiO2(110). *Surface Science* **2000**, *457* (3), 295–310.

[124] Harris, P. J. F. Growth and Structure of Supported Metal Catalyst Particles. *International Materials Reviews* **1995**, *40* (3), 97–115.

[125] Smoluchowski, M. V. Drei Vortrage Uber Diffusion, Brownsche Bewegung Und Koagulation von Kolloidteilchen. *Zeitschrift fur Physik* **1916**, *17*, 585–599.

[126] Pai, W. W.; Swan, A. K.; Zhang, Z.; Wendelken, J. F. Island Diffusion and Coarsening on Metal (100) Surfaces. *Phys. Rev. Lett.* **1997**, *79* (17), 3210–3213.

[127] Wen, J.-M.; Chang, S.-L.; Burnett, J. W.; Evans, J. W.; Thiel, P. A. Diffusion of Large Two-Dimensional Ag Clusters on Ag(100). *Phys. Rev. Lett.* **1994**, *73* (19), 2591–2594; Stoldt, C. R.; Jenks, C. J.; Thiel, P. A.; Cadilhe, A. M.; Evans, J. W. Smoluchowski Ripening of Ag Islands on Ag(100). *The Journal of Chemical Physics* **1999**, *111* (11), 5157–5166.

[128] Kang, K.; Redner, S.; Meakin, P.; Leyvraz, F. Long-Time Crossover Phenomena in Coagulation Kinetics. *Phys. Rev., A* **1986**, *33* (2), 1171–1182; Hubartt, B. C.; Kryukov, Y. A.; Amar, J. G. Rate-Equation Approach to Irreversible Island Growth with Cluster Diffusion. *Phys. Rev. E* **2011**, *84* (2), 021604.

[129] Binder, K.; Kalos, M. H. "Critical Clusters" in a Supersaturated Vapor: Theory and Monte Carlo Simulation. *J Stat Phys* **1980**, *22* (3), 363–396.

[130] Morgenstern, K.; Rosenfeld, G.; Poelsema, B.; Comsa, G. Brownian Motion of Vacancy Islands on Ag(111). *Phys. Rev. Lett.* **1995**, *74* (11), 2058–2061.

[131] Sholl, D. S.; Skodje, R. T. Diffusion of Clusters of Atoms and Vacancies on Surfaces and the Dynamics of Diffusion-Driven Coarsening. *Phys. Rev. Lett.* **1995**, *75* (17), 3158–3161; Van Siclen, C. D. Single Jump Mechanisms for Large Cluster Diffusion on Metal Surfaces. *Phys. Rev. Lett.* **1995**, *75* (8), 1574–1577; Voter, A. F. Classically Exact Overlayer Dynamics: Diffusion of Rhodium Clusters on Rh(100). *Phys. Rev., B Condens. Matter* **1986**, *34* (10), 6819–6829; Khare, S. V.; Bartelt, N. C.; Einstein, T. L. Diffusion of Monolayer Adatom and Vacancy Clusters: Langevin Analysis and Monte Carlo Simulations of Their Brownian Motion. *Phys. Rev. Lett.* **1995**, *75* (11), 2148–2151.

[132] Chen, Y.; Palmer, R. E.; Wilcoxon, J. P. Sintering of Passivated Gold Nanoparticles under the Electron Beam. *Langmuir* **2006**, *22* (6), 2851–2855; Rizza, G.; Cheverry, H.; Gacoin, T.; Lamasson, A.; Henry, S. Ion Beam Irradiation of Embedded Nanoparticles: Toward an in Situ Control of Size and Spatial Distribution. *Journal of Applied Physics* **2007**, *101* (1), 014321; Ruffino, F.; Bastiani, R. D.; Grimaldi, M. G.; Bongiorno, C.; Giannazzo, F.; Roccaforte, F.; Spinella, C.; Raineri, V. Self-Organization of Au Nanoclusters on the SiO2 Surface Induced by 200 keV-Ar Irradiation. *Nuclear Instruments and Methods in Physics Research, Section B: Beam Interactions with Materials and Atoms* **2007**, *257*, 810–814; Ruffino, F.; Grimaldi, M. G.; Giannazzo, F.; Roccaforte, F.; Raineri, V.; Bongiorno, C.; Spinella, C. Kinetic Mechanisms of the in Situ Electron Beam-Induced Self-Organization of Gold Nanoclusters in SiO 2. *J. Phys. D: Appl. Phys.* **2009**, *42* (7), 075304; Rizza, G.; Attouchi, F.; Coulon, P.-E.; Perruchas, S.; Gacoin, T.; Monnet, I.; Largeau, L. Rayleigh-like Instability in the Ion-Shaping of Au-Ag Alloy Nanoparticles Embedded within a Silica Matrix. *Nanotechnology* **2011**, *22* (17), 175305; Dawi, E. A.; Vredenberg, A. M.; Rizza, G.; Toulemonde, M. Ion-Induced Elongation of Gold Nanoparticles in Silica by Irradiation with Ag and Cu Swift Heavy Ions: Track Radius and Energy Loss Threshold. *Nanotechnology* **2011**, *22* (21), 215607.

[133] Granqvist, C. G.; Buhrman, R. A. Size Distributions for Supported Metal Catalysts. *Journal of Catalysis* **1976**, *42* (3), 477–479.

[134] Subramaniam, C.; Tom, R. T.; Pradeep, T. On the Formation of Protected Gold Nanoparticles from $AuCl_4^-$ by the Reduction Using Aromatic Amines. *J Nanopart Res* **2005**, *7* (2-3), 209–217.

[135] Yang, Y.; Yan, Y.; Wang, W.; Li, J. Precise Size Control of Hydrophobic Gold Nanoparticles Using Cooperative Effect of Refluxing Ripening and Seeding Growth. *Nanotechnology* **2008**, *19* (17), 175603.

[136] Sakai, T.; Alexandridis, P. Mechanism of Gold Metal Ion Reduction, Nanoparticle Growth and Size Control in Aqueous Amphiphilic Block Copolymer Solutions at Ambient Conditions. *J. Phys. Chem. B* **2005,** *109,* 7766–7777.

[137] Sánchez-Iglesias, A.; Aldeanueva-Potel, P.; Ni, W.; Pérez-Juste, J.; Pastoriza-Santos, I.; Alvarez-Puebla, R. A.; Mbenkum, B. N.; Liz-Marzán, L. M. Chemical Seeded Growth of Ag Nanoparticle Arrays and Their Application as Reproducible SERS Substrates. *Nano Today* **2010**, *5* (1), 21–27.

[138] Brown, K. R.; Natan, M. J. Hydroxylamine Seeding of Colloidal Au Nanoparticles in Solution and on Surfaces. *Langmuir* **1998**, *14* (4), 726–728.

[139] Brown, K. R.; Walter, D. G.; Natan, M. J. Seeding of Colloidal Au Nanoparticle Solutions. 2. Improved Control of Particle Size and Shape. *Chem. Mater.* **2000**, *12* (2), 306–313.

[140] Dement'eva, O. V.; Kartseva, M. E.; Bol'shakova, A. V.; Vereshchagina, O. F.; Ogarev, V. A.; Kalinina, M. A.; Rudoy, V. M. Metal Nanoparticles on Polymer Surfaces: 4. Preparation and Structure of Colloidal Gold Films. *Colloid J* **2005**, *67* (2), 123–133.

[141] Brown, K. R.; Lyon, L. A.; Fox, A. P.; Reiss, B. D.; Natan, M. J. Hydroxylamine Seeding of Colloidal Au Nanoparticles. 3. Controlled Formation of Conductive Au Films. *Chem. Mater.* **2000**, *12* (2), 314–323.

[142] Meltzer, S.; Resch, R.; Koel, B. E.; Thompson, M. E.; Madhukar, A.; Requicha, A. A. G.; Will, P. Fabrication of Nanostructures by Hydroxylamine Seeding of Gold Nanoparticle Templates. *Langmuir* **2001**, *17* (5), 1713–1718.

[143] Bullen, C.; Zijlstra, P.; Bakker, E.; Gu, M.; Raston, C. Chemical Kinetics of Gold Nanorod Growth in Aqueous CTAB Solutions. *Crystal Growth & Design* **2011**, *11* (8), 3375–3380.

[144] Huang, C.-C.; Yang, Z.; Chang, H.-T. Synthesis of Dumbbell-Shaped Au−Ag Core−Shell Nanorods by Seed-Mediated Growth under Alkaline Conditions. *Langmuir* **2004**, *20* (15), 6089–6092.

[145] Murphy, C. j.; Jana, N. r. Controlling the Aspect Ratio of Inorganic Nanorods and Nanowires. *Adv. Mater.* **2002**, *14* (1), 80–82.

[146] Taub, N.; Krichevski, O.; Markovich, G. Growth of Gold Nanorods on Surfaces. *J. Phys. Chem. B* **2003**, *107* (42), 11579–11582.

[147] Wei, Z.; Zamborini, F. P. Directly Monitoring the Growth of Gold Nanoparticle Seeds into Gold Nanorods. *Langmuir* **2004**, *20* (26), 11301–11304.

[148] Mieszawska, A. J.; Zamborini, F. P. Gold Nanorods Grown Directly on Surfaces from Microscale Patterns of Gold Seeds. *Chem. Mater.* **2005**, *17* (13), 3415–3420.

[149] Umar, A. A.; Oyama, M.; Salleh, M. M.; Majlis, B. Y. Formation of High-Yield Gold Nanoplates on the Surface: Effective Two-Dimensional Crystal Growth of Nanoseed in the Presence of Poly(vinylpyrrolidone) and Cetyltrimethylammonium Bromide. *Crystal Growth & Design* **2009**, *9* (6), 2835–2840.

[150] Lu, X.; Rycenga, M.; Skrabalak, S. E.; Wiley, B.; Xia, Y. Chemical Synthesis of Novel Plasmonic Nanoparticles. *Annual Review of Physical Chemistry* **2009**, *60* (1), 167–192.

[151] Chen, S.; Kimura, K. A New Strategy for the Synthesis of Semiconductor-Metal Hybrid Nanocomposites: Electrostatic Self-Assembly of Nanoparticles. *Chemistry Letters* **1999**, *28* (3), 233–234.

[152] Zhu, T.; Vasilev, K.; Kreiter, M.; Mittler, S.; Knoll, W. Surface Modification of Citrate-Reduced Colloidal Gold Nanoparticles with 2-Mercaptosuccinic Acid. *Langmuir* **2003**, *19* (22), 9518–9525.

[153] Niu, J.; Zhu, T.; Liu, Z. One-Step Seed-Mediated Growth of 30–150 Nm Quasispherical Gold Nanoparticles with 2-Mercaptosuccinic Acid as a New Reducing Agent. *Nanotechnology* **2007**, *18* (32), 325607.

[154] Sajanlal, P. R.; Sreeprasad, T. S.; Nair, A. S.; Pradeep, T. Wires, Plates, Flowers, Needles, and Core−Shells: Diverse Nanostructures of Gold Using Polyaniline Templates. *Langmuir* **2008**, *24* (9), 4607–4614

[155] Ali Umar, A.; Oyama, M. High-Yield Synthesis of Tetrahedral-Like Gold Nanotripods Using an Aqueous Binary Mixture of Cetyltrimethylammonium Bromide and Hexamethylenetetramine. *Crystal Growth & Design* **2009**, *9* (2), 1146–1152

[156] Xiao, Z.-L.; Han, C. Y.; Kwok, W.-K.; Wang, H.-H.; Welp, U.; Wang, J.; Crabtree, G. W. Tuning the Architecture of Mesostructures by Electrodeposition. *J. Am. Chem. Soc.* **2004**, *126* (8), 2316–2317

[157] Penner, R. M. Mesoscopic Metal Particles and Wires by Electrodeposition. *J. Phys. Chem. B* **2002**, *106* (13), 3339–3353

[158] Zhang, B.; Xu, P.; Xie, X.; Wei, H.; Li, Z.; Mack, N. H.; Han, X.; Xu, H.; Wang, H.-L. Acid-Directed Synthesis of SERS-Active Hierarchical Assemblies of Silver Nanostructures. *J. Mater. Chem.* **2011**, *21* (8), 2495–2501

[159] Sajanlal, P. R.; Pradeep, T. Mesoflowers: A New Class of Highly Efficient Surface-Enhanced Raman Active and Infrared-Absorbing Materials. *Nano Res.* **2009**, *2* (4), 306–320

[160] Pető, G.; Molnár, G. L.; Pászti, Z.; Geszti, O.; Beck, A.; Guczi, L. Electronic Structure of Gold Nanoparticles Deposited on SiOx/Si(100). *Materials Science and Engineering: C* **2002**, *19* (1–2), 95–99

[161] Jena, B. K.; Raj, C. R. Synthesis of Flower-like Gold Nanoparticles and Their Electrocatalytic Activity Towards the Oxidation of Methanol and the Reduction of Oxygen. *Langmuir* **2007**, *23* (7), 4064–4070

[162] Li, Y.; Shi, G. Electrochemical Growth of Two-Dimensional Gold Nanostructures on a Thin Polypyrrole Film Modified ITO Electrode. *J. Phys. Chem. B* **2005**, *109* (50), 23787–23793

[163] Kim, J.-H.; Kang, T.; Yoo, S. M.; Lee, S. Y.; Kim, B.; Choi, Y.-K. A Well-Ordered Flower-like Gold Nanostructure for Integrated Sensors via Surface-Enhanced Raman Scattering. *Nanotechnology* **2009**, *20* (23), 235302

[164] Xie, J.; Zhang, Q.; Lee, J. Y.; Wang, D. I. C. The Synthesis of SERS-Active Gold Nanoflower Tags for In Vivo Applications. *ACS Nano* **2008**, *2* (12), 2473–2480

[165] Wang, T.; Hu, X.; Dong, S. Surfactantless Synthesis of Multiple Shapes of Gold Nanostructures and Their Shape-Dependent SERS Spectroscopy. *J. Phys. Chem. B* **2006**, *110* (34), 16930–16936

[166] Giannini, V.; Rodríguez-Oliveros, R.; Sánchez-Gil, J. A. Surface Plasmon Resonances of Metallic Nanostars/Nanoflowers for Surface-Enhanced Raman Scattering. *Plasmonics* **2010**, *5* (1), 99–104

[167] Jena, B. K.; Raj, C. R. Seedless, Surfactantless Room Temperature Synthesis of Single Crystalline Fluorescent Gold Nanoflowers with Pronounced SERS and Electrocatalytic Activity. *Chem. Mater.* **2008**, *20* (11), 3546–3548

[168] Das, A. K.; Raj, C. R. Facile Growth of Flower-like Au Nanocrystals and Electroanalysis of Biomolecules. *Journal of Electroanalytical Chemistry* **2010**, *638* (2), 189–194

[169] Huang, X.-J.; Yarimaga, O.; Kim, J.-H.; Choi, Y.-K. Substrate Surface Roughness-Dependent 3-D Complex Nanoarchitectures of Gold Particles from Directed Electrodeposition. *J. Mater. Chem.* **2009**, *19* (4), 478–483

[170] Wang, W.; Cui, H. Chitosan-Luminol Reduced Gold Nanoflowers: From One-Pot Synthesis to Morphology-Dependent SPR and Chemiluminescence Sensing. *J. Phys. Chem. C* **2008**, *112* (29), 10759–10766

[171] Wang, W.; Yang, X.; Cui, H. Growth Mechanism of Flowerlike Gold Nanostructures: Surface Plasmon Resonance (SPR) and Resonance Rayleigh Scattering (RRS) Approaches to Growth Monitoring. *J. Phys. Chem. C* **2008**, *112* (42), 16348–16353

[172] Zhong, L.; Zhai, X.; Zhu, X.; Yao, P.; Liu, M. Vesicle-Directed Generation of Gold Nanoflowers by Gemini Amphiphiles and the Spacer-Controlled Morphology and Optical Property. *Langmuir* **2010**, *26* (8), 5876–5881

[173] Li, H.; Yang, Y.; Wang, Y.; Li, W.; Bi, L.; Wu, L. In Situ Fabrication of Flower-like Gold Nanoparticles in Surfactant-Polyoxometalate-Hybrid Spherical Assemblies. *Chem. Commun.* **2010**, *46* (21), 3750–3752

[174] Wang, Z.; Zhang, J.; Ekman, J. M.; Kenis, P. J. A.; Lu, Y. DNA-Mediated Control of Metal Nanoparticle Shape: One-Pot Synthesis and Cellular Uptake of Highly Stable and Functional Gold Nanoflowers. *Nano Lett.* **2010**, *10* (5), 1886–1891

[175] Wang, L.; Wei, G.; Guo, C.; Sun, L.; Sun, Y.; Song, Y.; Yang, T.; Li, Z. Photochemical Synthesis and Self-Assembly of Gold Nanoparticles. *Colloids and Surfaces A: Physicochemical and Engineering Aspects* **2008**, *312* (2–3), 148–153

[176] Kameoka, Y.; Pigford, R. L. Absorption of Nitrogen Dioxide into Water, Sulfuric Acid, Sodium Hydroxide, and Alkaline Sodium Sulfite Aqueous Solutions. *Ind. Eng. Chem. Fund.* **1977**, *16* (1), 163–169

[177] Bielański, A. *Podstawy chemii nieorganicznej. 1 1*; Wydawnictwo Naukowe PWN: Warszawa, 2010

[178] Shi, H.; Bi, H.; Yao, B.; Zhang, L. Dissolution of Au Nanoparticles in Hydrochloric Acid Solution as Studied by Optical Absorption. *Applied Surface Science* **2000**, *161* (1–2), 276–278

[179] Haruta, M. When Gold Is Not Noble: Catalysis by Nanoparticles. *Chem Record* **2003**, *3* (2), 75–87

[180] Esumi, K.; Suzuki, A.; Yamahira, A.; Torigoe, K. Role of Poly(amidoamine) Dendrimers for Preparing Nanoparticles of Gold, Platinum, and Silver. *Langmuir* **2000**, *16* (6), 2604–2608

[181] Bard, A. J. *Electroanalytical Chemistry: A Series of Advances.*; Marcel Dekker: New York, 1970

[182] Stremsdoerfer, G.; Perrot, H.; Martin, J. R.; Cléchet, P. Autocatalytic Deposition of Gold and Palladium onto N - GaAs in Acidic Media. *J. Electrochem. Soc.* **1988**, *135* (11), 2881–2886

[183] Watzky, M. A.; Finke, R. G. Transition Metal Nanocluster Formation Kinetic and Mechanistic Studies. A New Mechanism When Hydrogen Is the Reductant: Slow, Continuous Nucleation and Fast Autocatalytic Surface Growth. *J. Am. Chem. Soc.* **1997**, *119* (43), 10382–10400

[184] Finney, E. E.; Finke, R. G. Fitting and Interpreting Transition-Metal Nanocluster Formation and Other Sigmoidal-Appearing Kinetic Data: A More Thorough Testing of Dispersive Kinetic vs Chemical-Mechanism-Based Equations and Treatments for 4-Step Type Kinetic Data. *Chem. Mater.* **2009**, *21* (19), 4468–4479

[185] Mulvaney, S. P.; He, L.; Natan, M. J.; Keating, C. D. Three-Layer Substrates for Surface-Enhanced Raman Scattering: Preparation and Preliminary Evaluation. *J. Raman Spectrosc.* **2003**, *34* (2), 163–171

[186] Oran, J. M.; Hinde, R. J.; Abu Hatab, N.; Retterer, S. T.; Sepaniak, M. J. Nanofabricated Periodic Arrays of Silver Elliptical Discs as SERS Substrates. *J. Raman Spectrosc.* **2008**, *39* (12), 1811–1820

[187] Khan, M. A.; Hogan, T. P.; Shanker, B. Gold-Coated Zinc Oxide Nanowire-Based Substrate for Surface-Enhanced Raman Spectroscopy. *J. Raman Spectrosc.* **2009**, *40* (11), 1539–1545

[188] Driskell, J. D.; Shanmukh, S.; Liu, Y.; Chaney, S. B.; Tang, X.-J.; Zhao, Y.-P.; Dluhy, R. A. The Use of Aligned Silver Nanorod Arrays Prepared by Oblique Angle Deposition as Surface Enhanced Raman Scattering Substrates. *J. Phys. Chem. C* **2008**, *112* (4), 895–901

[189] Naumann, D. Ft-Infrared and Ft-Raman Spectroscopy in Biomedical Research. *Applied Spectroscopy Reviews* **2001**, *36*, 239–298

[190] Kamińska, A.; Dzięcielewski, I.; Weyher, J. L.; Waluk, J.; Gawinkowski, S.; Sashuk, V.; Fiałkowski, M.; Sawicka, M.; Suski, T.; Porowski, S.; Hołyst, R. Highly reproducible, stable and multiply regenerated surface-enhanced Raman scattering substrate for biomedical applications. *J.Mater.Chem.* **2011**, *21*, 8662–8669.

[191] Adamkiewicz, W. Otrzymywanie powierzchni wzmacniających sygnały Ramana. Published doctoral thesis (http://rcin.org.pl/dlibra/docmetadata?id=56798&from=publication), Institute of Phisical Chemistry of the Polish Academy of Sciences, **2015**, Warsaw, Poland.

[192] Paczesny, J. Ordered thin films of amphiphilic compounds and nanoparticles. Published doctoral thesis (http://rcin.org.pl/dlibra/docmetadata?id=17498&from=publication), Institute of Phisical Chemistry of the Polish Academy of Sciences, **2012**, Warsaw, Poland.